DOKUZ EYLÜL UNIVERSITY

GRADUATE SCHOOL OF NATURAL AND APPLIED SCIENCES

PRODUCTION AND DEVELOPMENT OF PEROVSKITE SOLAR CELLS WITH INORGANIC HOLE TRANSPORT MATERIALS

by

Salih Alper AKALIN

January, 2022

İZMİR

PRODUCTION AND DEVELOPMENT OF PEROVSKITE SOLAR CELLS WITH INORGANIC HOLE TRANSPORT MATERIALS

A Thesis Submitted to the
Graduate School of Natural and Applied Sciences of Dokuz Eylül University
In Partial Fulfillment of the Requirements for the Degree of Doctor of Philosophy in Nanoscience and Nanoengineering Program

by
Salih Alper AKALIN

January, 2022
İZMİR

Ph.D. THESIS EXAMINATION RESULT FORM

We have read the thesis entitled **"PRODUCTION AND DEVELOPMENT OF PEROVSKITE SOLAR CELLS WITH INORGANIC HOLE TRANSPORT MATERIALS"** completed by **SALİH ALPER AKALIN** under supervision of **ASSOC. PROF. DR MUSTAFA EROL** and we certify that in our opinion it is fully adequate, in scope and in quality, as a thesis for the degree of Doctor of Philosophy.

Assoc. Prof. Dr. Mustafa EROL

Supervisor

Assoc. Prof. Dr. M. Faruk EBEOĞLUGİL

Thesis Committee Member

Assoc. Prof. Dr. Fethullah GÜNEŞ

Thesis Committee Member

Prof. Dr. Şule ERTAN ELA

Examining Committee Member

Assoc. Prof. Dr. Serpil DENİZALTI

Examining Committee Member

Prof. Dr. Okan FISTIKOĞLU

Director

Graduate School of Natural and Applied Sciences

ACKNOWLEDGMENT

First of all, I would like to express my deep sense of gratitude to my advisor Assoc. Prof. Dr. Mustafa EROL for his constructive ideas, help, constant support, guidance and contributions. I would also like to thank my committee members, Assoc. Prof. Dr. M. Faruk EBEOĞLUGİL and Assoc. Prof. Dr. Fethullah GÜNEŞ for reviewing my study and offering valuable suggestions and sharing their visions about the content of my thesis.

I wish to extend my sincere thanks to Assist. Prof. Dr. Serdar YILDIRIM and Dr. Sibel OĞUZLAR for working in harmony as a team on the same project. I would like to thank MSc. Begüm UZUNBAYIR and Erdem Tevfik ÖZDEMİR for their collaboration in the laboratory and support of some of my studies. I believe they will achieve great success in the future. I would like to thank Dr. Hilmiye Deniz ERTUĞRUL UYGUN, MSc. Özgür Yasin KESKİN and MSc. Ahmet Çağrı KILINÇ for their support in the analyses. I would like to express my special thanks to Dr. Uğur Deneb MENDA, Dr. Pınar GÖKDEMİR CHOI, and Prof. Dr. Serap GÜNEŞ for answering all my questions about perovskite solar cells and sharing all the information they know with me.

This study was funded by DEÜ Department of Scientific Research Project (BAP) with the name “Production and development of hole transport materials in next generation perovskite solar cells” and project number 2019.KB.MLT.004. Hence, I would like to thank to DEÜ BAP and EMUM for funding and infrastructural supports.

Finally, I would like to thank to my mother Nurdan AKALIN, my brother Hilmi Arkut AKALIN, and also to my father Erdal AKALIN, who has contributed to me getting to where I am today, even though he is not with us. I would like to give a special thanks to my lovely wife, Merve EVYAPAN AKALIN for encouraging me to progress on the scientific journey and always supporting me on this way.

Salih Alper AKALIN

PRODUCTION AND DEVELOPMENT OF PEROVSKITE SOLAR CELLS WITH INORGANIC HOLE TRANSPORT MATERIALS

ABSTRACT

Perovskite solar cells have recently emerged as the most interesting subtype of solar cells, which is one of the renewable energy types, thanks to their various design capabilities, production costs and high efficiency in a short time. Perovskite solar cells, which consist of three important layers as hole transport layer, absorber layer and electron transport layer, can be formed in p-i-n or n-i-p architecture, depending on their usage and production types. The material and production method used in the p-type hole transport layer in cells with p-i-n architecture are very important. In order for the photons to reach the absorber layer, this layer must be highly transparent, have high hole mobility and have a stable structure. At the same time, band gap are also very important in the electron-blocking layer function.

In this thesis, doped and undoped nickel oxide thin films were deposited on indium tin oxide in a radio frequency magnetron sputtering system to be used as a hole transport layer. Sputtering target materials used in the deposition of thin films were obtained by sintering the powders produced using the sol-gel method after pressing with the help of cold isostatic pressing. In the thesis study, the structural, morphological, optical, and electrical properties of powders, target materials and films were examined separately. Perovskite solar cells were produced with these films and an efficiency of over fifteen percent was achieved.

Keywords: Perovskite solar cell, hole transport material, thin film

İNORGANIK BOŞLUK TAŞIYICI MALZEMELİ PEROVSKİT GÜNEŞ HÜCRELERİNİN ÜRETİLMESİ VE GELİŞTİRİLMESİ

ÖZ

Perovskit güneş hücreleri, yenilenebilir enerji türlerinden biri olan güneş hücrelerinin çeşitli tasarım kabiliyetleri, üretim maliyetleri ve kısa sürede yüksek verime ulaşması gibi özellikleri sayesinde son zamanlarda en ilgi çekici alt türü olarak karşımıza çıkmaktadır. Boşluk taşıyıcı katman, soğurucu katman ve elektron taşıyıcı katman olarak üç önemli katmandan oluşan perovskit güneş hücreleri kullanım ve üretim türlerine göre p-i-n ya da n-i-p mimarisinde oluşturulabilmektedir. P-i-n mimarideki hücrelerde p-tipi olan boşluk taşıyıcı katmanda kullanılan malzeme ve üretim yöntemi oldukça önemlidir. Fotonların soğurucu katmana ulaşması için bu katmanın oldukça transparan, yüksek boşluk hareketliliğine sahip ve kararlı yapıda olması gerekmektedir. Aynı zamanda bant boşluğu da elektron engelleyici katman görevinde oldukça önemlidir.

Bu tezde, katkılı ve katkısız nikel oksit ince filmler boşluk taşıyıcı katman olarak kullanılmak üzere radyo frekanslı magnetron saçtırma sisteminde indiyum kalay oksit üzerine biriktirilmiştir. İnce filmlerin biriktirilmesinde kullanılan saçtırma hedef malzemeleri, sol-jel yöntemi kullanılarak üretilen tozların soğuk izostatik presleme yardımıyla preslendikten sonra sinterlenmesiyle elde edilmiştir. Tez çalışmasında tozların, hedef malzemelerin ve filmlerin yapısal, morfolojik, optik ve elektriksel özellikleri ayrı ayrı incelenmiştir. Bu filmler ile perovskit güneş hücreleri üretilmiş ve yüzde on beşin üzerinde verimlilik elde edilmiştir.

Anahtar kelimeler: Perovskit güneş hücresi, boşluk taşıyıcı malzeme, ince film

CONTENTS

Page

LIST OF FIGURES

Page

LIST OF TABLES

Page

CHAPTER ONE
INTRODUCTION

Global energy consumption continues without slowing down and the energy need is increasing exponentially day by day. With the decrease of finite fossil fuel sources, an increase is observed in the search for alternative energy sources, especially renewables, in order to meet the increasing demand. The share of renewable energy, which is the general title of photovoltaic, wind energy, hydropower, bio-power, geothermal, etc., reached ~29% in electrical energy conversion in 2020. In that year, 256 GW of renewable energy capacity was added up to the one in 2019, and the figures of renewable power installed around the world increased by 10% to 2839 GW. Among the renewable energy types, solar energy has shown the highest annual capacity increase since 2016, thanks to its features such as ease of installation, modular structure, and easy adaptation to various environments. A new capacity increase of 139 GW was recorded in 2020, and the installed power worldwide reached to 760 GW. The installed power, which was 39 GW in 2010, has grown 19.5 times in only 10 years (REN21, 2021). By this motivation, it is foreseen that the capacity increases will boost over the next years. The tremendous interest in solar energy systems encourages researchers to develop solar cells that are more innovative, economical, stable, and applicable on various surfaces.

Although studies on solar cells have accelerated in recent years, the pioneering studies are dating back to very old times. The PV effect was first discovered by Becquerel in 1839. The first PV device was created by Charles Fritts, containing a selenium semiconductor. The first study with silicon cell, the most commercial types of the solar cell type today, was made by researchers at Bell Laboratory, and a 6% efficiency value was obtained (Righini & Enrichi, 2020). Since then, solar cells with varying architectures and materials have been created and continued to be created.

Today, the present interest in renewable and sustainable energy resources is constantly increasing due to rising energy consumption, the danger of depletion of fossil resources, and global climate change. To meet this need, many solar cells

powered by solar energy are being developed. These cells generally convert the energy of incident photons from the sun falling into their surfaces to electrical energy with various efficiency and stability values depending on electronic, optical, and structural properties of their functional layers (Zweibel & Hersch, 1984). Looking from the past to the present, researchers have always challenged to produce more efficient solar cells with more economical materials and easier production methods. In this context, solar cells are mainly defined within three different generations according to technology, material type, production method, cost, and design.

The first generation of solar cells is composed of silicon and/or germanium and is made of rigid bulk materials. A series of processes must take place such as formation of p-n junctions, deposition of anti-reflection layer, texturing, and deposition of metallic contacts to convert the single crystal Si wafer obtained from Si ingot by the Cz method into a solar cell. Both mono(single)-crystalline and poly(multi-crystalline) Si are used in PV technology with their best reported efficiencies as over 26% and 23%, respectively. Together they are the most widely used commercial solar cells today, dominating 70 - 80% of the total PV market (Wilson et al., 2020). This market is shared between mono and poly-crystalline with the ratio of 62% and 38%, respectively (Philipps, Burger, Kiefer, & Kost, 2018).

The second-generation of solar cells, known as thin film solar cells, are generally based on materials such as a-Si, CIGS, or CdTe. Due to the severe manufacturing requirements associated with the first generation of cells, thin film solar cells may be manufactured in vast quantities on cost-effective substrates such as glass, polymer, or metal derivatives. Thus, low-cost, mass-production-capable, and flexible cells might be constructed. On the other hand, the limited mineral sources of beginning materials and their toxicity impose restrictions on their utilization (Ranabhat et al., 2016).

The third-generation solar cells are multilayer thin-film structures, and the two best-known members are the DSSCs and PSCs derived from DSSCs. Considering the cell efficiency improvement of these cells compared to the 1st and 2nd generation cells, their development from discovery to the present day has taken relatively short time,

especially for PSCs, as seen in Figure 1.1 (Green et al., 2021; National Renewable Energy Laboratory [NREL], 2021).

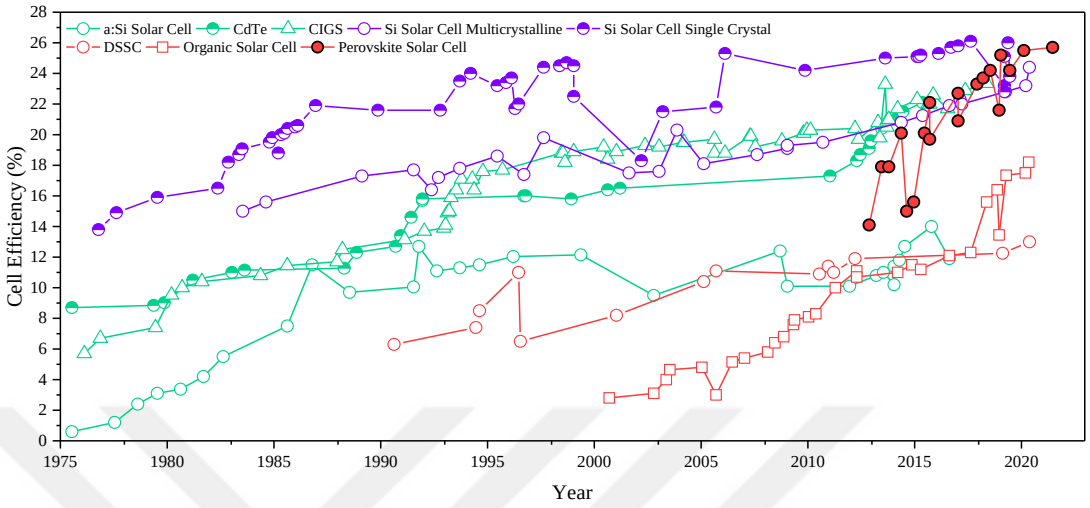

Figure 1.1 Efficiencies of photovoltaic cells

PSCs, members of third-generation PVs, were first reported in 2009 with a PCE of 3.13% (Kojima, Teshima, Shirai, & Miyasaka, 2009). The champion efficiency of 25.6% (certified 25.2%) has been reached from initial efficiency at just only a little more than a decade (Jeong et al., 2021). Due to stability issues, these cells, which have the enormous potential to increase efficiency through numerous adjustments in layers in the structure, are still in the laboratory stage. As a result, they have not yet reached the mass manufacturing and commercialization capabilities as the first- and second-generation cells.

By the motivation given above, in this thesis, to particularly contribute to the research on 3rd generation cells, several efforts were given on the development of hole transport layers (HTM) of PSCs. PSC with pristine, Li-doped, Li, Mg-codoped and Li, Cu-codoped NiO_x thin films with different additives ratios (0.05, 0.10, 0.15) as inorganic HTMs were produced together with the other layers of PSCs. Thin films were deposited on ITO/glass substrates using single target material by RF-magnetron sputtering system. The target materials with varying stoichiometries were manufactured by obtaining powders through using sol-gel method, pre-forming with cold-isostatic press, and sintering, respectively. $MAPbI_3$ as the perovskite absorber

layer was obtained by one-step deposition using spin coater on the HTM layer. PCBM as electron transport layer and BCP as buffer layer were coated by spin-coating on the absorber layer. Finally, Silver was deposited as back contact by thermal evaporation system to obtain ITO/NiO_x-based HTM/$MAPbI_3$/PCBM/BCP/Ag configurated perovskite solar cell. Following the completion of the productions, structural, optical, and electrical characterizations of the relevant layers were performed.

The thesis is planned by the following outline. In Chapter 2, the principles of photovoltaic technology and the developments in solar cells are explained. The most recent one of these developments, the perovskite solar cells and their functional layers has been explained in detail. In addition, the theoretical background of thin film growth methods and powder metallurgy are summarized. In Chapter 3, the materials and production methods used to produce doped and undoped powders, target materials, thin films are given for production of HTMs, and to fabricate perovskite solar cells. In addition, the characterization methods used for structural, optical, and electrical properties are introduced. In Chapter 4, all the results obtained in Chapter 3 were evaluated and interpreted by discussing with similar studies in the literature. Consequently, the complete results and future plans based on this research are summarized in Chapter 5.

CHAPTER TWO
THEORETICAL BACKGROUND

2.1 Photovoltaic Conversion

Solar energy is the energy that occurs as a result of the fusion reactions that take place in the core of the sun. This abundant energy is accounts for 3.86×10^{12} MW, which can meet the needs of people for a few billion years and reaches the earth's atmosphere in the amount of 1.37 kW/m^2 after traveling 1.50×10^{11} m towards the earth (Hersch & Zweibel, 1982). Since the solar spectrum contains almost all of the electromagnetic waves (in the range of 0.2 - 2 μm), it is called the black body at a temperature of about 6000K. Not all sun rays reaching the atmosphere arrive at the earth's surface, some are absorbed, reflected, or scattered by the layers in the atmosphere.

Air Mass is the path length that the sun rays travelling through the atmosphere and indicates the decrease in the intensity of light passing through the atmosphere. AM0 refers to the sun's rays just outside the atmosphere, while AM1 is used for rays that come perpendicular to the earth's surface. The AM1.5 corresponds to 41.8° sun angle regarding the zenith. AM1.5 spectrum is classified as AM1.5D and AM1.5G, which corresponds direct and global sun radiation. In all photovoltaic tests, AM1.5G solar spectrum is set as a standard with mean irradiance of 1000 W/m^2 (100 mW/cm^2) (Massiot, 2014). The differences of blackbody, AM0, and AM1.5G radiation on spectral irradiance is shown in Figure 2.1.

Various technologies such as solar thermal collectors, concentrators, and solar cells are used to convert solar energy to electricity on the earth's surface or outside the atmosphere. Solar cells, also known as photovoltaic cells, are devices had a multilayer architecture that includes semiconductor materials that produce electricity directly from the sun rays (Gorjian & Shukla, 2020).

The conductivity of semiconductors is 10^{-6} to 10^{4} $(\Omega.m)^{-1}$ which is between conductive and insulating materials. Semiconductor materials become conductive when they are excited with enough energy to cross the bandgap, which is the barrier for electrons to reach the conduction band from the valence band (Callister & Rethwisch, 2018).

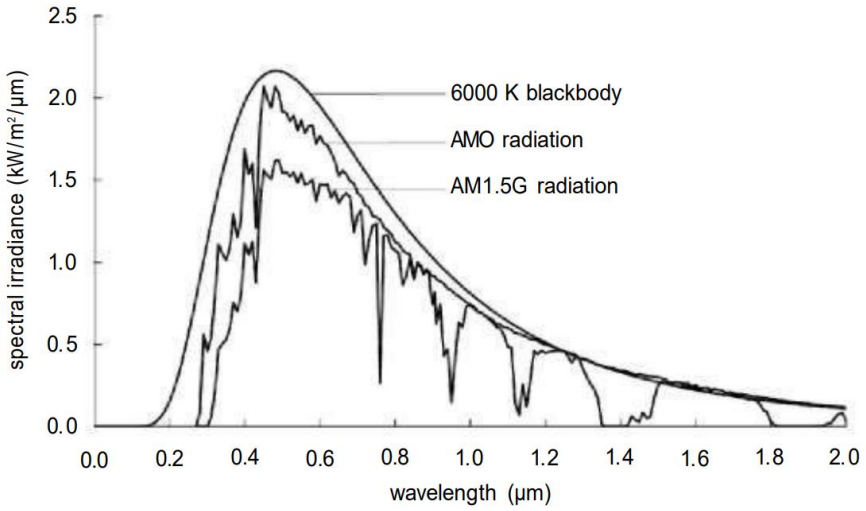

Figure 2.1 Solar irradiance of blackbody, AM0, and AM1.5G radiation (Massiot, 2014)

For solar cells, the semiconductor materials are excited with photons and photogenerated charge carriers move towards the higher energy states based on the phenomenon of the photovoltaic effect. Photon has energy is given in the following expression:

$$E_{ph} = h\nu \tag{2.1}$$

Where h is Plank's constant and ν is the frequency of the incident photons. Once the photon reaches to the material, three different situations take place, shown in Figure 2.2:

- $E_{ph} < E_g$*:* Photon energy is lower than the bandgap, photon pass through the material without any absorption.

- $E_{ph} \geq E_g$: Photon energy is greater than or equal to the bandgap, an incident photon is absorbed therefore electron is excited to a higher energy state and electron-hole pair is generated.
- $E_{ph} > E_g$: Photon energy is greater than the bandgap, the remaining energy after excitation is dissipated as heat. Therefore, regardless of the energy of the absorbed photon, all photogenerated carriers have energy as same as bandgap energy (Massiot, 2014).

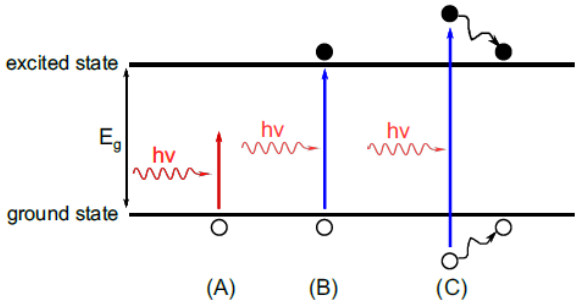

Figure 2.2 Behaviors of photoexcited electrons (Massiot, 2014)

Semiconductors classified as intrinsic (undoped) and extrinsic (p- or n-type doped) are found in solar cells with variations of p-n and p-i-n junction types. Materials are doped with impurity atoms having different valence from the host atoms so as to change such properties namely, the electronic properties. An n-type semiconductor is a material that includes impurity atoms with higher valence than host atoms, therefore extra electrons are bound by a weak electrostatic attraction and are ready to be free. On the other hand, a p-type semiconductor is a material that includes impurity atoms with lower valence than host atoms which cause incomplete bond formation enabling positions for free electrons. Phosphorus and boron doping into silicon is the most well-known example for n-type and p-type semiconductors, respectively. Free electrons, called donors, and free holes, called acceptors, are occupied states in conduction and valence bands, respectively. Figure 2.3 (a and b) shows that the Fermi energy level gravitates to the conduction band and the valence band for n-type and p-type semiconductors, respectively. If p- and n-type semiconductors intersect in a single material, the p-n junction forms, and because of the obligation of the same level of the

Fermi energy, the energy bands of p- and n-type sides bend according to Fermi energy level. For p-i-n junction, the same phenomenon existed shown in Figure 2.3.

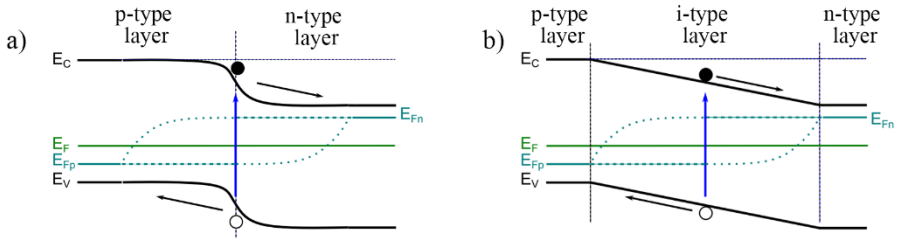

Figure 2.3 Band structure of a) p-n junction and b) p-i-n junction (Massiot, 2014)

The electrical contacts from the front and rear sides of the solar cell are crucial to collect carriers. Generally, transparent conductive oxides that allow sun rays to get into the solar cell are used as a front contact and metallic contacts are used as a rear contact. Collection efficiency depends on limitations of recombination losses which have three main types as radiative, non-radiative, and auger recombinations illustrated in Figure 2.4. *Radiative recombination* is the combination of an electron from the conduction band to a hole from the valence band directly and emits a photon with the same energy of bandgap. *Non-radiative* (also called defect-assisted) *recombination* occurs when an electron or hole unwinds to the trap energy states in the forbidden bandgap that generates from impurities or defects in the crystal. *Auger recombination* affects two different carriers which interact with each other in the conduction band at the same time. One carrier releases the energy and recombines with holes while the other get kinetic energy.

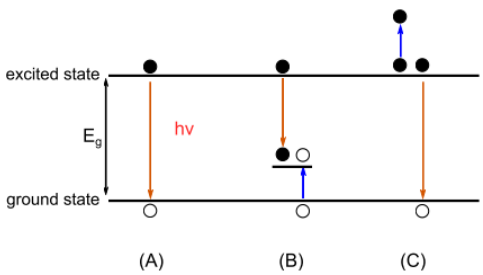

Figure 2.4 Band diagram of a) radiative, b) non-radiative, and c) auger recombination losses (Massiot, 2014)

The electrical properties of solar cells are determined by the data obtained from the standard current-voltage test methods in the AM1.5G spectrum with a light intensity of 1000 W/m^2 (100 mW/cm^2) and a temperature of 25 °C. The I-V curve illustrated in Figure 2.5 is obtained with the current values recorded for a limited voltage range. Some terminologies use to determine the efficiency of solar cells:

- I_{SC}: The current value at zero voltage
- J_{SC}: The current in a unit area (Equation 2.2)
- I_{MP}: The current value at maximum power
- V_{OC}: The voltage value at zero current
- V_{MP}: The voltage value at maximum power
- Fill Factor (FF): The ratio of the maximum realized power to the maximum possible power with I_{SC} and V_{OC} values (Equation 2.3)
- Efficiency (η or PCE): The ratio of output energy to input energy (Equation 2.4)

$$J_{SC} = \frac{I_{SC}}{Area} \tag{2.2}$$

$$FF = \frac{V_{MP} I_{MP}}{V_{OC} I_{SC}} \tag{2.3}$$

$$PCE = \frac{P_{out}}{P_{in}} = \frac{V_{OC} I_{SC} FF}{P_{in}} \tag{2.4}$$

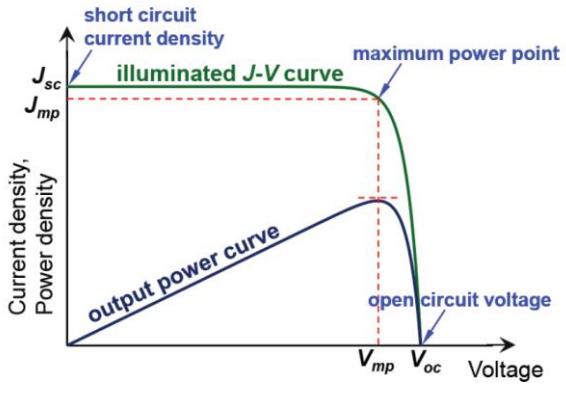

Figure 2.5 Current - voltage characteristics of solar cells (Tao, 2016)

The efficiency of solar cells is directly associated with the bandgap of the absorber layer due to bandgap should be lower than the energy of the incident photon to generate free electrons. Schockley and Queisser calculated the theoretical maximum power conversion efficiency for ideal solar cells and based on this study theoretical limit for a single-junction solar cell was found 33% with the 1.4 eV of bandgap energy called as Schockley-Queisser Limit (Figure 2.6).

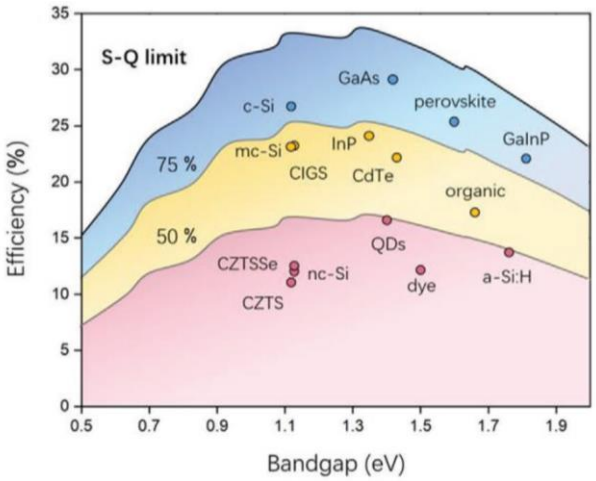

Figure 2.6 Schockley-Queisser Limit of most known solar cell materials (Z. Zhang, Li, Meng, Lien, & Gao, 2020)

From the first day to nowadays, researchers investigate new materials to achieve the value of Schockley and Queisser limit with single-junction architecture and new designs to obtain more efficiency with multi-junction architecture.

2.2 Generations of Solar Cells

There are various solar cells generated with different materials and architectures and they are classified as "generation". In many sources, solar cells are basically classified into three generations. First-generation solar cells involve silicon-based bulk solar cells such as mono and poly-crystalline Si solar cells. Second-generation solar cells, also known as thin-film solar cells, consist of a-Si:H, CIGS, CdTe. Third-generation solar cells, also known as emerging solar cells, include organic, dye-sensitized, and perovskite solar cells.

2.2.1 First Generation of Solar Cells

2.2.1.1 Silicon Solar Cells

Silicon is an intrinsic semiconductor with a 1.12 eV band gap and can be doped with IIIA and IVA elements of the periodic table to form p- and n-type semiconductors. The first silicon solar cell was invented with a p-type diffused layer on an n-type Si wafer and achieved ~6% efficiency in 1954 (Chapin, Fuller, & Pearson, 1954). At the start, boron was diffused in arsenic doped Si wafer to create p-n junction, then the procedure was changed to p-type on the n-type with phosphorus diffusion on the boron-doped Si wafer as an industrial standard. Aluminum was used to the back surface field with the mission of being back contact, hence recombination at the backside was reduced as a result of n^+pp^+ structure was formed (Figure 2.7) (Mandelkorn & Jr., 1973). Metal front contact was generated with the screen-printing technology after texturing and anti-reflection coating of the surface to improve solar cell efficiency to complete solar cell architecture. Monocrystalline Si wafers that are used in Si solar cell, transistors, chips etc. are obtained by slicing of single crystal Si ingot produced by Cz Method, while polycrystalline Si wafers are obtained by slicing of ingots prepared by directional solidification (Van Overstraeten, 1990). Mono and polycrystalline Si solar cells are the most widely used commercial solar cells today and dominate 70 - 80% of the total market with the PCE of 20 - 25% (Wilson et al., 2020).

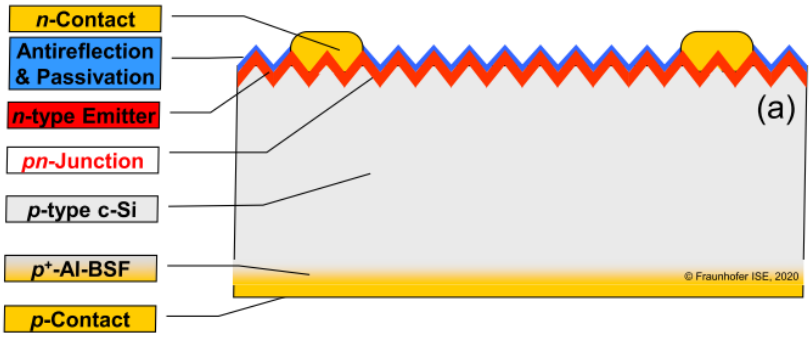

Figure 2.7 Silicon solar cell structure (Wilson et al., 2020)

2.2.2 Second Generation of Solar Cells

2.2.2.1 Cadmium Telluride

CdTe is an IIB-VIA group semiconductor with a bandgap of 1.5 eV as a promising material to absorb photon energy to convert electricity by generating of p-n junction with CdS. CdTe solar cells have a cost and production-friendly structure with several micron layers which could be produced in several hours from glass to panel and dominates 5.7% of all kinds of PV market and 76% of the thin-film PV market in 2019 (Barbato et al., 2021; Wilson et al., 2020).

The traditional architecture of CdTe solar cells is shown in Figure 2.8. The main important layer in the architecture of glass/TCO/buffer layer/CdS/CdTe/back contact is CdTe and CdS that have a mission of being p-type and n-type layer, thus p-n junction is generated.

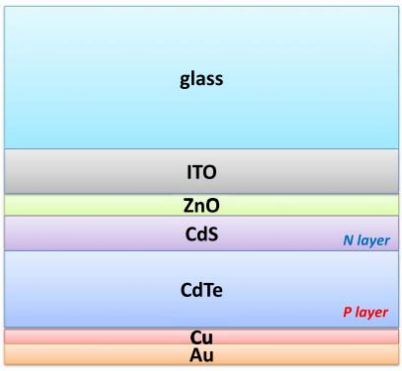

Figure 2.8 Basic structure of CdTe/CdS solar cell (Barbato et al., 2021)

The efficiency of CdTe solar cells has increased over years. In 1972, Bonnet and Rabenhorst manufactured a thin-film CdTe solar cell for the first time with vapor deposition of cadmium telluride and evaporation of cadmium sulfide with an efficiency of ~6% (Bonnet & Rabenhorst, 1972). The champion efficiencies were obtained by First Solar Company with over 20% efficiency in 2016 (T. D. Lee & Ebong, 2017).

2.2.2.2 Copper Indium Selenide and Copper Indium Gallium Selenide

CIS and CIGS are a member of I–III–VI2 chalcopyrite semiconductor alloys family. They are especially well suited as p-type absorber materials for solar cells due to their direct bandgaps ranging from ~1 to 2.6 eV. CIS thin-film solar cells have been in development since the first use of the CIS/CdS junction with 4.5% efficiency in 1976 (Kazmerski, White, & Morgan, 1976). In 2019, the champion efficiency of 23.35% was achieved in a solar cell with the configuration of Glass/Mo/Mo(S,Se)/CIGSSE/$Zn(O,S,OH)_x$/$Zn_{0.8}Mg_{0.2}O$/BZO shown in Figure 2.9 (Nakamura et al., 2019).

Figure 2.9 The structure of CIGS solar cell achieved champion efficiency (Nakamura et al., 2019)

2.2.2.3 Amorphous Silicon

a:Si solar cells are categorized under the first generation as they are silicon based or under the second generation solar cells because they are thin films, according to different sources (Ranabhat et al., 2016; Righini & Enrichi, 2020). There is an interest in a-Si thin-film material which absorb a significant amount of sunlight with its direct bandgap. Nevertheless, short orders and dangling bonds causes short diffusion length of minority carrier and aberrant electrical conduct. Therefore, passivation by hydrogen is applied to a-Si, converting it to a-Si:H, resulting in reducing dangling bond and improve the properties (T. D. Lee & Ebong, 2017). In 1976, hydrogenated a-Si:H was

used for fabrication of solar cell with a p-i-n configuration, shown in Figure 2.10, and PCE of 2.4% was measured (Carlson & Wronski, 1976). The champion efficiency exhibited 10.22% with single junction and 12.96% with a-Si:H/μc-Si:H tandem solar cell (Matsui et al., 2015).

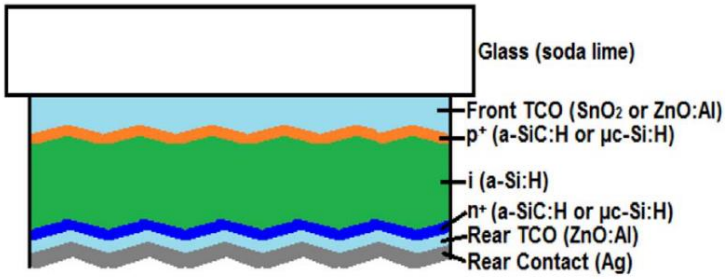

Figure 2.10 The structure of a-Si:H solar cell with p-i-n structure (T. D. Lee & Ebong, 2017)

2.2.3 Third Generation of Solar Cells

2.2.3.1 Dye-Sensitized Solar Cells

DSSCs are distinctive solar cells that have a junction of solid liquid with organic materials and are basically composed of a top electrode, porous TiO_2 layer, paint pigments, liquid electrolyte, catalyst material, and counter electrode, shown in Figure 2.11. Solar energy is captured by DSSCs through the process of artificial photosynthesis. The working principle of DSSCs can be explained as follows. The mission of dye pigments deposited on TiO_2 particles is absorption of photons, and then photoexcited electrons transport to the conduction band of TiO_2. The purpose of the iodine/tri-iodide redox double electrolyte solution is the regeneration of the base state of the dye by reducing the cation. The oxidized iodide ions are regenerated at the counter electrode which also have a purpose about collection of electrons from circuit and being catalyze of them to reduce triiodide to iodide ions (James & Contractor, 2018).

Gratzel and O'regan studied DSSC with the conducting glass sheet/TiO_2/trimetric ruthenium complex/iodide/triiodide redox electrolyte/counter electrode structure for the first time in 1991 and achieved PCE of 7.9% (O'Regan & Grätzel, 1991). Ela et al

designed a DSSC consisting of a binary electron donor system with dibenzo-BODIPY and phenothiazine and achieved 7.69% cell efficiency (Erten-Ela, Ueno, Asaba, & Kubo, 2017). In 2020, Ji et al used Thieno[3,2-*b*]indole-based organic dye in DSSCs and achieved PCE of 14.2% (Ji, Zhou, Eom, Kim, & Kim, 2020).

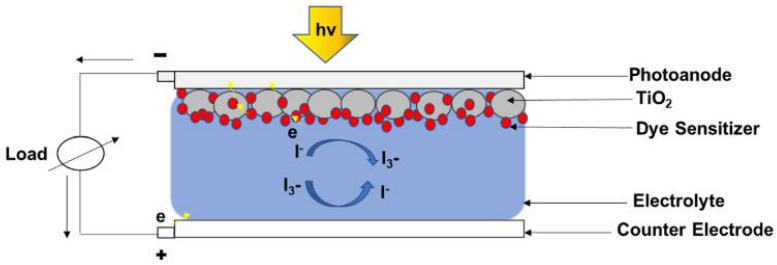

Figure 2.11 Structure of basic dye-sensitized solar cell (James & Contractor, 2018)

2.2.3.2 Perovskite Solar Cells

Perovskite solar cells get their name from the perovskite structure as photon absorber layer in the architecture. The first meeting of the perovskite structure with solar cell research was started in 2009 in the study of Kojima and colleagues using $CH_3NH_3PbBr_3$ and $CH_3NH_3PbI_3$ in DSSC, low efficiencies were obtained as 3.13% and 3.81%, respectively. Their absorption characteristics for visible region wavelengths indicate that these structures are promising for solar cells. The cell with $CH_3NH_3PbBr_3$ showed a 65% conversion at the wavelength of 400-420 nm and responded to photons at the wavelength range of 350-550 nm, in particular, the $CH_3NH_3PbI_3$ had lower efficiency, while it could respond to the entire visible region (Kojima et al., 2009).

Organo-metal halide perovskite structures have made PSCs more popular as they have their advantages such as design flexibility, relatively easy and inexpensive production, as well as efficiency limits of silicon-based solar cells (Ranabhat et al., 2016). Thanks to these features, in a short time, the champion efficiency of 25.6% (certified 25.2%) has been reached from 3.13% at just a little more than a decade (Jeong et al., 2021).

PSCs using organo-metal halide perovskites mainly consist of three main layers, namely the HTM, PSK, and ETM. From these layers, ETM and HTM, which have n-type and p-type semiconductor properties respectively, provide the movement of the electron and hole pairs formed by photons falling on the absorber PSK layer. Apart from these main layers, the TCO layer and the MC are provided in the cell, which allows input of sunlight and connection to the external circuit.

There are three main steps for the operation of PSCs, as shown in Figure 2.12:

1. Photon absorption and charge generation: Incoming photons are absorbed by perovskite, with the dissociation of excitons produced by photons that have greater than or equal energy of bandgap, electrons, and holes (charge carriers) are generated.
2. Charge transportation: Free electrons and free holes inject into ETM and HTM layers, respectively.
3. Charge extraction: Electrons and holes migrate to anode and cathode, respectively. In this architecture, the anode is a TCO such as FTO or ITO, and the cathode is generally a metal such as Au, Ag, or Al. Collected electrons and holes are transmitted to the external circuit to generate current (Marinova, Valero, & Delgado, 2017).

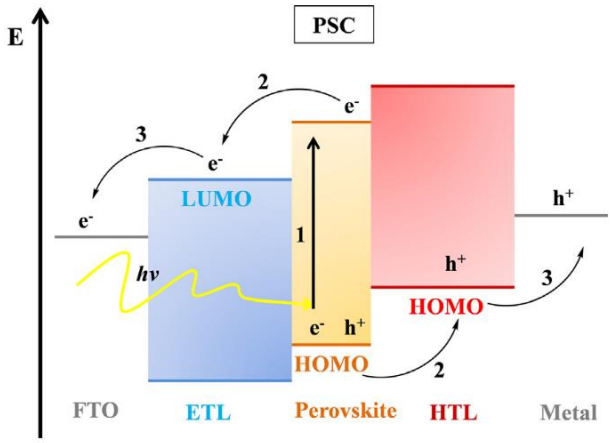

Figure 2.12 Basic operation steps of perovskite solar cells (Marinova et al., 2017)

PSCs are usually classified according to the direction of arrival of photons and architecture. These cells are defined as p-i-n if the light comes from the HTM direction, n-i-p comes from the ETM direction. In this definition, n, i, and p are pointed out ETM, PSK, and HTM layers, respectively. In addition, HTM or ETM in PSCs is mesoscopic if it has a porous interface with the perovskite compound. These layers are defined as planar perovskite cells if they are bound in a thin film-shaped interface. In summary, four different cell architectures are seen in PSCs; n-i-p mesoscopic, n-i-p planar, p-i-n mesoscopic, and p-i-n planar; shown in Figure 2.13 (Song, Watthage, Phillips, & Heben, 2016).

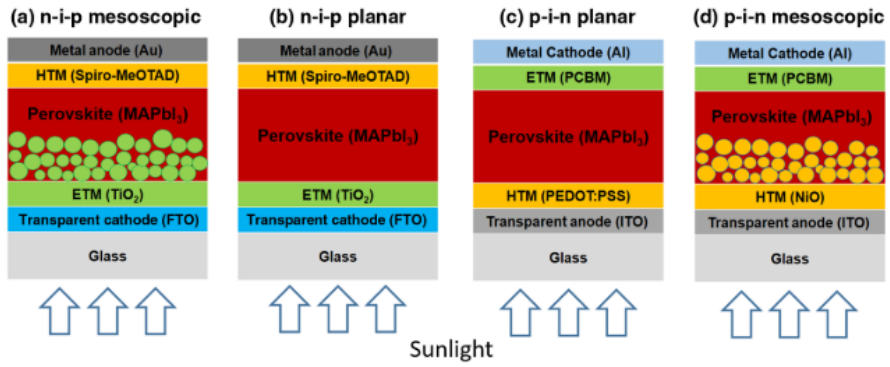

Figure 2.13 Structure of perovskite solar cell in a) mesoscopic n-i-p, b) planar n-i-p, c) planar p-i-n, and d) mesoscopic p-i-n (Song et al., 2016)

The various layers in the PSCs and the materials used in these layers are shown in Figure 2.14 for the cells in the n-i-p architecture. In TCO layers, which provide connection to the external circuit and allow photon entry, ITO and FTO are generally used in a thin-film form. The electron-rich n-type semiconductors that lead to electron mobility in architecture serve as ETM layers. These layers can be produced from two types of materials, usually organic (PCBM) or inorganic (TiO_2, ZnO, SnO_2) based. One of the most important points in the selection of materials to be used as ETM layers is that the CBM/LUMO of this n-type material must be below the CBM/LUMO level of the PSK material to form the i-n junction region in the p-i-n structure healthy. The PSK (i) layer is where the electron-hole pairs are formed (Figure 2.12). The most commonly used types of perovskite absorber layers are $CH_3NH_3PbI_3$ ($MAPbI_3$) and $CH_5N_2PbI_3$ ($FAPbI_3$) and their derivatives. HTM layers are responsible for hole

mobility. A similar important situation in ETM also applies to the selection of material for HTMs. VBM/HOMO level of p-type material must be above the VBM/HOMO level of Psk to form p-i junction, thus the properly working p-i-n cell is obtained. Organic (Spiro-OMeTAD, PTAA) and inorganic (CuO, CuSCN, NiO, etc.) materials are commonly used as HTM. After the HTM layer, metal films with good conductivity such as gold (Au) and silver (Ag) are used to complete the circuit as the rear contact on the non-illuminated side of the architecture (Fu et al., 2018).

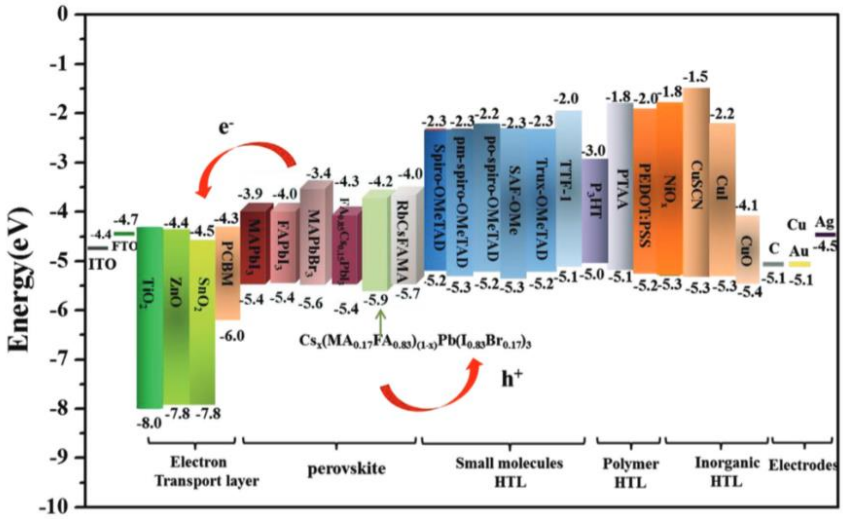

Figure 2.14 Cell structures and materials types in n-i-p architecture (Fu et al., 2018)

2.3 Layers of Perovskite Solar Cells

2.3.1 Absorber Layer

Perovskite is the name given to the ABX_3 structure which is represented to $CaTiO_3$ because it was described by L.A. Perovski after being revealed by Gustav Rose in 1839. “A” is an organic or inorganic monovalent cation, “B” is a divalent inorganic cation, and “X” is a halogen anion (Naveen Kumar, Rani, & Kurchania, 2021), shown in Figure 2.15.

In PSCs, perovskites used as absorbing layers are composed of organic and inorganic structures. In these structures, the A-side is generally MA or FA, B-side is Pb, and X-side is Cl, Br, I, or their combinations (Figure 2.15b). The popularity of

halide perovskites has risen after the studies of Mitzi and co-workers about the discovery that after the increase of dimensionality by the transition from two to three dimensional structure, organometal halide perovskite shows a semiconductor-metal transition, resulting in a decrease in the band-gap, hence could be suitable for photovoltaic applications (Mitzi, Feild, Harrison, & Guloy, 1994).

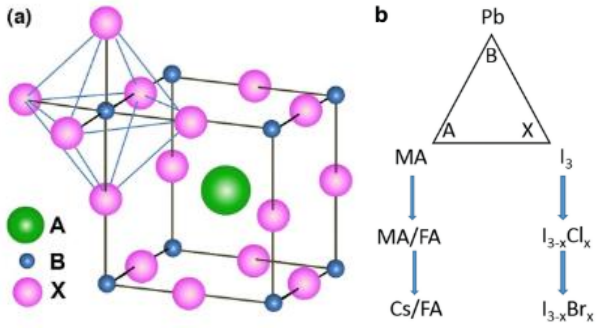

Figure 2.15 a) ABX_3 perovskite structure (Park, 2015) and b) materials of A, B, and X sides (Chi & Banerjee, 2020)

Perovskite thin films could be prepared with some methods such as single-step solution deposition, two-step solution deposition, vapor-assisted deposition, and thermal vapor deposition shown in Figure 2.16.

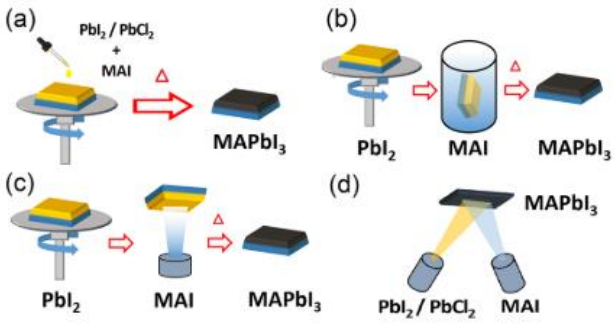

Figure 2.16 Preparation methods of perovskite thin films: a) single-step, b) two-step, c) hybrid, and d) thermal vapor deposition (Song et al., 2016)

Single-step solution deposition is frequently utilized to create perovskite thin films due to its simplicity of processing and low-cost fabrication. Precursor solutions are generally prepared by dissolving organic halides (MAI) and lead halides (PbX_2, X = I, Br, or Cl) in a solvent such as GBL, DMSO, DMF, or their different combinations.

Mostly spin-coating but sometimes spray, doctor-blading, inkjet printing, etc. could be applied to obtain perovskite film, then heated to a range of 100 - 150 °C as the post-deposition process. MAI:PbI_2 ratio, substrate material, process temperature, duration, environment (especially oxygen and humidity value) are the main critical factors to obtain films with desired phase, crystallinity, and morphology.

Two-step solution deposition is, also known as the sequential deposition method, commonly used in researches to develop PSCs. A common two-step solution process involves spin-coating a PbI_2 seed layer on a substrate and then soaking in an MAI/isopropanol solution to transform it to $MAPbI_3$. Additionally, spin-coating was employed to incorporate MAI molecules into the PbI_2 network. In comparison to the single-step solution method, the two-step sequential deposition method produces perovskite films with more uniform and high density, resulting in achieving high-efficiency PSCs.

The vapor-assisted deposition is a modified two-step solution deposition method using the vapor deposition technique to introduce MAI rather than the solution method. This approach enables more precise control over the morphology and grain size of the film via gas-solid crystallization and efficiently prevents film delamination caused by liquid-solid contact. However, this process is restricted in use since the gas-solid interaction often takes tens of hours to complete, and devices manufactured using this method exhibit only a PCE of 10 - 12%.

Vapor phase deposition is a well-established technique for producing high-quality semiconductor thin films with homogeneous thickness and composition. This approach allows the production of pinhole-free uniform perovskite films. In comparison to solution-processed perovskite films, vapor-deposited perovskite layers may be deposited on TiO_2 and PEDOT:PSS layers conformally. Due to the limited thermal stability of both the precursors and the products, vapor deposition demands careful temperature control during deposition. As a result, a limited number of research groups have established the fabrication of high-efficiency devices using this method (Song et al., 2016).

2.3.2 Contact Layer

Designing a counter electrode for use in PSCs, the energy level and work function must be taken into consideration first, followed by electrical conductivity and stability. While V_{OC} and FF are directly connected to counter electrode performance, I_{SC} is just associated to the photogeneration and recombination efficiency of electrons in the perovskite and photoanode layers. Therefore, Electrode conductivity and interface resistance between electrode and HTM layer are critical characteristics affecting V_{OC} and FF. Although other low-cost counter electrode materials such as C, Al, Cu and TCO have been investigated recently as alternatives to Au and Ag, they are still the most preferred electrodes in the literature. It has long been known that energy levels between 5.1 and 4.1 eV are appropriate.

TCO glass is usually used as an electrode on the side where the photons come from. Not only do TCO materials like as ITO, FTO, IO:H, IZO, and AZO transmit electrons and holes, but they also permit the transmission of light. The most preferred TCOs are ITO and FTO for p-i-n inverted PCS (G. R. Li & Gao, 2020).

2.3.3 Electron Transport Material Layer

ETM have a vital role in determining total photovoltaic performance. The ETM's functional features may be listed as follows:

- Electron extraction from the absorber layer and transportation of them to the contact layer,
- Providing enhanced the coverage/contact area between the perovskite and the contact layer,
- Serving to block transportation of holes,
- Facilitating being scaffold to absorber layer in mesoporous ETMs
- Acting as a nucleation region for perovskite by affecting crystal growth and thus optoelectronic properties for n-i-p PSCs.
- Serving as a layer to resist moisture and barrier metal ions (Lin et al., 2021).

Both inorganic and organic ETMs are frequently used in PSC research, could be deposited in various methods. Inorganic ETMs are generally used in n-i-p PSCs, while organic ETMs are generally used in inverted p-i-n PSCs. The most preferred ETMs are TiO_2, SnO_2, ZnO for inorganic ETMs and PCBM, fullerene-C60 for organic HTMs (Lin et al., 2021).

2.3.4 Hole Transport Layer

HTMs are semiconductor materials showing p-type characteristics that provide hole movement and block the electrons in solar cells (Y. Zhang, Liu, Tan, & Gu, 2015). For these semiconductor materials to be employed as HTM, band gap values, optical characteristics, carrier mobility, and electron-blocking properties are crucial. The VBM/HOMO value of the HTM layer should be greater than value of the absorber layer to transfer the holes generated after the separation of the electron-hole pair as a result of excitation, from absorber layer to HTM, and then transparent conductive anode quickly. Additionally, CBM/LUMO value of the HTM layer should also be greater than value of the absorber layer, which also means being a wide bandgap, because of blocking of electron transportation to transparent conductive oxide essentially. This band configuration is very beneficial in preventing charge recombination (W. Yan et al., 2015).

HTM has been presented between the transparent conductive anode and perovskite layer in order to decrease energy losses at interface of the hole collection. Materials must have specific requirements as follows to be an HTM candidate.

- VBM/HOMO level of the HTM layers should match the perovskite layer, which facilitates to enhance the V_{OC} value of the solar cell.
- HTM layers are expected to have high mobility to transfer holes to the electrode effectively.
- HTM layers are expected to have high optical transmittance in the range where perovskite layer is effective, to prevent losses by blocking photons from passing through for inverted PSCs.

- HTM layers are expected to prevent to transfer electrons to the neighboring electrode.
- The HTM layers should isolate the perovskite layer from moisture in the air and at the same time separate it from the anode layer while not reacting with neighbors, for enhancing the device's stability by lowering the risk of corrosion and deterioration.
- For mass productions in the future, the deposition of the HTM layers should be applied through simple, low cost and practical methods.
- HTM layers should have low imperfections but as with NiO_x and CuO_x, its own imperfections that allow it to acquire positive properties can be ignored (Arumugam et al., 2021; S. Li, Cao, Li, & Bo, 2021; Salim et al., 2015).

Many researchers in the literature have studied on HTMs. In literature, it is seen that organic (spiro-OMeTAD, PEDOT:PSS, PTTA, P3HT, etc.) and inorganic (NiO_x, CuO_x, CuSCN, CuI, MoS_2,WS_2, etc.) materials have been used as HTM in perovskite cells (S. Li et al., 2021).

2.3.4.1 Organic HTMs

Spiro-OMeTAD was initially employed in PSCs in 2012 (H. S. Kim et al., 2012; M. M. Lee, Teuscher, Miyasaka, Murakami, & Snaith, 2012). It has a proper HOMO and LUMO level with appr 2.7 eV of bandgap, amorphous structure, and high T_g. Due to the relatively low hole mobility in spiro-OMeTAD, it could have some additives such as Li-TFSI and tBP to enhance mobility and hence the efficiency of solar cells. In addition to being the most common HTM in the studies, commercially available spiro-OMeTAD was used as the HTM layer even in the PSC with champion efficiency (25.6%) (Jeong et al., 2021). Even the stability is the biggest problem because of being organic, lots of studies also focused on the improve their stability with different additives (Pham et al., 2020; Sathiyan et al., 2020; Seo et al., 2018). The high cost and complex synthesis steps are the biggest barriers to the use of spiro-OMeTAD in commercial PSCs (Z. Hu et al., 2018).

PTAA also a prevalent HTM with nearly same situation with Spiro-OMeTAD for needing some additives to work effectively. For example, addition of Lewis acid dopant, efficiency was obtained as 19.01% with excellent fill factor of 0.81 while improving the stability of cell (Luo et al., 2018). Studies shows that PTAA could be used in both n-i-p and p-i-n architecture.

PEDOT:PSS is another HTM that is frequently employed in planar p-i-n PSCs. Although it has some advantages such as easy preparation and having low hysteresis, stability and performance involving V_{OC} and J_{SC} is rather low due to enormous energy barrier between absorber layer and PEDOT:PSS whose solution also has strong acidity. In the literature, PEDOT:PSS has been modified with different additives such as PSS-Na (Zuo & Ding, 2017), F4-TCNQ (D. Liu et al., 2017), and graphene oxide (Yu et al., 2018) to improve energy level matching with absorber layer, increase electrical conductivity, enhance optical properties, respectively.

P3HT is also promising organic material for HTM due to having high carrier mobility, optimal bandgap fitting with solar spectrum and cost-effective. Nevertheless, PSCs in which P3HT is used as HTM have low efficiency values due to its low conductivity of P3HT, therefore many studies have been carried out to enhance conductivity. As preferred in PEDOT:PSS, F4TCNQ was used as a dopant to improve conductivity and thus increasing the PCE value from 10.3% to 14.4% (Y. Zhang et al., 2016).

In addition to the most popular HTMs mentioned above, spiro-OMeTAD, PTAA, PEDOT:PSS and P3HT, many different organic molecules continue to be investigated as HTMs in the literature to achieve high efficiency and stability with low cost (S. Li et al., 2021).

Even though PSCs derived from organic HTMs demonstrate superior PCE, high acidity, tendency to absorb water (hygroscopicity) and inadequacy of blocking electrons negatively affect the long-term stability of PSCs. Exposure to environmental conditions, humidity, and UV-visible light during the work of organic HTMs impair

the structure and stability of these materials. A study shows that organic HTMs such as spiro-OMeTAD and PTAA are 23 - 57 times more costly than gold, limiting its commercialization (Sajid et al., 2018). For all these reasons, their long-term stability and commercialization potential is low despite their high theoretical efficiency (Nouri, Mohammadi, & Lianos, 2018).

2.3.4.2 Inorganic HTMS

Inorganic materials are inherently more stable to harsh environmental conditions, and their relative economics compared to organic materials increase their commercialization potential for using as HTM in PSCs. In a study, solar panel estimated costs were calculated for 1 m^2 area and it was found that average cost of PSC involved organic HTM and NiO_x HTM was 1800 \$/m^2 and 800 \$/m^2, respectively (Sajid et al., 2018). In addition, having ease of preparation and modification with different additives, and high hole mobility makes them attractive candidates for application in stable PSCs (Arumugam et al., 2021; Q. Wang et al., 2021). In the literature, the most used inorganic semiconductors as HTM are NiO_x, CuO_x, CuS, CuSCN, MoO_3, and V_2O_5, etc (Ye, Liu, Bian, & Huang, 2018).

Cu-based p-type semiconductor materials such as Cu_2O, CuO_x, $CuAlO_2$, CuS, CuI, CuP, CuSCN etc. are frequently used as inorganic HTMs in PSC researches thanks to exhibiting chemical stability high hole mobility and conductivity, appropriate energy level, and ease of deposition by solution process to obtain homogeneous films economically (Arumugam et al., 2021).

CuO and Cu_2O films prepared by low temperature methods in inverted PSCs enhanced J_{SC} and V_{OC} and in addition, where high crystalline perovskite layer was grown on top of them to improve carrier transport capability. As a result, 16.52 mA cm^{-2} for J_{SC}, 1.07 V for V_{OC}, 0.75 for FF and 13.35% for PCE were attained as a solar cell performance (Zuo & Ding, 2015). Homogeneous and pinhole-free Cu_2O thin films were deposited on the ITO/glass substrate by electrodeposition, and these thin films acted as growth points for the crystallization of the perovskite film. As a result, 18.03

mA cm^{-2} for J_{SC}, 0.88 V for V_{OC}, 0.61 for FF and 9.64% for PCE were accomplished as a solar cell performance (L. Liu et al., 2016).

CuS also widely used in gas sensors and organic solar cells, were applied by spin-coating technique to PSC with ITO/CuS/$MAPbI_3$/C60/BCP/Ag architecture. Although VBM (from -4.9 to -5.1 eV) of ITO was well-matched with VBM (-5.4 eV) of $MAPbI_3$ thanks to modified by CuS NPs, there was no positive change in surface roughness and transmittance. With spin-coating optimization, the maximum PCE of 16.2% was reached with J_{SC} of 22.3 mA cm^{-2}, VOC of 1.02 V, and FF of 0.69 (Rao et al., 2016). In another study, CuS NPs was accumulated by dynamic spin-coating as HTM layer in n-i-p PSCs where $MAPbI_3$ or CsFAMAPbIBr was utilized as absorber layer, while TiO_2 was used as ETM layer. The performance of solar cells was compared by replacing only the HTM layer with spiro-OMeTAD, leaving the other layers the same. While the efficiency of $MAPbI_3$ and CsFAMAPbIBr was 13.47% and 11.85%, respectively, in cells in which CuS was used as HTM, these values were measured as 17.41% and 15.5%, respectively, in cells using spiro-OMeTAD instead of CuS (Tirado et al., 2019).

CuSCN has inherent benefits, such as high chemical stability and ease of manufacture, and exhibits exceptional transparency in the visible spectrum. However, the solvent diethyl sulfide (DES), which is frequently employed in solution processing of CuSCN, might deteriorate the perovskite layer, therefore researchers are attempted to synthesize CuSCN-based PSCs with a p-i-n structure because of limits on forming n-i-p structure (S. Li et al., 2021). In one study, a p-i-n cell was formed by growing CuSCN by electro-depositing method and using $MAPbI_3$ as the absorbing layer. The maximum efficiency of the cell was measured as 16.6% with V_{OC} of 1.00 V, FF of 0.76, J_{SC} of 21.9 mA cm^{-2}, with the positive effect of great hole mobility of CuSCN and low surface stability and contact resistance in $MAPbI_3$ coated on it (Ye et al., 2015). In another study, to mitigate the deterioration by diethyl sulfide, CuSCN was coated using fast solvent removal procedure which permitted the formation of compact, conformal layers that ease extract and collect carriers. The PSC which involving reduced graphene oxide between CuSCN and Au showed 20.4% of

efficiency and also retained greater than 95% of their initial efficiency after 1000 hours of operation at maximum power point at full sun intensity at 60°C (Arora et al., 2017).

NiO_x has found a wide range of use as HTMs in perovskite solar cells thanks to its many suitable properties. In the next section, the structure and properties of NiO_x and its usage in PSC, both undoped and doped, will be discussed in detail.

2.4 Nickel Oxide

NiO_x is a well-known p-type semiconductor with wide band gap (3.6 - 4.0 eV) which takes place in different applications, including anti-ferromagnetic materials, lithium-ion batteries, chemical gas sensors, transparent layers in smart windows, solar cells, etc. due to its exciting electrical, optical, magnetic, catalytic, electrochromic features. Moreover, it exhibits improved thermal and chemical stability while it is plentiful in the earth with low-cost and synthesizable using cost-effective processes. Nickel oxide in a form of powder, bulk or thin film can be manufactured using various methods such as pulsed laser deposition, electrodeposition, spin coating, sol-gel, thermal decomposition, and spray-pyrolysis (Akalin, Erol, Uzunbayir, Oguzlar, & Yildirim, 2021).

NiO_x is a non-stoichiometric ($_x$) rock salt (NaCl-type) structure with a space group of Fm3m and a lattice parameter of 0.4173 nm (Ye et al., 2018). The change in non-stoichiometry value is be associated with a color change. The value change in non-stoichiometry is be abetted with a color change, as the other binary metal oxides have. The stoichiometric NiO is green while the non-stoichiometric one is black (Dubey & Kaurav, 2020).

NiO_x typically accumulates an excess of oxygen during the thermal treatment process, which is quickly compensated for by the oxidation of some Ni^{2+} to Ni^{3+}, forming nickel vacancies and interstitial oxygen in NiO_x crystallites. Typically, during the thermal treatment process, NiO_x procures excess oxygen which enters as O^{2-} ions, however, due to the lack of sufficient space in the structure, this creates nickel

vacancies at cation sites and hence, $Ni_{1-x}O$. When compared with the stoichiometric NiO, Ni^{2+} vacancy corresponds to a charge of -2e and thus two holes. Therefore, in the situation of excess oxygen, Ni^{3+} ions can be formed which involves a Ni^{2+} and an extra hole, it can be described as follows:

$$Ni^{3+} \rightarrow Ni^{2+} \rightarrow h \tag{2.1}$$

The Kröger-Vink notation is utilized to depict the locations and electrical charge states of point defects in the crystal. In this notation, a defect is denoted by a major symbol, and the occupied site is denoted by a subscript. M_M and O_O describe that metal atom is on a normal metal lattice and oxygen ion is on a regular oxygen lattice, respectively. The V is used to indicate vacant positions, for example, V_M describes metal vacancy. The subscript "i" defines interstitial position while superscript “dot”, “prime”, and “x” describes the positive charge, negative charge, and zero charges, respectively (Kofstad, 1995). The non-stoichiometric state of nickel oxide can be represented by Kröger-Vink notations as follows:

$$2Ni_{Ni}^{X} + \frac{1}{2}O_2(g) \rightarrow 2Ni_{Ni}^{\bullet} + O_O^X + V_{Ni}''\bullet \tag{2.2}$$

Where Ni_{Ni}^{X} is Ni^{2+} ions, $V_{Ni}''\bullet$ is Ni^{2+} vacancy, and $Ni_{Ni}^{\bullet}$ is Ni^{3+} ions. This relation defines that the reaction of two Ni^{2+} ions (Ni_{Ni}^{X}) with oxygen results in the formation of a nickel vacancy ($V_{Ni}''\bullet$) and two Ni^{3+} ions ($2Ni_{Ni}^{\bullet}$) in the NiO crystal. The relation clearly shows that each Ni^{3+} formed from the vacancy of Ni^{2+} increases the holes in NiO_x, hence p-type properties. (Dubey & Kaurav, 2020; Nandy, Saha, Mitra, & Chattopadhyay, 2007; Soo Kim & Chul Lee, 2012).

The schematic representation of the non-stoichiometric NiO is shown in Figure 2.17. Due to the excess of oxygen, the number of Ni^{2+} and O^{2-} ions is unequal, therefore some Ni^{3+} ions are formed to make the system as neutral-charge, the final nickel oxide can be represented as follows:

$$[Ni_{1-3x}^{2+} V Ni_{2x}^{3+}]O \tag{2.3}$$

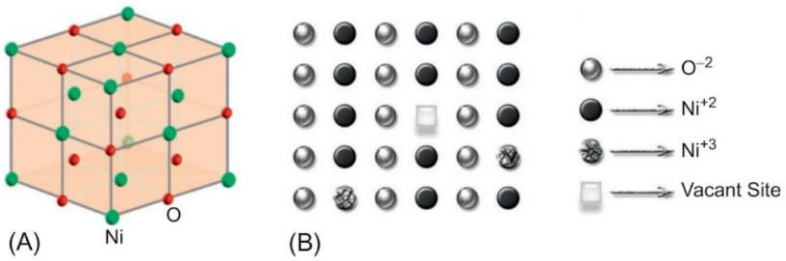

Figure 2.17 Illustration of a) cubic structure and b) ions and vacancies of NiO_x (Ye et al., 2018)

Dopants contributed to the increase in the concentration of crystal imperfections can be shown a similar effect. The ions of dopants are selected close to the ionic radii of metal ions to locate on cation lattice sites however have a different valence. The excess or deficit charge of impurity ions is atoned by more metal vacancies, interstitials, or valance differences in the crystal structure; hence electrons or holes concentration is improved. Thus, the hole mobility can be easily adjusted by increasing the number of nickel vacancies and/or interstitial oxygen and/or by doping with monovalent atoms such as lithium (an increase in the amount of Ni^{3+}) (Dirksen, Duval, & Ring, 2001). The inherent p-type characteristic of being non-stoichiometric has made wide usage opportunities for doped or undoped NiO_x as HTMs in PSCs.

In its first trial of NiO via spin coating in PSCs in 2013, despite the fact that NiO quenches the perovskite steady-state PL better than spiro-OMeTAD, the cell with FTO/NiO_x/$MAPbI_{3-x}Cl_x$/PCBM/Al architecture gave poor performance due to the insufficient surface coating of the perovskite film with the possibility of the ETM layer directly contacting the HTM layer (Docampo, Ball, Darwich, Eperon, & Snaith, 2013).

Afterward, a two-step sequential dipping method for $MAPbI_3$ was studied to obtain improved film quality in an ITO/NiO_x/$CH_3NH_3PbI_3$/PCBM/Al solar cell, while NiO_x film was spin-coated. With the UVO treatment, the surface adsorbents, on which NiO_x adsorbed carbonaceous species and other atmospheric pollutants in storage, were removed to reveal a clean NiO_x surface and thus increased the work function of NiO_x. As a result, the best cell was achieved with the NiO_x thickness of 10.2 nm and performance values were PCE of 7.6%, V_{OC} of 1.05 V, J_{SC} of 15.4 mA cm^{-2}, and FF of 0.47 (L. Hu et al., 2014).

Wang and coworkers have investigated the effects of film thickness and oxygen flow rate in the low-temperature RF sputtering deposition of NiO_x on the performance of mesoscopic $NiO/CH_3NH_3PbI_3$. The champion efficiency was achieved 11.6% and the other photovoltaic characteristics were V_{OC} of 0.96 V, J_{SC} of 19.8 mA cm^{-2}, and FF of 0.61, obtained with NiO_x films deposited with 10% oxygen flow ratio ($O_2/Ar + O_2$) for 150 s (K. Wang et al., 2014).

In the other study, pulsed laser deposition was utilized to obtain improved optical transparent well-ordered NiO nanostructured film on the ITO substrate. $ITO/NiO_x/MAPbI_3/PCBM/Al$ solar cell photovoltaic parameters were V_{OC} of 1.06 V, J_{SC} of 20.2 mA cm^{-2}, and FF of 0.81 and achieved PCE of 17.3% with optimized NiO film in which oxygen partial pressure of 200 mTorr at deposition time for 100 - 180 nm thickness were applied on production (Park et al., 2015).

Wang and colleagues applied (UVO) treatment to reduce the surface energy thus enhancing crystallinity and surface coating of NiO_x which was produced with electrochemical deposition method onto the FTO substrate. UVO treatment improves the wettability of the surface, electrical conductivity, and work function of NiOx film, as a result, $FTO/NiO_x/MAPbI_3/PCBM/BCP/Ag$ solar cell exhibited the best PCE of 19.67% with FF of 0.75 J_{SC} of 23.39 mA cm^{-2} and V_{OC} of 1.11 V after 5 minutes UVO treatment of NiO_x film (T. Wang et al., 2019).

As expressed in the previous section explaining the effect of defects in crystal structure on hole conductivity of NiO; extrinsic doping which means doping with other atoms is referred as an effective way to improve hole conductivity by creating defects in the structure.

Monovalent alkali metal ions have been utilized as a dopant in order to improve the electrical conductivity of NiO_x. Li^+ can be conveniently doped into the lattice site of Ni^{2+} thanks to close ionic radii of Li^+ (0.76 Å) and Ni^{2+} (0.69 Å). Therefore, Ni^{3+} concentration is increased, which promotes conductivity due to free holes moving through the lattice (Ma et al., 2021). With this approach, Nie and friends investigated

Li doped NiO_x film at different molar ratios as 0%, 2%, 5%, 10%, and 20% in FTO/Li:NiO_x/$MAPbI_3$/PCBM/Al cell via spin coating. It was found that, with the Li^+ doping, it substituted with Ni^{2+} vacancy, therefore increasing the conductivity of NiO, hence directly affecting the performance of the device positively. The PCE was enhanced by almost 40% (from 11 ± 0.85% to 17.43 ± 0.44%) with 5 at% lithium doped NiO device, with V_{OC} of 1.12 V, J_{SC} of 21.79 mA cm^{-2}, and FF of 0.74, without any other phases of lithium (Nie et al., 2018).

In another study, the effect of doping lithium into NiO_x thin films produced by PLD was studied with different annealing temperatures and doping amounts. The focus of this study was the impact of annealing time from 100 °C to 450 °C, partial pressure of oxygen from 0% to 100%, film thickness from 7 nm to 90 nm, and finally 0.1 and 0.2% Li additive on cell performance. As a result, ITO/Li:NiO_x/$MAPbI_{3-x}Cl_x$/PCBM/Ag solar cell exhibited PCE of 15.51%, V_{OC} of 1.06 V, J_{SC} of 22.87 mA cm^{-2}, and FF of 0.64 with 0.1% lithium incorporation which was improved by about 23% from pristine NiO_x post-annealed at 450 °C (Qiu et al., 2017).

Kim et al established the contribution of Cu doping into NiO_x to the efficiency of p-i-n PSCs for the first time in 2014. Both NiO_x and 5 at% Cu:NiO_x was applied by spin coating on the ITO substrate. The electrical conductivity was significantly increased (8.4×10^{-4} S cm^{-1}) upon 5 at% Cu doping compared to pristine NiO_x (2.2×10^{-6} S cm^{-1}). In addition, perovskite film had an improved degree of PL quenching onto the Cu:NiO_x film compared to pristine NiO_x, showing that Cu:NiO_x has a higher hole collection and transport efficiency, resulting in a rise of JSC and FF. As a result, ITO/NiO_x/$MAPbI_3$ or $MAPb(I_xBr_{1-x})_3$/PCBM/Ag configured solar cell exhibited PCE of 15.40%, V_{OC} of 1.11 ± 0.01 V, J_{SC} of 18.75 ± 0.42 mA cm^{-2}, and FF of 0.72 ± 0.01 (J. H. Kim et al., 2015)

On the other study, pristine NiO_x and Cu:NiO_x with different power values (5W, 10W, 15W, 20W, and 25W) were deposited on FTO substrates by DC magnetron sputtering using nickel and copper targets and employed in FTO/NiO_x or Cu:NiO_x/$MAPbI_3$/PCBM/Ag configured PSC. The best efficiency of 14.96% was

obtained with 5 at% Cu doped NiO_x film, with a thickness of around 20 nm, produced in 2 minutes with 15 W doping power while it was 9.60% for the pristine film. The photovoltaic performance parameters were V_{OC} of 1.005 V, J_{SC} of 19.08 mA cm^{-2}, and FF of 0.69 (A. Huang et al., 2018).

Ge and coworkers investigated the effect of doping with alkaline earth metal such as Mg, Ca, Sr, and Ba on valance band position of NiO_x. All films (pristine and doped with 5 mol% for each additives) were prepared by spin-coating, heated at 150 °C for 5 min and annealed at 500 °C for 1 h. The hole conductivity was increased and VBM position was downshifted thanks to alkali metals in NiOx matrix. As it can be seen that VBM positions were calculated -5.04, -5.19, -5.29, -5.34 and -5.18 eV for pristine, Mg, Ca, Sr, and Ba doped NiO_x, respectively, the highest downshifting (0.30 eV) occurred with Sr doping film (-5.34 eV), which is advantageous for band alignment with $MAPbI_3$ (-5.4 eV). As a result, FTO/Sr:NiO_x/$MAPbI_3$/PCBM/BCP/Ag configured device exhibited the best PCE of 19.49% with V_{OC} of 1.14 V, J_{SC} of 22.66 mA cm^{-2}, and FF of 0.75. The other cell efficiencies with different HTM layers were 16.65% for pristine, 18.29% for Mg:NiO_x, 18.75% for Ca:NiO_x, and 17.94% for Ba:NiO_x (Ge et al., 2019).

As discussed above, although the utility of single element doping to improve the conductivity and band alignment of NiO_x is recognized, co-doping of multi-elements has been taken into account for further development.

In this regard, Chen et al focused on a co-doping strategy based on Li, Mg doped NiO_x with different ratios such as $Mg_{0.15}Li_{0.05}Ni_{0.80}O$, $Mg_{0.15}Ni_{0.85}O$ and $Li_{0.05}Ni_{0.95}O$ produced by spray-pyrolysis method. It was observed that only Li doping kept CBM value (-1.6 eV) constant while upshifting VBM value (-5.1 eV) resulting in the band gap from 3.6 to 3.5 eV, while only Mg doping caused the band gap (3.95 eV) to widen by upshifting of CBM value (-1.4 eV) and downshifting of VBM value (-5.35 eV). Therefore, in the Li, Mg codoped structure, Li was responsible for the downshifting of the VBM while Mg was associated with the upshifting of the CBM and thus the bandgap was 3.85 eV. As a result, FTO/$Mg_{0.15}Li_{0.05}Ni_{0.80}O$/$MAPbI_3$/Ti(Nb)$O_x$/Ag

configurated cell exhibited the certified results such as the PCE of 15%, V_{OC} of 1.09 V, J_{SC} of 20.96 mA cm^{-2}, and FF of 0.67 for 1.017 cm^2 cell size (W. Chen et al., 2015). As a continuation of the previous work, Xie et al. achieved 20.65% efficiency using the same HTM layer with FTO/LiMgNiO_x/$FAPbI_3$(MACl treated)/PCBM/TiO_x/Ag solar cell with V_{OC} of 1.10 V, J_{SC} of 23.09 mA cm^{-2}, and FF of 0.81 and reached high stability tested 500 h light soaking aging test (Xie et al., 2017).

Liu and friends investigated the performance comparison of Li,Cu codoped NiO_x with pristine and mono-doped NiO_x in perovskite solar cell application, in which all HTM layers prepared by spin coating on FTO, heated at 150 °C for 5 min, then annealed at 500 °C for 30 min. Sample ratios were determined as pristine NiO_x, 3 at% Cu:NiO_x, 5 at% Cu:NiO_x, 2 at% Li, 3 at% Cu:NiO_x. When comparing carrier mobility of samples, the results were measured as 100.9 cm^2 V^{-1} s^{-1} and 165.9 cm^2 V^{-1} s^{-1} for 5 at% Cu:NiO_x and 2 at% Li, 3 at% Cu:NiO_x, respectively, which was attributed to electrical conductivity, hence efficiency of charge extraction, resulting in improved J_{SC} and FF. As a result, the best efficiency was measured 14.53% for FTO/LiCuNiO_x/$MAPbI_3$/PCBM/Ag configuration. The photovoltaic parameters were V_{OC} of 0.961 V, J_{SC} of 20.8 mA cm^{-2}, and FF of 0.73 (M.-H. Liu et al., 2016).

In addition, there are many studies to deposit a thin film of NiO_x in the perovskite solar cell as an HTM layer in the literature with pristine or different dopants (single, double, or more together), using different production methods such as physical vapor deposition methods, sol-gel, spin coating, and electrodeposition, etc. Some of them are listed in Table 2.1.

In comparison to solution-based methods, magnetron sputtered films have some advantages to being more homogenous and compact on an infinite number of substrates (with different sizes and flexibility). The film thickness is accurately regulated on the angstrom scale, allowing for mass manufacturing with high consistency (A. B. Huang et al., 2016). Although solution-based structures allow for precise stoichiometry control, their homogeneity, surface roughness, and mechanical characteristics are inferior to those produced using vapor-based approaches and

resulting directly affecting sustainable mass production (Zayim, Turhan, Tepehan, & Ozer, 2008).

Table 2.1 Studies on HTMs used in PSCs

HTM	Deposition Method	PSK/ETM	V_{OC}	J_{SC}	FF	PCE	REF
Spiro-OMeTAD	Spin coating	$FAPbI_3/TiO_2$	1.19	26.35	0.82	25.59	(Jeong et al., 2021)
PTAA	Spin coating	$MAPbI_3/TiO_2$	1.05	22.35	0.81	19.01	(Luo et al., 2018)
PEDOT: PSS	Spin coating	$MAPbI_3$/PCBM	1.11	18.44	0.76	15.56	(Zuo & Ding, 2017)
P3HT	Spin coating	$(FAPbI_3)_{1-x}$ $(MAPbBr_3)_x$ $/TiO_2$	0.97	23.9	0.62	14.40	(Y. Zhang et al., 2016)
CuO	Spin coating	$MAPbI_3$/PCBM	1.06	15.82	0.73	12.11	(Zuo & Ding, 2015)
Cu_2O	Spin coating	$MAPbI_3$/PCBM	1.07	16.52	0.75	13.35	(Zuo & Ding, 2015)
CuS	Spin coating	$MAPbI_3$/ C60/BCP	1.02	22.3	0.69	16.2	(Rao et al., 2016)
CuSCN	Electro-deposition	$MAPbI_3$/ C60/BCP	1.00	0.76	21.9	16.6	(Ye et al., 2015)
NiO_x	Spin Coating	$MAPbI_3$/PCBM	1.05	15.4	0.47	7.6	(L. Hu et al., 2014)
NiO_x	RF-magnetron sputtering	$MAPbI_3$/PCBM	0.96	19.8	0.61	11.6	(K. Wang et al., 2014)
$LiNiO_x$	Spin coating	$MAPbI_3$/PCBM	1.12	21.79	0.74	17.43	(Nie et al., 2018)
$LiNiO_x$	PLD	$MAPbI_{3-x}Cl_x$/PCBM	1.06	22.87	0.64	15.51	(Qiu et al., 2017)
$CuNiO_x$	DC-magnetron sputtering	$MAPbI_3$/PCBM	1.01	19.08	0.69	9.60	(A. Huang et al., 2018)
$MgLiNiO_x$	Spray pyrolysis	$MAPbI_3/Ti(Nb)O_x$	1.09	20.96	0.67	15.00	(W. Chen et al., 2015)

V_{OC}: V, J_{SC}: $mA.cm^{-2}$, PCE: %

2.5 Physical Vapor Deposition

Terminology of “thin-film” can be described as a structure produced by coating, depositing, evaporating, etc. with a thickness from a nanometer to several microns on top of the various substrates. Saving scarce materials with less material usage, thus minimizing dimensions with enhanced performance are the biggest known advantages of utilizing thin-film structures (Sönmezoğlu, Koç, & Akın, 2012). Except for coating operation, deposition and evaporation processes are operated in a high vacuum. The production methods of thin films are mainly divided into three categories: chemical solution deposition, chemical vapor deposition, and physical vapor deposition. CSD is the type of coating to form films whereby solutions composed from chemical precursors dissolved or suspended in a solvent are coated on the substrate and heated to result in the desired film (Dorey, 2012). CVD is a technique to deposit thin films on the substrate which are exposed with volatile precursors undergoing chemical reactions, generally at high temperatures (Martin, 2010). PVD is the deposition process in a vacuum below 10^{-4} Pa to produce a thin film from solid material on the substrate with the controllable thickness in Å (10^{-10} m) value. PVD consists of two categories: thermal evaporation and sputtering.

In the thermal evaporation method, source materials are heated resistively in the filament or the boat generally made from materials with low evaporation rates and low vapor pressures such as W, Mo, and Ta, and as a result, atoms of source materials evaporate with having 0.1 - 0.3 eV kinetic energy and deposit on the substrate without any collision thanks to a high vacuum environment (Figure 2.18) (Adachi & Wasa, 2012).

Sputter deposition is a technique to produce a thin film on the substrate with sputtered atoms with high kinetic energy from the target material surface due to bombarding by energetic ions of gas or plasma accelerated in an electric field, shown in Figure 2.19 (Mattox, 2010). DC, RF, magnetron, and ion beam sputtering are all examples of sputtering systems that are employed in practice, shown in Figure 2.20.

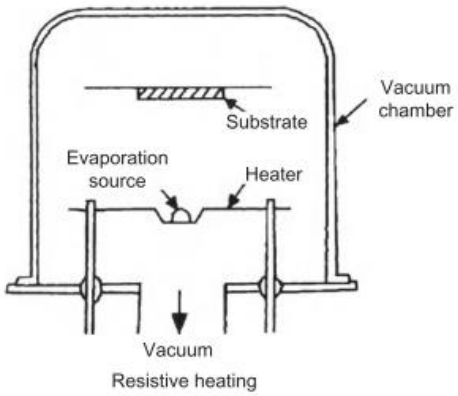

Figure 2.18 Schematic representation of the thermal evaporation system (Adachi & Wasa, 2012)

The DC diode sputtering system consists of two electrodes in which the anode and cathodes are arranged planarly, on which the substrate and target materials are placed, respectively. The chamber filled with inert gas, generally Ar at 1 - 5 Pa after being highly vacuumed. Glow discharge is taken place after applying voltage from DC-diode and ionizes Ar gases. Ar^+ ions sputter atoms from target materials as a result of accelerated to a negatively charged target material and sputtered atoms are deposited on the substrate as a thin film. In DC sputter systems, metal target materials are used to maintain glow discharges between metallic electrodes. For insulator/semiconductor target materials that are desired to be deposited as insulator/semiconductor thin films, RF sputtering systems using RF voltage suppliers are effective.

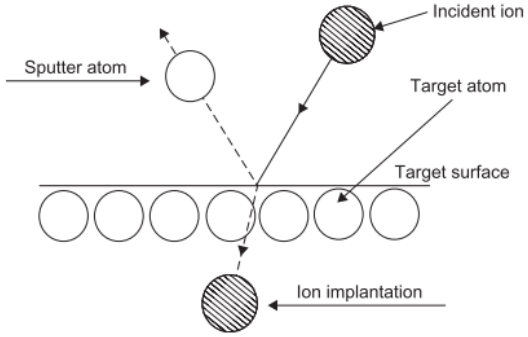

Figure 2.19 Ion-target interaction in the sputtering process (Adachi & Wasa, 2012)

Sputtering methods deposit material at a slower pace than thermal evaporation. Deposition rates are increased when the sputtering pressure is reduced. The magnetron-type discharge is used to lower the sputtering pressure, as shown in Figure

2.20. The magnetron sputtering system contains magnetic coils below the cathode side where the target material is placed, which creates a magnetic field that causes cycloidal movement of electrons in the glow discharge. The collision rate between electrons and gas molecules rises with increasing the number of trapped electrons via the magnetic field. Plasma density that triggers an increase in the current density is raised by the magnetic field, which causes an increase in the sputtering rate at the target material. The sputtered particles pass through the discharge space without colliding due to the low working gas pressure, resulting in a rapid deposition rate.

Reactive sputtering is a method of depositing composite thin films as a result of the reaction of sputtered atoms with reactive gas molecules, essentially in the form of two-dimensional collisions on the substrate. Reactive sources are divided into two categories: gas and solid. The gas source which includes elements beget compound thin film while the target material is metal, alloy, or other mixtures could be a pure reactive or reactive/inert gas mixture given in Table 2.2. Standard sputtering systems, such as DC or RF (or/non) magnetron sputtering, are used to perform reactive sputtering (Adachi & Wasa, 2012).

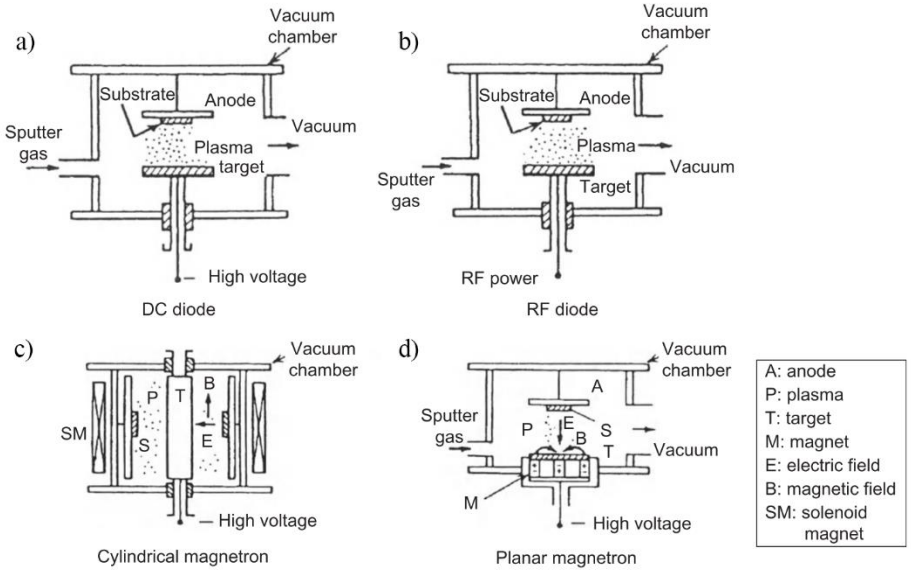

Figure 2.20 Schematic presentation of sputtering system with a) DC-diode, b) RF-diode, c) cylindrical magnetron, and d) planar magnetron (Adachi & Wasa, 2012)

Table 2.2 Gases used in reactive sputtering system (Adachi & Wasa, 2012)

Compound	Reactive Gas or Liquid
Oxide	Air, O_2, or H_2O
Nitride	N_2 or NH_3
Oxy-nitrides	$O_2 + N_2$
Sulfides	H_2S
Carbides	C_2H_2 or CH_4
Fluorides	HF or CF_4
Arsenide	As

Sputtering provides several benefits over other conventional evaporation processes. Additional advantages of RF magnetron sputtering include the ability to employ non-conductive targets, charge-up effects, and less arching owing to the alternating electric field. The most valuable advantage of the RF magnetron sputtering system that should be emphasized is the deposition of thin films using non-conductive target materials without a need to be melted or evaporated. Magnetron sputtering is widely utilized in the semiconductor industry for the deposition of a variety of materials necessary for the manufacturing of integrated circuits. Magnetron sputtering is widely utilized in the semiconductor industry for the deposition of a variety of materials from target materials (Maurya, Sardarinejad, & Alameh, 2014).

2.6 Production of Target Material

Powder metallurgy is a manufacturing process that uses temperature and pressure to convert metal, ceramic, and alloy powders generated through mechanical and chemical techniques into engineered products. Acquiring powders, pre-forming them to desired shapes, sintering for achieving properties, and reaching to final product by post-sintering are the most important steps of powder metallurgy (Upadhyaya, 2002).

The final product properties are direct regards to the sintering parameters, which in powder metallurgy are affected by the size, shape, and chemical composition of the powders mainly composed of metals, ceramics, or alloys, therefore not all production method is appropriate for all applications (Upadhyaya, 2002). There are different production methods that use mechanical, chemical, and physical approaches.

The sol-gel process is a wet-chemical technique that is the most applied method in both research and production areas, especially in the production of inorganic ceramic powders. The main advantage of this technique is that inorganic oxide powders with the desired properties such as hardness, optical transparency, chemical durability, porosity, and chemical resistance, etc. can be easily produced with simple equipment without the need for very high temperatures, therefore this technology is involved in an increasing number of applications in several fields of science and engineering (Toygun, Köneçoğlu, & Kalpaklı, 2013).

The term sol-gel consists of the two important steps of this technique, the sol and gel processes. Sol is a colloidal particle suspension in a liquid or a polymer molecule solution. For the presence of a sol, the liquid should be less intense than the solid particles in which, colloids range from 1-1000 nm are made. The gel is a three-dimensional porous network with a high-density dispersion of solids containing liquid components and liquids. The bonding of the smallest solvent particles and the dissolved particles is a crucial criterion for the formation of the gel. The sol-gel process consists of several steps, in order of execution: hydrolysis, polycondensation, gelation, aging, drying, condensation, and crystallization. In the first step of the sol-gel process, known as hydrolysis, the precursors defined in two main groups, metal salts, and alkoxides, are hydrolyzed in the solvent associated with the precursors, which is water or the proper alcohol. Condensation, also known as polycondensation, is the second step of the sol-gel process, from which different types of structures such as powders, finers, thin films, amorph bulk, and monolithic solid can be produced. The final product is obtained by eliminating the organic groups from the structure with the help of heat treatment (Neacşu, Nicoară, Vasile, & Vasile, 2016). Nature and concentration of precursors, type of solvent and acidity of the medium, the concentration of each type of insolvent, type and concentration of additives, the aging time of gel, and temperature can influence the sol-gel process (Toygun et al., 2013).

Although hydrolysis can take place without the catalyst, the reaction can be concluded much more quickly and accurately when a catalyst is added. The pH of the solutions, as well as the structure and concentration of the catalyst utilized, have a

considerable impact on the hydrolysis and condensation processes. The formation of the sol takes place because of peptization, which is affected by the type of acid, used during hydrolysis. Weak or non-complex acids are often efficient in the creation of sols. Catalysts such as ammonia and mineral acids are commonly employed. Acetic acid, hydrofluoric acid, potassium hydroxide, potassium fluoride, and amines are some of the other substances employed. The choice of an acid or basic catalyst is recognized to be the most crucial factor determining the pace of hydrolysis process. It is stated in the literature that the low pH of the sol rises the gelation time and the acid-catalyzed sol-gel technique generates a linearly or randomly branched polymer, whereas the base-catalyzed creates a high-density particle structure. The effect of pH on reaction rate, as well as all other characteristics, expedite for researchers to adjust research parameters and achieve the ideal end product configuration (Toygun et al., 2013).

Gelation can be defined as a state resembling the freezing process in which a solution suddenly loses its fluidity and turns into an elastic solid. The microstructure of the gels, and hence the final product, can be adjusted depending on the pace and form of the gelation reactions. Clusters expand and bond due to hydrolysis and condensation and form a gel. Since gelling time is one of the crucial factors of the process to acquire the low density and porous products, this step, where the size and shape of the last product are determined, must be well controlled. The particle density is known to rise as the gelation duration increases. Because gelation is caused by hydrolysis and condensation processes, every parameter that influences these reactions has a direct impact. To prepare a proper inorganic structure, the hydroxyl and organic residues in the gel must be destroyed. When the volatile substances in the pore are cut off in order to destroy the formed pores, the gel starts to swell and this generates the structure of the gel to deteriorate (Dilsiz & Akovali, 2002). When compared to alternative powder production technologies, the sol-gel process offers several benefits. The following are some of the benefits:

- Except for the condensation, all of the stages need low temperatures, which are typically near to room temperature. As a result, the danger of thermal deterioration is reduced, high purity and stoichiometry may be achieved.

- The majority of the first starting materials, such as metal alkoxides and mixed alkyl/alkoxides, are volatile. This assures the product's high purity.
- The procedure has mild chemical conditions. Acids and bases catalyze hydrolysis and condensation. Organic structures with pH sensitivity, as well as biological species including enzymes and all cells, can be preserved and continue to operate using particular procedures.
- This method may be used to make high-porosity and nanocrystalline materials.
- Pore size and mechanical strength may be adjusted by adjusting the aging and drying conditions.
- Because liquid precursors are employed, ceramic materials may be cast into a variety of complicated forms and thin films can be produced without the requirement for processing or melting.
- Because the sol-gel technique uses a low temperature, it can produce uncommon amorphous materials that are below the crystallization temperature of oxide materials (Brinker & Scherer, 2013).

Pre-forming is the process of forming the powders into the desired shape according to the shape of the mold by applying pressure to a mold. This pressed item, known as a green compact, formed by the cold fusion of the powder grains in the mass, gains strength as a result of the performing process. This strength is required during the process of removing the green compact from the mold and transferring it to the furnace. The final shape and mechanical characteristics. are associated density level and uniformity of the green compact.

Powders do not act as liquids in the press; pressure is not uniformly distributed throughout the structure, and only a limited amount of powder runs along the mold wall. Therefore, effective part density depends on the design of mold and equipment. In the first stage, it is assumed that each grain contacts its neighbors, but no bond has yet been made around the powders. The particles place into the mold, alter shape, and mechanical bonding happens as pressure is applied. The density and the strength following compression are referred to as raw density and raw strength, respectively.

Due to the increased hardness of the pieces as a result of deformation, greater pressure must be employed to keep on pressing (Sarıtaş, Türker, & Durlu, 2007).

Pre-forming processes, depending on the application of heat during pressing, are divided into two main groups as hot and cold. Manufacturing methods are isostatic (hot), extrusion, die compacting, spraying, and pressureless sintering under the hot categories, while die compacting, isostatic (cold), rolling injection molding, slip casting, and slurry casting are under the cold category.

Isostatic pressing is a powder forming process that applies equal pressure in all directions to a powder compact, which provides better density and microstructure homogeneity without the geometric restrictions of uniaxial pressing. Isostatic pressing can be performed in two ways: cold isostatic press or hot isostatic press which is used to press parts at ambient temperatures or to joint parts at high temperatures through solid-state diffusion, respectively. In other words, whereas the sintering process is essential for products following CIP, it is not necessary for the HIP (Kuşoğlu, 2011). The schematic demonstration of isostatic pressing by CIP is shown in Figure 2.21.

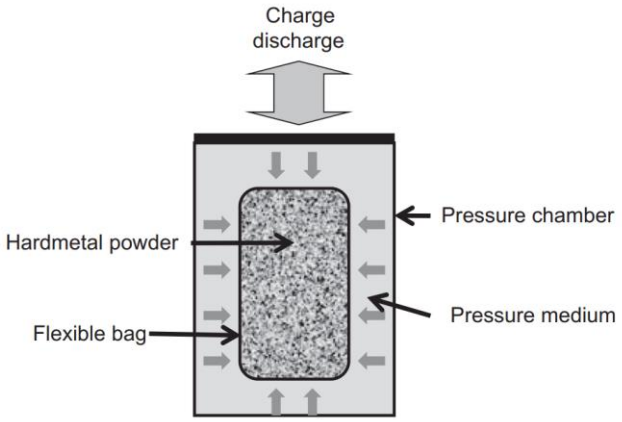

Figure 2.21 The schematic demonstration of CIP instrument (Mehrotra, 2014)

Sintering is a thermal process that is carried out at a temperature of about 0.4-0.9 of the melting temperatures of the materials, in a controlled atmosphere, at a certain temperature and time, by means of diffusion, which allows the particles of green parts to be bonded together. Sintering enlarges the contact areas of the powders, resulting in

material transport to reduce the specific surface area and pore volume of the porous powders, which gives integrity to the compact structure by the bonding of particles generated by the diffusion of atoms. Furthermore, shrinkage occurs during sintering which causes the part to condense. After the sintering process, increment of densification and strength takes place in the green compact.

Smaller particles have a higher surface area, hence higher surface energy, which means that the surface energy per volume of a particle is inversely proportional to its size. Smaller particles require less time to sinter thanks to their higher surface energies, even if all of them do not be relayed to sintering. Almost every particle contact surface of neighbors in crystalline solids results in the formation of grain boundaries. Therefore, neck growth reduces surface energy with increasing grain boundary energy (German, 2005).

Solid-state sintering and liquid phase sintering are the two distinct processes of sintering. Additionally, various methods such as spark sintering, microwave sintering, and laser sintering are used in specific applications. In solid state sintering, material transport carries out by diffusion, thanks to the driving force created by the free energy or chemical potential difference between the neck region and the powder surface.

Compared to liquid phase sintering solid phase sintering, not all particles in the structure are solid, one of the phases is viscous at the sintering temperature. This is particularly realized when sintering materials with widely disparate melting temperatures. The solid particles are wetted by the liquid phase, resulting in significant capillary pressure in the narrow channels between them. The quantity of capillary pressure is higher in fine particles, making sintering easier. In silicate systems, liquid-phase sintering is commonly used (German, 2010). Demonstration of neck formation and coalescence for particles in sintering process is shown in Figure 2.22.

In the compressed condition, there exist contact sites between the particles. Larger pores form between small grains. The atomic interaction and transport between the particles increases during the sintering process, and neck development occurs. Thus,

grain size increasing with the decreases of the pore size (Figure 2.23). At the contact locations, one boundary grows instead of the solid-vapor interface. Two particles are totally merged to create a single grain in the last stage of the sintering process.

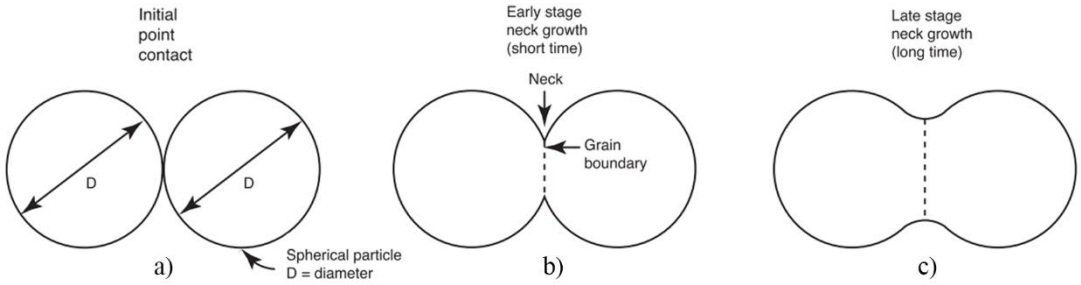

Figure 2.22 Demonstration of sintering; a) particles in contact, b) neck formation by inter-particle diffusion, and c) coalescence of particles (German, 2010)

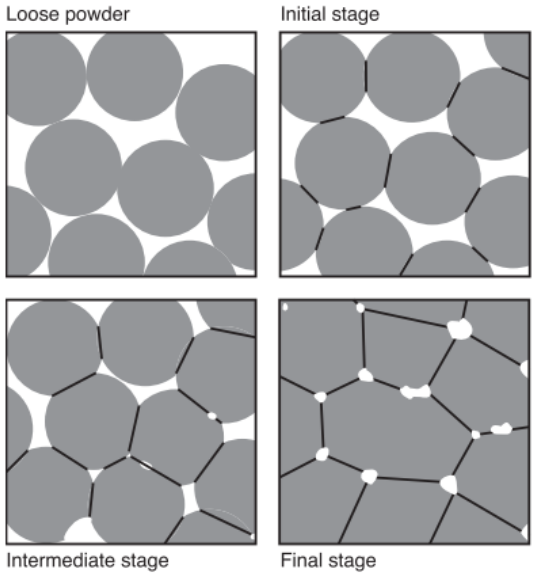

Figure 2.23 Illustration of sintering process (German, 2010)

Here, the theoretical background and previous literature (Table 2.1) on solar cells were summarized in detail. Based on the information given, a study was conducted as a unique and original thesis covering the production of sol-gel derived NiO_x and $Li_{0.05}A_aNi_{(0.95-a)}O_x$ (A: Cu, Mg; a: 0.05, 0.10, 0.15) powders to form sputtering targets and deposition of NiO_x thin films as HTMs with intended stoichiometries together with the other important layers (ETM, PSK, contacts) in their commercial forms to construct novel PSCs for the first time.

CHAPTER THREE
EXPERIMENTAL

3.1 The Objective of The Study

This study aims to produce and characterize NiO_x and $Li_{0.05}A_aNi_{(0.95-a)}O_x$ (A: Cu, Mg; a: 0.05, 0.10, 0.15) thin films from the target materials that have the same stoichiometry by RF-magnetron sputtering system to use as HTM layer in perovskite solar cells. For this purpose, powders used in the target materials were produced by the sol-gel process. Pre-forming of target materials using the powders and PVA-water mixture was carried out through cold isostatic pressing. The pre-formed bulk material, the green body, was then sintered to obtain dense targets to be used in the sputtering system. NiO_x and $Li_{0.05}A_aNi_{(0.95-a)}O_x$ (A: Cu, Mg; a: 0.05, 0.10, 0.15) thin films to act as hole transport layers were deposited on ITO/glass substrates from the target materials by the RF-magnetron sputter system. After depositing hole transport layers with varying stoichiometries on the ITO/glass substrates, other critical layers of a perovskite solar cell are deposited sequentially. Since the main focus of the study is to investigate effects of doping and structural modification in NiO_x structure, other layers (perovskite layer, electron transport layer, buffer layer, and back contact) were deposited from commercial and standard routes of literature.

3.2 Materials

From the production of the powders to the fabrication of solar cells, many different substances and materials listed in Table 3.1 were used as-purchased without any treatment.

3.3 Methods

The experimental part of the study consists of two main parts as the production & characterization of target materials and PSCs as illustrated in Figure 3.1 The production of target materials is based on the production and shaping of powders. The

fabrication of solar cells includes the deposition of HTMs and the other layers. Nomenclatures and prefixes for samples of different stoichiometry are given in Table 3.2.

Table 3.1 List of substance/materials

Process	Substance/Material	Purity, Supplier
Production of Powders	Nickel nitrate hexahydrate ($Ni(NO_3)_2.6H_2O$)	≥ 97%, Sigma Aldrich
	Lithium nitrate ($LiNO_3$)	≥ 98%, Sigma Aldrich
	Magnesium acetate tetrahydrate $(CH_3COO)_2Mg{\cdot}4H_2O$	≥ 98%, Sigma Aldrich
	Copper nitrate trihydrate ($Cu(NO_3)_2.3H_2O$)	≥ 98%, Sigma Aldrich
	Methanol (CH_3OH)	≥ 99.8%, Sigma Aldrich
	Acetic acid (CH_3COOH)	≥ 99.7%, Sigma Aldrich
Production of Targets	Polyvinyl alcohol (PVA) $((C_2H_4O)_x)$	≥ 99%, Sigma Aldrich
Deposition of HTM Layer	Argon gas	99.999%, Linde
	Oxygen gas	99.999%, Linde
	ITO coated glass substrate (LT-G001)	9 - 15 Ω/sq, Lumtec
Deposition of Perovskite Layer	Methylammonium iodide MAI (CH_3NH_3I)	> 99.5%, Lumtec
	Lead(II) iodide (PbI_2)	99.999%, Lumtec
	N,N-Dimethylformamide (DMF)	99.8%, Sigma Aldrich
	Dimethyl sulfoxide (DMSO)	≥ 99.9%, Sigma Aldrich
	γ-Butyrolactone (GBL)	≥ 99%, Sigma Aldrich
	Chlorobenzene (CBZ)	≥ 99.5%, Sigma Aldrich
Deposition of ETM Layer	(6,6)-Phenyl C61 butyric acid methyl ester (PCBM)	> 99.5%, Lumtec
Deposition of Buffer Layer	Bathocuproine (BCP)	99.99%, Sigma Aldrich
Deposition of Contact Layer	Silver pellet	99.99%
	Gold pellet	99.99%
	Tungsten Boat (0.3 CC)	RD-Mathis

The types of equipment used during the production are as follows;

- *Production of powders:*
  - Magnetic Stirrer (Wisd Wise Stir MSH-20D)

- Drying oven (Binder ED53)
- Oven (Protherm PLF 130/6)

- *Production of target materials:*
  - Hydraulic press (Specac, Atlas)
  - CIP (AIP, CP360)
- *Deposition of HTM thin film:*
  - RF-Magnetron Sputter (Nanovak NVTH-350)
- *Deposition of ETM and buffer layer:*
  - Glove Box System (MBraun M200)
  - Magnetic Stirrer (Wisd Wise Stir MSH-20D)
- *Deposition of contact layer:*
  - Glove Box System (MBraun M200)
  - Thermal Evaporator (MBraun)

Table 3.2 Nomenclatures and prefixes for samples of different stoichiometry

Prefix	Sample	Li	$Mg_{(a)}$ / $Cu_{(a)}$	$Ni_{(0,95-a)}O_x$
P, T, F, S-	N	0.00	0.00	1.00
P, T, F, S-	NL	0.05	0.00 (Mg)	0.95
P-	NLM5	0.05	0.05 (Mg)	0.90
P, T, F, S-	NLM10	0.05	0.10 (Mg)	0.85
P, T, F, S-	NLM15	0.05	0.15 (Mg)	0.80
P-	NLM30	0.05	0.30 (Mg)	0.65
P, T, F, S-	NLC5	0.05	0.05 (Cu)	0.90
P-	NLC10	0.05	0.10 (Cu)	0.85
P, T, F, S-	NLC15	0.05	0.15 (Cu)	0.80
P-	NLC30	0.05	0.30 (Cu)	0.65

P: powder, T: target material, F: thin film, S: solar cell

3.3.1 Production of Target Materials

3.3.1.1 Production of NiO_x-Based Powders

$Ni(NO_3)_2.6H_2O$, CH_3OH, and CH_3COOH were used as NiO precursor, solvent, and catalyst, namely chelating agent to produce NiO-based powders, respectively. For the single or co-doped samples, the number of additives was added respective to mole

ratios in the given stoichiometries. The stoichiometries and compositions of the solutions are given in Table 3.3. A sufficient amount of acetic acid was added to keep the pH ≈ 2. The mixtures were stirred minimum of 60 min to obtain transparent solutions. Then, the solution was held at 80 - 100 °C for gelation. Grinding was performed to the dried gels in a mortar and transferred to the oven for drying at 275 °C for 2 h to eliminate hydroxyl and organic groups (Ahmed, Pang, Olea, & Hodgson, 2012). Pristine NiO_x samples were heat-treated at 300 °C, 500 °C, and 650 °C to determine optimum annealing temperature.

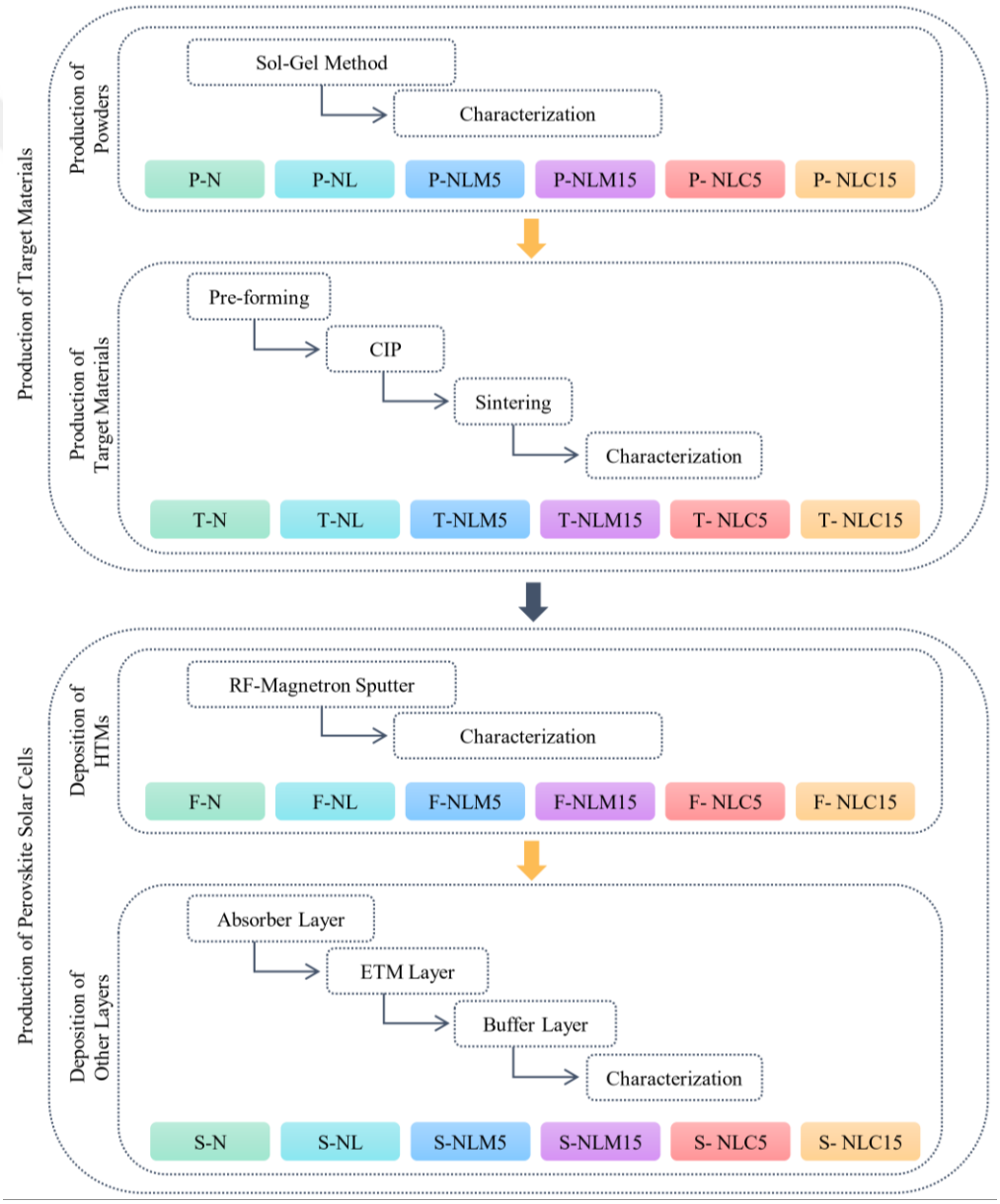

Figure 3.1 Flowchart of the manufacturing process

Table 3.3 Amount of precursor used in samples with different stoichiometries

Substance	**P-N**	**P-NL**	**P-NLM5**	**P-NLM15**	**P-NLC5**	**P-NLM15**
$Ni(NO_3)_2.6H_2O$	179.88 g	170.88 g	161.88 g	143.88 g	161.88 g	143.88 g
CH_3OH	400 ml	400 ml	400 ml	400 ml	400 ml	400 ml
$LiNO_3$	-	2.12 g	2.12 g	2.12 g	2.12 g	2.12 g
$CH_3COO)_2Mg{\cdot}4H_2O$	-	-	6.56 g	19.68 g	-	-
$Cu(NO_3)_2.3H_2O$	-	-	-	-	7.4 g	22.2 g

3.3.1.2 Production of Target Materials

Each sample was manufactured at least more than 40 ± 1 g in powder with the same approach as explained previously to produce pristine or doped target materials. The green body was obtained by mixing powders with 3 wt%. PVA binder -water solution by hand. The mixture was pressed under 0.1 MPa for 5 min in a 2-inch (5.08 cm) diameter mold at hydraulic press after being dried at 150 °C for 1 hour in the oven. The pre-formed sample in a vacuumed bag was hydrostatically pressed under 250 MPa for 30 min at cold isostatic press (CIP – AIP, C360). The sample was then sintered at 1300 °C for 12 hours to reduce porosities and impurities (Protherm, PLF 130/6). Target materials with ~ 45 mm in diameter were obtained after all processes. The Cu backplate is bonded to the targets with adhesive carbon tape to increase thermal conductivity, which can dissipate the heat generated during sputtering.

3.3.2 Production of Perovskite Solar Cells

3.3.2.1 Deposition of HTM Layers

To fabricate p-i-n type PSCs, the first operation is to deposit the HTM layer onto the TCOs. For this purpose, NiO-based thin films were deposited on ITO/glass substrates using T-N, T-NL, T-NLM5, T-NLM15, T-NLC5, and T-NLC15 targets by RF-magnetron sputtering system with the parameters given in Table 3.4. ITO/glass samples were cleaned in ethanol and DI water for 10 min, respectively. Target to sample distance was fixed to 10 cm. The chamber was evacuated to $4.5 – 5 \times 10^{-6}$ Torr as the initial vacuum. 45 W RF power was used for the sputtering process with Ar/O_2

gas mixtures (15/10 SCCM) at 4 x 10^{-2} Torr system vacuum. Targets were sputtered with close-shutter mode to remove contamination on their surfaces for 15 min. As a result, thin films were deposited on ITO/glass substrate for 30 mins. then they were annealed at 450 °C for 2 h.

Table 3.4 The sputtering parameters

	T-N	T-NL	T-NLM5	T-NLM15	T-NLC5	T-NLC15
Target Diameters	45 mm	46.1 mm	43.1 mm	44.3 mm	43.7 mm	42.3 mm
RF Power	45 W					
Initial Vacuum	3 - 4.5×10^{-6} Torr					
Deposition Vacuum	4×10^{-2} Torr					
Sputtering Time	30 min					
Gas Flow Ratio	40% O_2 / 60% Ar [O_2 / (Ar + O_2)] : 40%					
Substrate	ITO/Glass					
Distance	10 cm					
Temperature	Room Temperature					

3.3.2.2 Production of the perovskite layer

Absorber, ETM, and buffer layers are spin-coated in the glove box system as shown in Figure 3.2. Precursor solution of perovskite was obtained by mixing of 553 mg PbI_2 and 190 mg MAI in 1 ml of GBL:DMF:DMSO mixture with 4:3:3 volume ratio to obtain 1.2 M concentration at 65 ºC for 12 hours and after filtering with 0.45 µm PVDF. All substrates were spin-coated for 1 s at 500 rpm, 1 s at 1500 rpm, and 40 s at 4000 rpm with 50 µm solution. Surface washing was performed with 100 µm of chlorobenzene at 27th seconds to remove volatile solutions from the surface fast. The coated samples were annealed at 100 ºC for 10 min. One side was cleaned with acetone for electrical measurement and device architecture.

3.3.2.3 Production of Electron Transport Layer

For the ETM layer, a homogenous solution was prepared by dissolving 20 mg of PCBM in 1 ml of chlorobenzene and stirring for 1 day at 45 °C. The solution was spin

coated for 15 s at 1500 rpm, and 20 s at 2500 rpm on ITO/HTM/PSK (HTM: F-N, F-NL, F-NLM5, F-NLM15, F-NLC5, and F-NLC15).

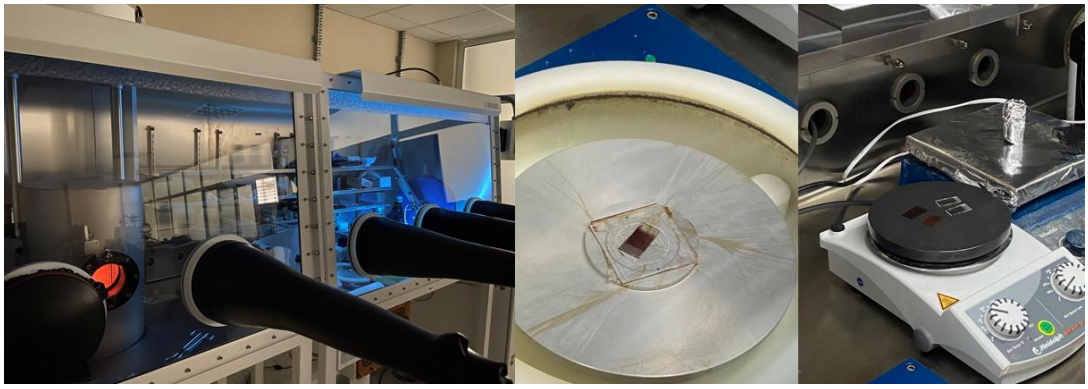

Figure 3.2 MBraun M200B glove box system (Personal archive, 2021)

3.3.2.4 Production of Buffer Layer

For the buffer layer, which acts as an exciton-blocking barrier with reducing non-radiative recombination of excitons at the PCBM/contact interface, a solution was prepared by dissolving 0.5 mg of BCP in 1 ml of ethanol. The solution was spin-coated for 40 s at 4000 rpm on ITO/HTM/PSK/ETM (HTM: F-N, F-NL, F-NLM5, F-NLM15, F-NLC5, and F-NLC15) devices.

3.3.2.5 Deposition of Contact Layer

Deposition of contact layers was carried out onto the BCP layer using Ag or Au (99.99%) pellets in a tungsten boat by the thermal evaporator. A mask with fixed windows was used to obtain defined cell sizes and measure electrical properties. The deposition rate was 3.5 Å/s and the process was terminated when a 150 nm coating was obtained. The thermal evaporator system and the mask are shown in Figure 3.3.

Photovoltaic cells were fabricated with two different approaches using the same parameters and coded with S1 and S2 prefixes. All HTMs onto the ITO layer were fabricated in two sets. The PSCs fabricated in the glove box and characterized in

ambient conditions were coded as S1. The other PCS fabricated in ambient conditions and characterized in the glove box were coded as S2.

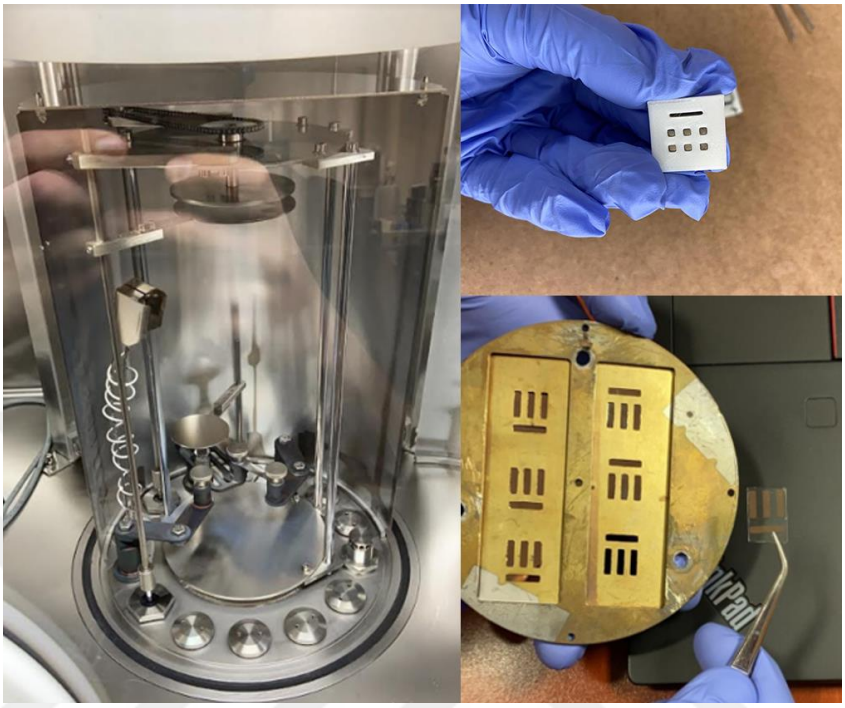

Figure 3.3 The thermal evaporator system and masks (Personal archive, 2021)

3.4 Characterization

3.4.1 Fourier transform infrared spectroscopy

FT-IR is a useful instrument to determine chemical bonds of molecules in organic or inorganic compounds by interpreting infrared absorption spectrum. Because each material is made up of a particular set of atoms, no two different compounds will ever have the same infrared spectrum. Hereby, IR may be used to do qualitative investigation on a wide range of materials. When molecules are excited with infrared spectrum, such motions of atoms occur at specific frequencies in their bonds, depending on the element and the type of bonds in their structure.

All powders with varying annealing temperatures were analyzed with a Perkin Elmer Spectrum BX (DEU, EMUM) instrument with an ATR accessory at a resolution

of 4 cm^{-1} in the spectrum range of 4000 to 650 cm^{-1}, and results are obtained as % transmittance as a function of wavelength and % absorption as a function of wavenumber curves.

3.4.2 X-Ray Diffractometer

XRD is the critical method to identify crystalline structure and structural phases of investigated materials. XRD method is based on Bragg's Law ($n\lambda = 2d\sin\theta$). The sample is exposed to incident X-ray beams and scattered beams are detected with a detector that is in a relative motion with x-ray source in such a way that the angle between the sample and itself is theta, which gives a diffraction pattern. By evaluating at the peak width and intensity of peaks in the pattern, information about the crystallization of the sample can be gathered and interpreted.

Powders, targets materials and thin films were characterized with Thermo Scientific, ARL X'TRA (DEU, EMUM) system that used radiation of Cu-K_α (1.5406 Å) set up voltage of 45 kV and current of 44 mA. Diffraction angles (2θ) were determined.

3.4.3 X-Ray Photoelectron Spectroscopy

XPS is used to identify to elemental composition, electronic state and chemical state of the elements existed in solid samples. Samples are exposed to incident x-ray beams in the ultra-high vacuum condition, and system are detected and analyzed the kinetic energies and numbers of photogenerated electrons escaped from 1-10 nm depth of surfaces. All elements except hydrogen and helium could be analyzed with XPS instrument due to having small diameter of orbitals.

Powders, target materials, and thin films were characterized for elemental composition and surface chemistry by Thermo Scientific K-Alpha (DEU, EMUM) with adjusting beam size of 400 nm and using monochromatic Al-K_α (1486.7 eV) as X-ray source at $5x10^{-10}$ mbar during spectral data acquirement. The survey spectra

were obtained with scanning 20 repetitions of each spots between -10 and 1350 eV with a transition energy of 150 eV and a scanning step of 1 eV. Core level spectra were obtained with the pass energy of 30 eV and 15 numbers of scans.

3.4.4 Scanning Electron Microscope

SEM is one of the most used analytic methods to investigate surface morphologies of solid samples such as powders, bulk materials or thin films. Surface of specimen are scanned with highly energetics electrons that oriented with the help of magnetic lenses in high vacuum environment. Backscattered electrons and secondary electrons are formed as a result of interaction between incident electrons and sample. Images which giving compositional and topographical information and a depth of field of topography are generated with the help of collecting of backscattered and secondary electrons at detector.

SEM images were obtained for powders, target materials, and thin films by Carl Zeiss, 300 VP (IKCU) with SE mode at 5 kV accelerating voltage at different magnifications of images.

3.4.5 Density

The Archimedes Method is used to calculate the density of materials, especially for ceramic bulk materials, based on calculating the pore volumes from the weight of the water required to fill the pores. First, after the sample is thoroughly dried in the oven, it is weighed on a precision scale (W_K) . The samples are then transferred to boiling water and left there for 4 hours while the boiling continues, then left to cool to room temperature. Its weight in water is measured with the help of a special apparatus, called (W_A). The sample is then haul out from the water, the water on its surface is wiped off and quickly weighed on the presicion scale, called (W_D). With these data and density of water (ρ_{water}), the bulk density and apparent solid density could be calculated.

$$Bulk\ Density = \frac{W_K}{W_D - W_A}\ x\ \rho_{water} \tag{3.1}$$

$$Apparent\ Solid\ Density = \frac{W_K}{W_K - W_A}\ x\ \rho_{water} \quad (3.2)$$

3.4.6 Hall Effect Measurement

Hall measurement system was used to determine hole mobility of thin films in ambient conditions using Ecopia HMS-3000 equipment (DEU, EMUM) working by Van der Pauw's method (Pauw, 1958). Samples should be square and contacted from four contacts to the sample holder in which two of them use for applying voltage, while the others utilize for measuring current. The electrons were affected by the magnetic field (0.55 T) applied perpendicular to the sample. With this effect called Lorentz force, the electrons changed direction and created a potential difference called the Hall voltage. Mobility was calculated by the obtained data (Chwang, Smith, & Crowell, 1974).

3.4.7 UV-Vis Spectrophotometer

The transmittance properties are crucial for HTM films that should allow incident light to arrive absorber layer in p-i-n architecture. Therefore, UV-Vis Spectrophotometer was utilized to characterize the transmittance properties. The system compares the incoming light intensity before passing through sample to the light intensity after passing through sample, and the ratio between these numbers gives the percentage of transmittance for a specific wavelength.

HTM films deposited on ITO substrate were measured by JASCO V-530 (DEU, MME) with wavelengths of 200-800 nm. In addition, only ITO substrate was measured for comparison. Bandgap calculation was carried out by Spectra Manager Application provided by JASCO.

3.4.8 Photoluminescence

PL is a tool to identify optoelectronic properties of materials, especially semiconductors with using light sources and detectors. The photon energy directed to

the sample causing photoexcitation which causes electrons to move excited states by by giving excess energy to the sample. When electrons are get back to equilibrium state from excited state, this excess energy is expelled from the sample as light emission or luminescence which specifically called photoluminescence which is related energy differences between excited state and equilibrium state.

Steady state florescence and decay time measurements of powders and thin films were carried out by Edinburg Instruments of FLSP920 (DEU, EMUM) with using 15 W xenon lamp and a micro second flash lamp, respectively.

3.4.9 Photovoltaic Characterization

Current-Voltage measurements were carried out under AM1.5G solar illumination (100 mW/cm^2) using Optosense LSS solar simulator in ambient condition and ABET solar simulator in the glove box for S1 and S2 coded PCSs, respectively. For both, Keithley 2400 source-meter were utilized and V_{OC}, I_{SC}, J_{SC}, FF, and PCE (η %) were calculated for all solar cells.

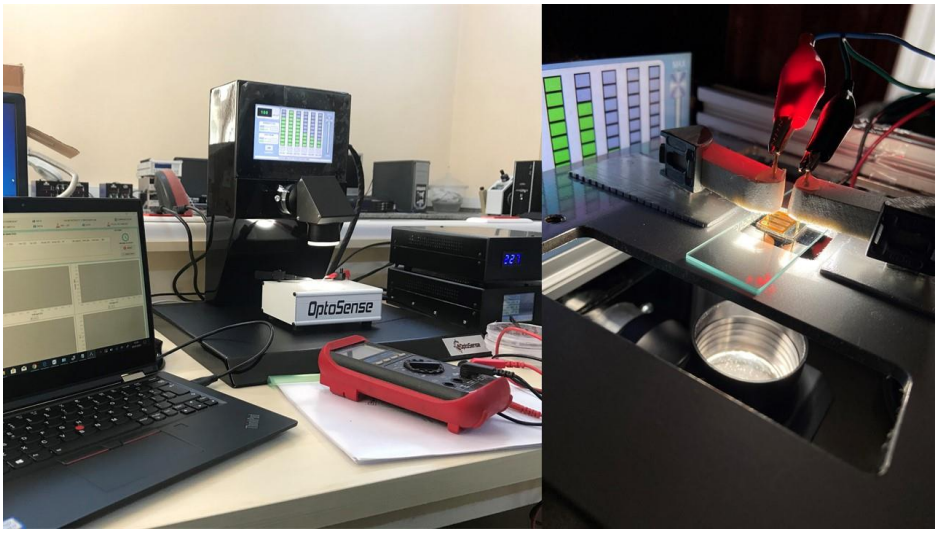

Figure 3.4 Solar simulator equipment and produced solar cell (Personal archieve, 2021)

CHAPTER FOUR
RESULTS AND DISCUSSION

The focus of the study is to fabricate perovskite solar cells with inorganic NiO_x-based HTM layers obtained by sputtering targets with different stoichiometry. In this context, the results are evaluated according to previously mentioned sequential production steps as powder, target materials, thin films, and perovskite solar cells.

4.1 Characterization of Powders

4.1.1 Spectroscopic Analysis

Functional groups of powders produced by sol-gel method were determined by FTIR analysis and results of P-N with different heat-treatment temperatures (275 °C, 350 °C, 500 °C, and 650 °C) was given in Figure 4.1. FTIR results show the presence of nitrate, carbonate groups, and crystal water in the structure. Peak O-H bonds between 3500 and 3750 cm^{-1} are attributed to carbonate (C=O) groups of about 1600 cm^{-1}. Absorption of 1100 - 1450 cm^{-1} corresponds to the presence of nitrate groups, approximately 2900 cm^{-1} corresponds to the C-H bond. Peaks between about 1000-750 cm^{-1}; indicate hydrogen-bonded π bond carbons (=CH). The absorption zone around 660 cm^{-1} is related to the Ni-O-H vibration bond. The absorption zone between 500 and 600 cm^{-1} also shows that NiO corresponds to the peaks of the metal-oxygen vibration modes. The peak of the O-H tensile bond in the range of 3500 - 3750 cm^{-1} after the drying process at 275 °C is coherent with the mass loss from TGA. The density of N-O (1525 cm^{-1}), C-O (1290 cm^{-1}), and C-H (973 cm^{-1}) bonds decreased with the increasing temperature. In addition, Ni-O bonds at 400-600 cm^{-1} were clearly observed (Thongtem & Thongtem, 2005).

4.1.2 Phase Analysis

The crystal phase structure and impurities in the structure of powders produced by the sol-gel method were determined using XRD. In Figure 4.2, XRD patterns of P-N

samples annealed after drying (275 °C) at different temperatures (350 °C, 500 °C, 650 °C) are given. Characteristic peaks at 37.48°, 43.47°, 63.12°, 75.58°, and 79.53° are related to (111), (200), (220), (311), and (222) crystal planes of cubic NiO_x according to JCPDS card no. #47-1049, respectively (H. Yan et al., 2014). Although the related peaks are observed for the samples annealed at 275 °C, it is understood that there are various impurities in the structure, as also known from FTIR analysis, due to extra peaks especially in the range of 20 - 35°, since the phase conversion did not take place. After 350 °C, phase transformation was not observed, crystallinity increase was observed by the intensity of the peaks with increasing temperature (Alagiri, Ponnusamy, & Muthamizhchelvan, 2012; Sheena, Priyanka, Sabu, Sabu, & Varghese, 2014; Teoh & Li, 2012).

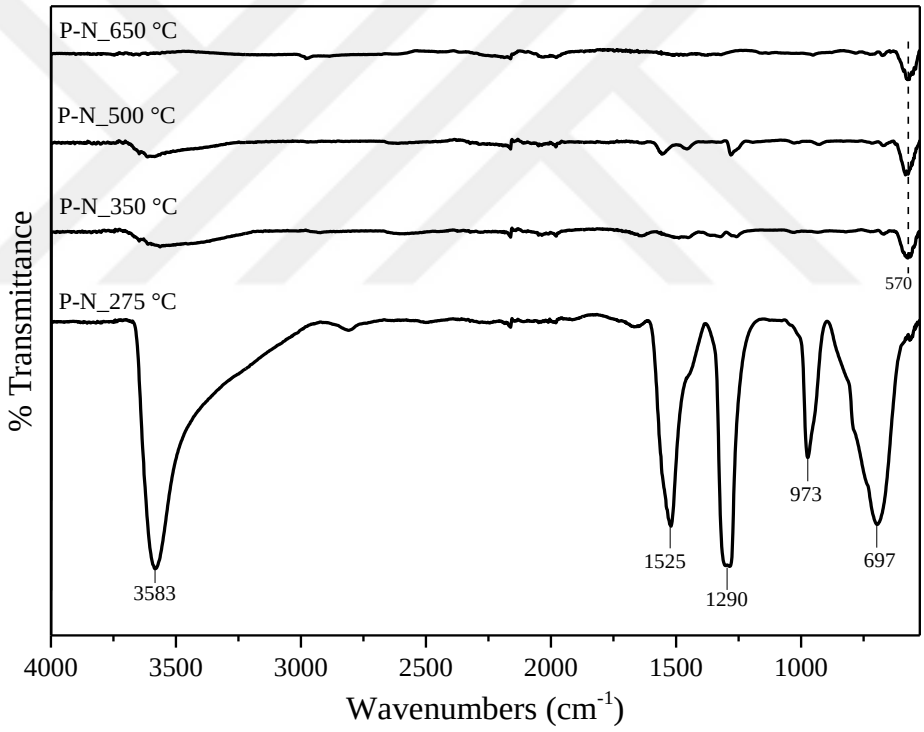

Figure 4.1 FTIR analysis of P-N based powders

Comparative XRD patterns of pristine and doped NiOx powders (P-N, P-NL, P-NLM5, P-NLM10, P-NLM15, P-NLM30, P-NLC5, P-NLC10, P-NLC15, and P-NLC30) are given in Figure 4.3 and Figure 4.4 to investigate the effect of additives on the structure. It can be thought that the Li^{1+}, $Mg^{2+,}$ and Cu^{2+} ions take place as additives in the structure due to no other phase formation except NLC30. The NLC30 sample in

Figure 4.5 shows the crystal planes of the cubic NiO phase, as well as the extra 35.8° and 39.1° peaks of the CuO compound corresponding to the literature JCPDS card no #80-1917, and these peaks belong to the (002)(-111) and (111)(200) crystal planes, respectively (Niveditha, Fatima, & Sindhu, 2016).

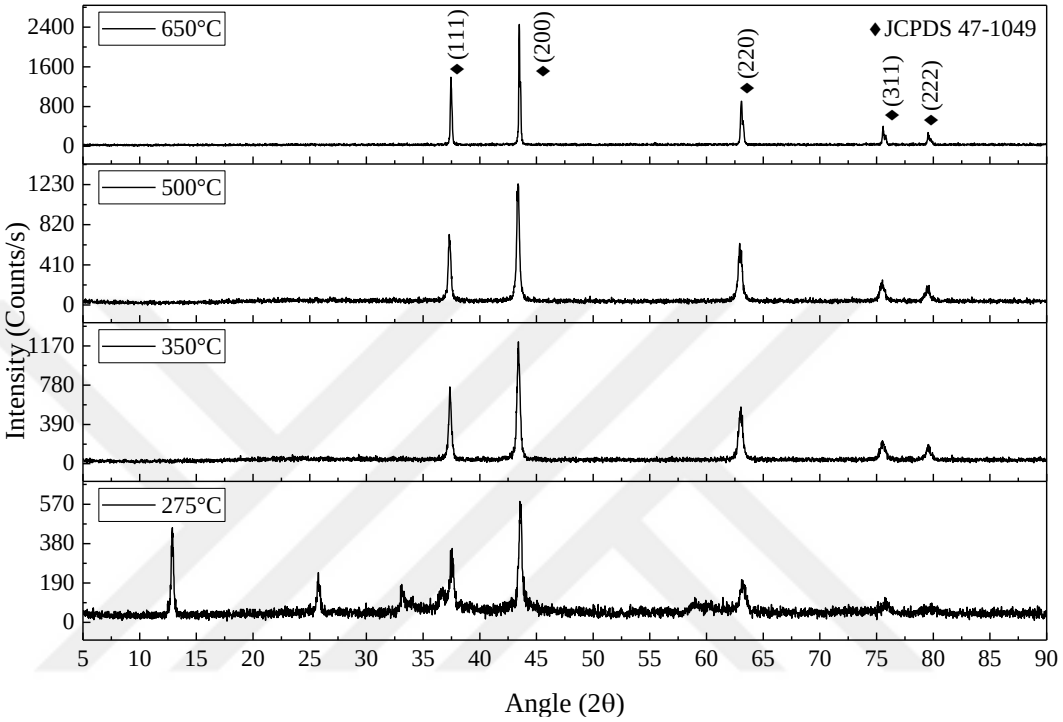

Figure 4.2 XRD pattern of P-N sample annealed at different temperatures

The additives incorporated in the structure should be investigated due to their effect on the distortion of the structure, although the ionic radii of Li^{1+} (76 pm), Mg^{2+} (72 pm), and Cu^{2+} (73 pm) are close to the radius of the Ni^{2+} (69 pm) ion (Shannon, 1976). In order to show the effect of additives on the structural change, the range of 43 - 44° has been examined particularly. The Debye – Scherrer and Bragg Equation are utilized to calculate crystallite sizes, d-spacing, and lattice parameters:

$$D = \frac{K\lambda}{\beta cos\theta} \tag{4.1}$$

$$n\lambda = 2dsin\theta \tag{4.2}$$

$$d_{hkl} = \frac{a}{\sqrt{h^2+k^2+l^2}} \tag{4.3}$$

where K = 0.94 (Scherrer constant), λ = 1.5406 Å (wavelength of X-ray for Cu $K_{\alpha 1}$ radiation), θ is diffraction angle of the peak, β is full width at half maximum (FWHM) of the peak, n = 1 (order of reflection), d_{hkl} is interplanar spacing, a is lattice parameter, and h, k, l are Miller indices. Peak positions, FWHMs, crystallite sizes, d-spacing, and lattice parameters for all powders are given in Table 4.1.

Table 4.1 Peak positions, FWHMs, crystallite sizes, d-spacing, and lattice parameters for all powders

Sample	(200) Peak Position 2θ (°)	FWHM β(°)	Crystallite Size (nm)	d_{200} (nm)	a (Å)
P-N (275°C)	43.5403	0.3023	29.5546	2.0769	4.1538
P-N (350°C)	43.4002	0.2736	32.6390	2.0833	4.1665
P-N (500°C)	43.3794	0.2481	35.9910	2.0842	4.1684
P-N (650°C)	43.4798	0.1181	75.6649	2.0796	4.1593
P-NL	43.4798	0.1844	48.4408	2.0796	4.1592
P-NLC5	43.6999	0.2044	43.7346	2.0697	4.1393
P-NLC10	43.6796	0.2249	39.7453	2.0706	4.1412
P-NLC15	43.6547	0.2472	36.1567	2.0697	4.1434
P-NLC30	43.6199	0.3749	23.8380	2.0733	4.1465
P-NLM5	43.4195	0.2211	40.3917	2.0824	4.1648
P-NLM10	43.3799	0.2133	41.8630	2.0842	4.1684
P-NLM15	43.4202	0.2104	42.4460	2.0823	4.1647
P-NLM30	43.4598	0.2357	37.8951	2.0805	4.1611

For P-N, with increasing annealing temperature, the crystallite size increases to 75.66 nm with the intensification of the peaks and the contraction of FWHM. The calculated lattice parameter (4.1593 Å) which is lower than the value (4.1771 Å) of JCPDS card no #47-1049 and leading structure to become non-stoichiometric can be attributed to differences in the ionic radius of Ni^{3+} (0.56 Å) and Ni^{2+} (0.69 Å) (Dubey & Kaurav, 2020).

Figure 4.5 represents the changes in crystallite sizes and lattice parameters with different additives ratios. The addition of Li^{+} decreased the crystallite size of P-NL sample to 48.44 nm. The lattice parameter (4.1592 Å) was calculated for P-NL. Li et al. observed a slight decrease in the lattice parameter with the addition of Li. Their findings pointed out that lattice parameter was decreased slightly because Li^{+} (0.76 Å) occupied Ni^{2+} sites in the crystal structure causes creating excess vacancies and converting Ni^{2+} (0.69 Å) to Ni^{3+} (0.56 Å) for charge neutralization(Y. Li, Li, Wang, Guo, & Li, 2016).

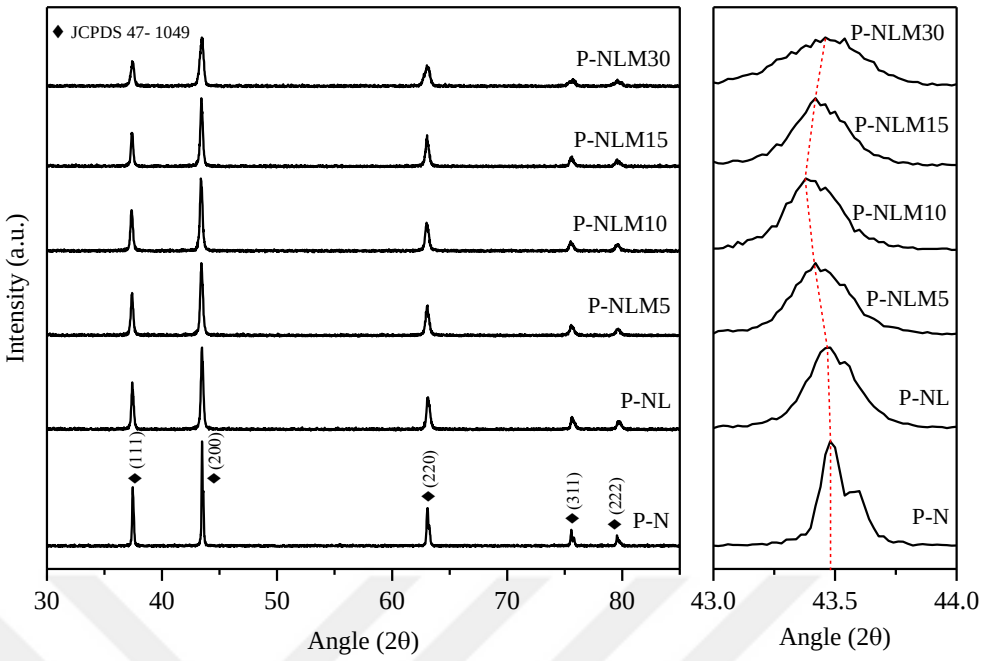

Figure 4.3 XRD patterns of P-N, P-NL, and P-NLM(5, 10, 15, 30)

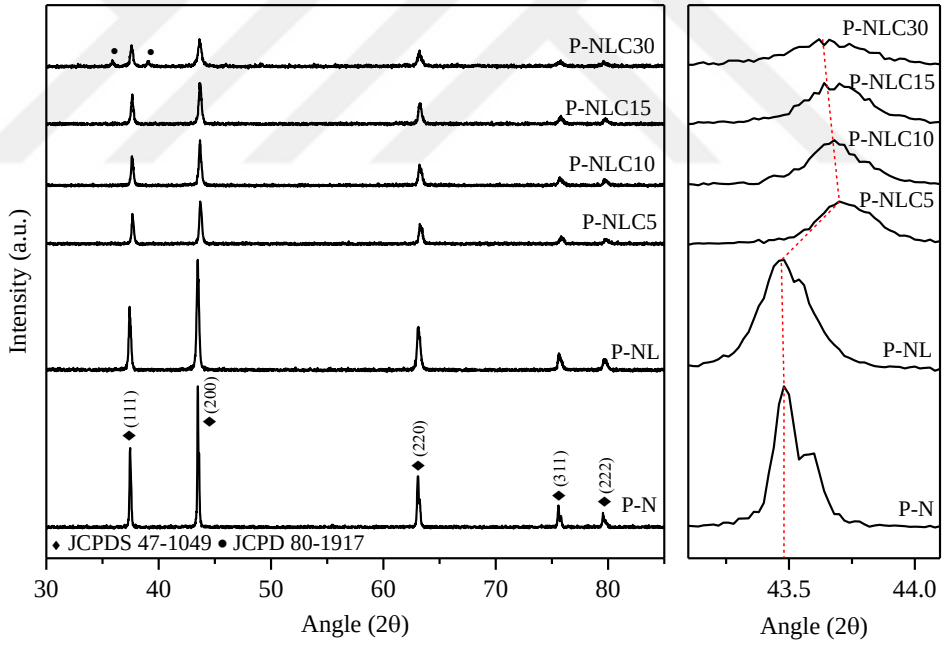

Figure 4.4 XRD patterns of P-N, P-NL, and P-NLC(5, 10, 15, 30)

By magnesium addition, both shifts and broadening of the peaks were observed. The crystallite size decreased with increasing additive ratios. Mg^{2+} (72 pm), which entered the structure up to P-NLM10, expanded the cubic cell and increased the lattice parameter (Panigrahi, Sathe, Babu, Mitra, & Mallick, 2020). The lattice parameter

decreased gradually in the P-NLM15 and P-NLM30 samples. The reason for this decrease is thought to be due to the precipitation of MgO instead of incorporation. . It is thought that the reason why the secondary MgO peaks do not appear in the phase analysis is the exact overlap of the MgO (200) peaks with the NiO (200) peaks (Ben Amor, Boukhachem, Boubaker, & Amlouk, 2014; Mastuli et al., 2014; Matsubara, Huang, Iwamoto, & Pan, 2014).

Like Magnesium, both shifts and broadenings were observed in the peaks with copper doping. A decrease in crystallite size was observed with increasing additive ratios. Lattice parameter decreased after Cu incorporation into structure as seen on P-NLC5, then it increased with increasing additive ratios. The decrease in lattice parameter may be due to the substitution of Cu^{2+} (73 pm) with Ni^{2+}, forcing Ni^{2+} to convert into Ni^{3+} and therefore the formation of vacancy in the structure. A similar situation is also described for Li doping (Y. Li et al., 2016). The increase in lattice parameter with increasing additive ratio could be due to the formation of CuO precipitates (D. Xu et al., 2015). Due to the fact that, precipitated CuO phases were seen in the patterns of P-NLC30 sample at 35.8° and 39.1° (Niveditha et al., 2016).

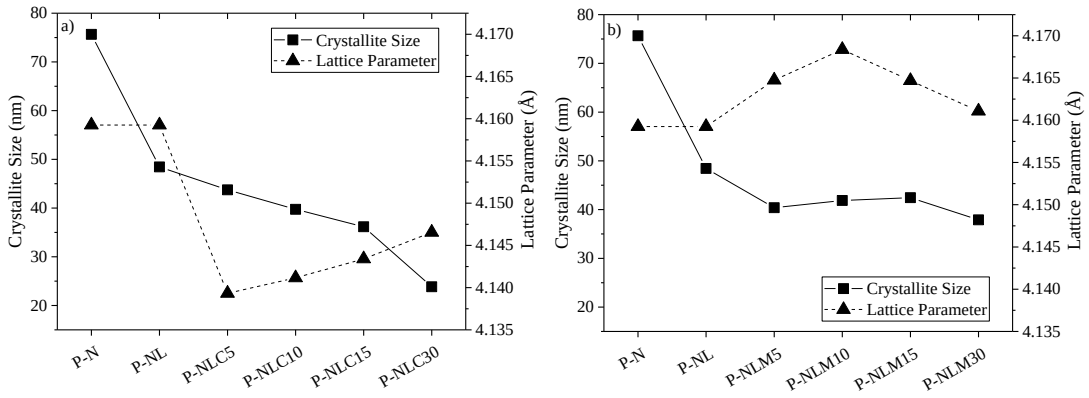

Figure 4.5 Crystallite sizes and lattice parameters of a) P-N, P-NL, P-NLM(5, 10, 15, 30), and b) P-N, P-NL, P-NLC(5, 10, 15, 30)

4.1.3 Elemental Analysis

XPS analysis is carried out to perform elemental analysis. As shown in survey scans (Figure 4.6), the presence of Ni, O, and C elements was observed for all samples. Li

and Mg peaks were detected in P-NLM samples while Li and Cu peaks were recorded in P-NLC samples. It is important to note that the C peaks came from the carbon tape used to fix the powders to the holder (Moulder, Stickle, Sobol, & Bomben, 1992).

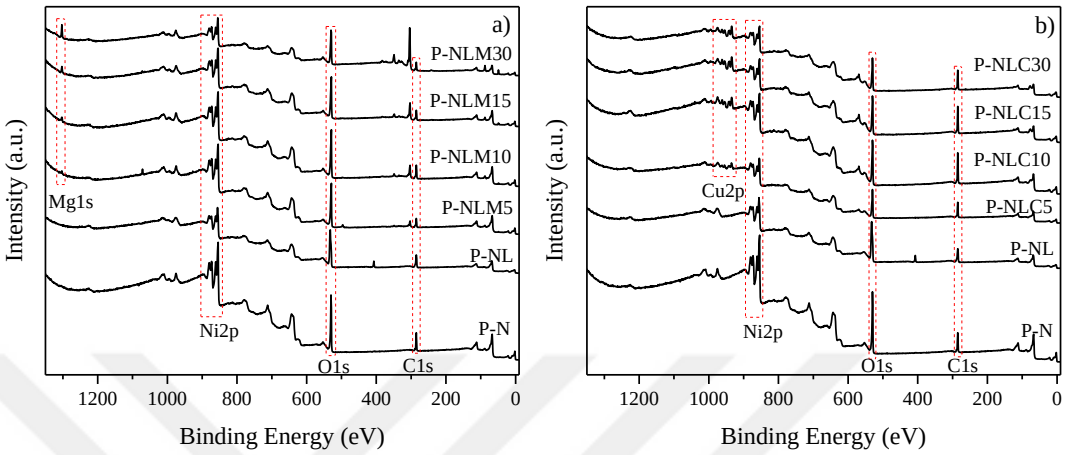

Figure 4.6 XPS survey scans for a) P-N, P-NL, P-NLM(5, 10, 15, 30), and b) P-N, P-NL, P-NLC(5, 10, 15, 30)

Core level scans for P-NLM and P-NLC samples are shown in Figure 4.7 and Figure 4.8, respectively. The peak positions and weight ratios of all powders are listed in Table 4.2. The characteristic quadruple peaks of the NiO phase are observed in the 850 - 890 eV binding energy range. Peaks around 854 eV, 861 eV, 872 eV, and 879 eV are associated with $Ni2p_{3/2}$, $Ni2p_{3/2}$ scatterings, $Ni2p_{1/2}$, and $Ni2p_{1/2}$ scatterings, respectively which are related to octahedral binding of NiO (J. Chen, Wu, Tan, & Chen, 2018; W. Huang et al., 2017; H. Yan et al., 2014). The two deconvoluted peaks around 529.38 eV and 531.18 eV are associated with the Ni-O octahedral binding of NiO (L. Xu et al., 2019). Due to the lower binding energy of Li, its fewer amounts are difficult to be detected, but the recorded Li1s peak seen at around 55 eV shows the existence of Li in the structure (J. Chen et al., 2018). Mg1s peak around 1302 eV revealed the presence of Mg^{2+} (Dong et al., 2018). Peaks around 934 eV, 941 eV, 954.08 eV, and 961 eV are associated with the $Cu2p_{3/2}$, $Cu2p_{3/2}$, $Cu2p_{1/2}$, and $Cu2p_{1/2}$, respectively (He et al., 2017).

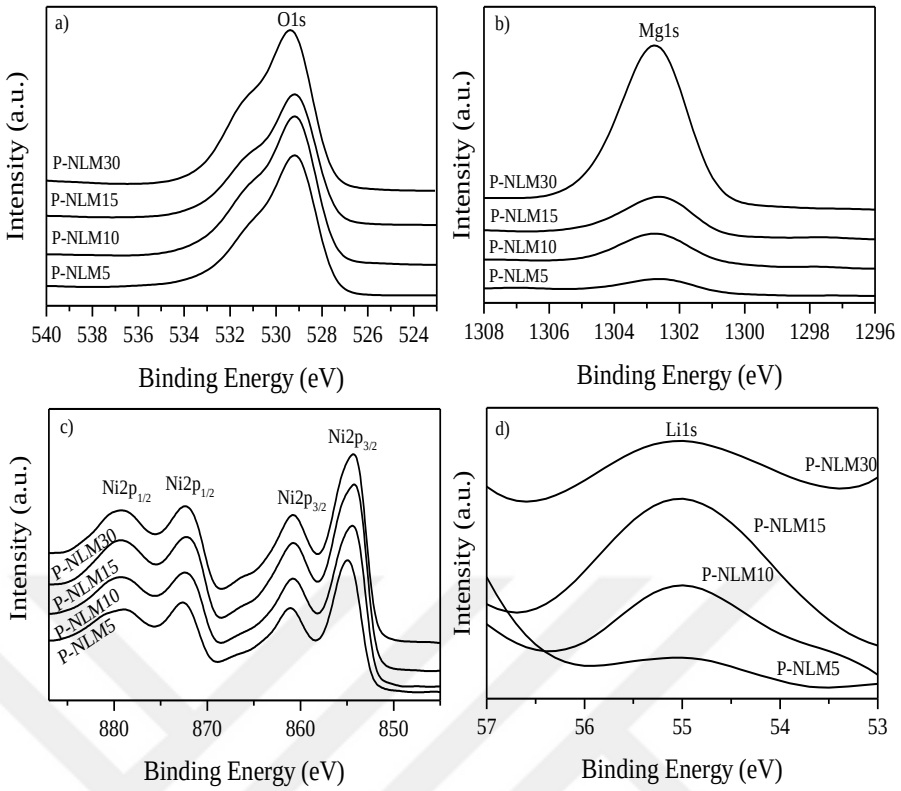

Figure 4.7 XPS core level spectra of a) O1s, b) Mg1s, c) Ni2p, d)Li1s peaks for P-NLM(5, 10, 15, 30)

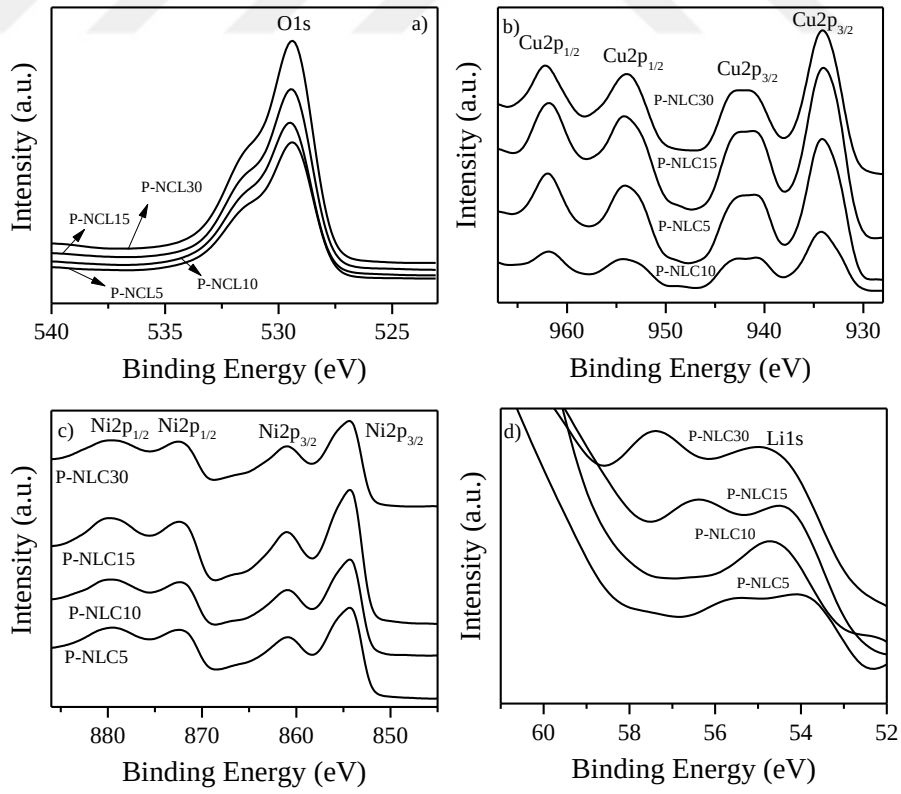

Figure 4.8 XPS core level spectra of a) O1s, b) Cu2p, c) Ni2p, d) Li1s peaks for P-NLC(5, 10, 15, 30)

Table 4.2 Peak positions and weight ratios for all powder samples

	P-N		P-NL	
Name	**Peak (eV)**	**Weight %**	**Peak (eV)**	**Weight %**
Ni2p	855.23	63.84	855.09	58.53
O1s	530.26	23.76	530.14	26.35
C1s	285.37	12.40	285.07	13.84
Li1s	-	-	54.27	1.29

	P-NLM5		P-NLM10		P-NLM15		P-NLM30	
Name	**Peak (eV)**	**Weight %**	**Peak (eV)**	**Weight %**	**Peak (eV)**	**Weight %**	**Peak (eV)**	**Weight %**
Ni2p	854.92	62.97	854.51	57.83	854.97	56.00	854.85	49.26
O1s	529.97	26.84	529.26	26.89	529.99	27.88	529.41	30.33
C1s	285.16	8.68	284.68	11.43	285.07	11.29	284.87	12.6
Li1s	54.53	0.26	54.28	0.41	53.99	0.34	58.14	0.25
Mg1s	1302.73	1.25	1302.57	3.44	1302.89	4.49	1302.67	7.57

	P-NLC5		P-NLC10		P-NLC15		P-NLC30	
Name	**Peak (eV)**	**Weight %**	**Peak (eV)**	**Weight %**	**Peak (eV)**	**Weight %**	**Peak (eV)**	**Weight %**
Ni2p	854.47	50.96	854.43	44.75	854.44	37.56	855.14	40.84
O1s	529.47	24.92	529.47	24.57	529.5	25.03	530.24	22.26
C1s	284.86	19.82	284.87	21.6	284.9	21.96	285.16	18.36
Li1s	53.86	0.76	54.2	0.64	54.15	0.62	55.59	0.35
Cu2p	933.99	3.53	933.8	8.44	933.74	14.83	934.26	18.19

4.2 Characterization of Target Materials

4.2.1 Phase Analysis

XRD results of the targets are shown in Figure 4.9 and Figure 4.10 to evaluate the changes in structure after sintering 1300 °C for 12 hours. Peaks around 37°, 43°, 62°, 76°, and 79° with slight shifts due to doping are associated with (111), (200), (220), (311), and (222) crystal planes of cubic NiO_x according to JCPDS card no. #47-1049, respectively (H. Yan et al., 2014).

Some changes in patterns were observed when additives were incorporated into the structure, especially with Mg and Cu in higher additives ratios. The preferred orientation was changed from (200) to (111) therewithal an increase in peak intensity of (220) for the sample T-NLM15 different from the others. Handwerker et al attributed this behavior to the formation of MgO-NiO solid solution (Handwerker,

Vaudin, & Blendell, 1988). On the other hand, no orientation transition was observed for Cu additive samples. Peak intensities were decreased with increasing Cu ratios, which can be attributed to amorphization with Cu incorporation (Schmahl, Barthel, & Eikerling, 1964).

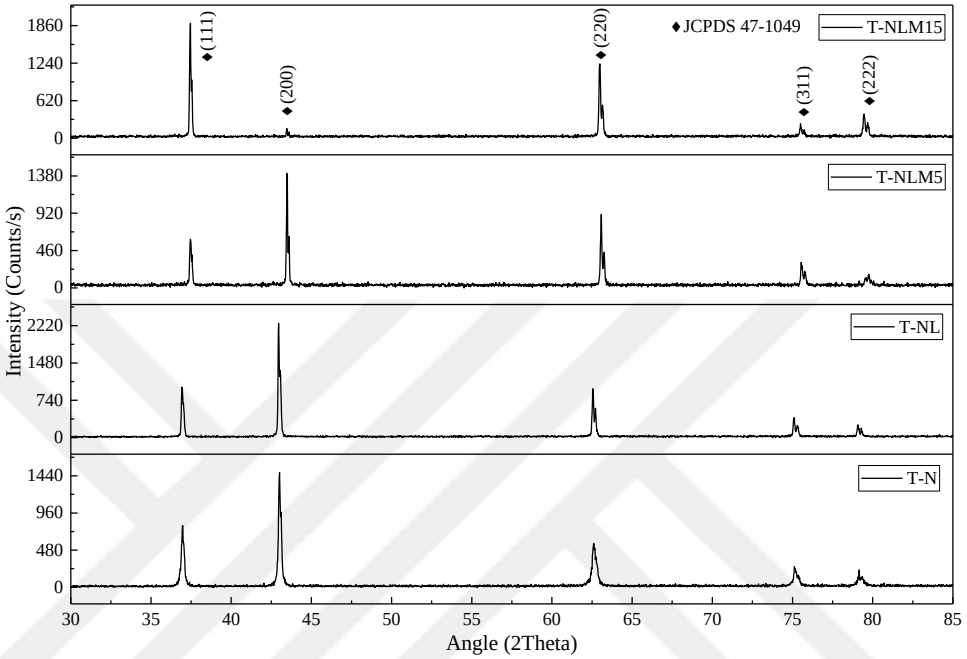

Figure 4.9 XRD pattern of T-N, T-NL, T-NLM5, and T-NLM15 target materials

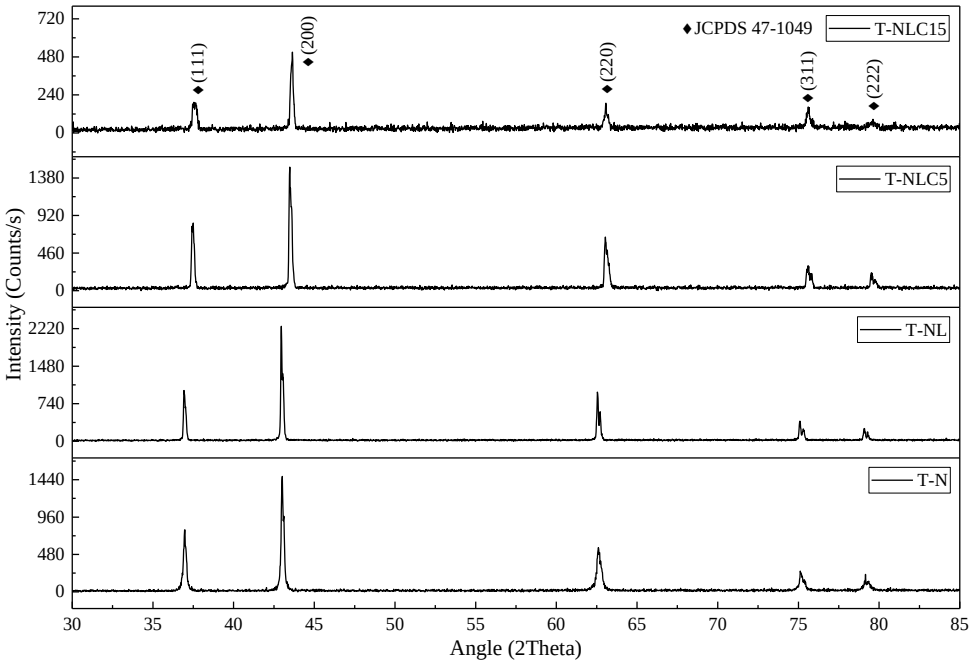

Figure 4.10 XRD pattern of T-N, T-NL, T-NLC5, and T-NLC15 target materials

4.2.2 Elemental Analysis

XPS Survey scans of all target samples are shown in Figure 4.11. Ni2p, O1s, and C1s peaks were detected in all samples. Mg1s, Cu2p, and Li1s peaks were only seen in Mg doped (T-NLM5 and T-NLM15), Cu doped (T-NLC5 and T-NLC15) and Li doped samples (T-NL, T-NLM5, T-NLM15, T-NLC5, and T-NLC15), respectively. Peak positions and percentage of weight for elements are given in Table 4.3.

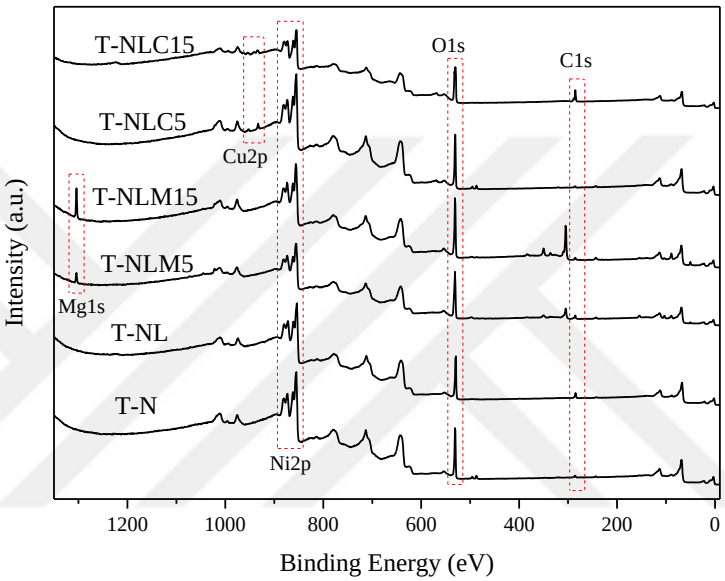

Figure 4.11 XPS survey scans for T-N, T-NL, T-NLM5, T-NLM15, T-NLC5, and T-NLC15

Core level scans of Ni2p, O1s, Mg1s, Cu2p, and Li1s for all targets were presented in Figure 4.12. Peaks around 854 eV, 861 eV, 872 eV, and 879 eV are related to $Ni2p_{3/2}$, $Ni2p_{3/2}$ scatterings, $Ni2p_{1/2}$, and $Ni2p_{1/2}$ scatterings of the quadruple peaks of NiO (J. Chen et al., 2018; W. Huang et al., 2017; H. Yan et al., 2014). O1s deconvoluted peaks around 530 and 531 eV are related to Ni-O binding of NiO (L. Xu et al., 2019). The two deconvoluted peaks around 529.38 eV and 531.18 eV are associated with the Ni-O octahedral binding of NiO (L. Xu et al., 2019). Peaks around 933 eV, 941 eV, 953 eV, and 962 eV are associated with the $Cu2p_{3/2}$, and $Cu2p_{3/2}$ scattering, $Cu2p_{1/2}$, $Cu2p_{1/2}$ scattering, respectively and indicate the presence of Cu in the structure (He et al., 2017). The Mg1s peak seen around 1303 eV indicates the presence of Mg^{2+} in the structure and it is seen that the intensity increases with the

increasing dopant rate (Dong et al., 2018). Although difficult to detect, the presence of Li around 55 eV is observed (J. Chen et al., 2018).

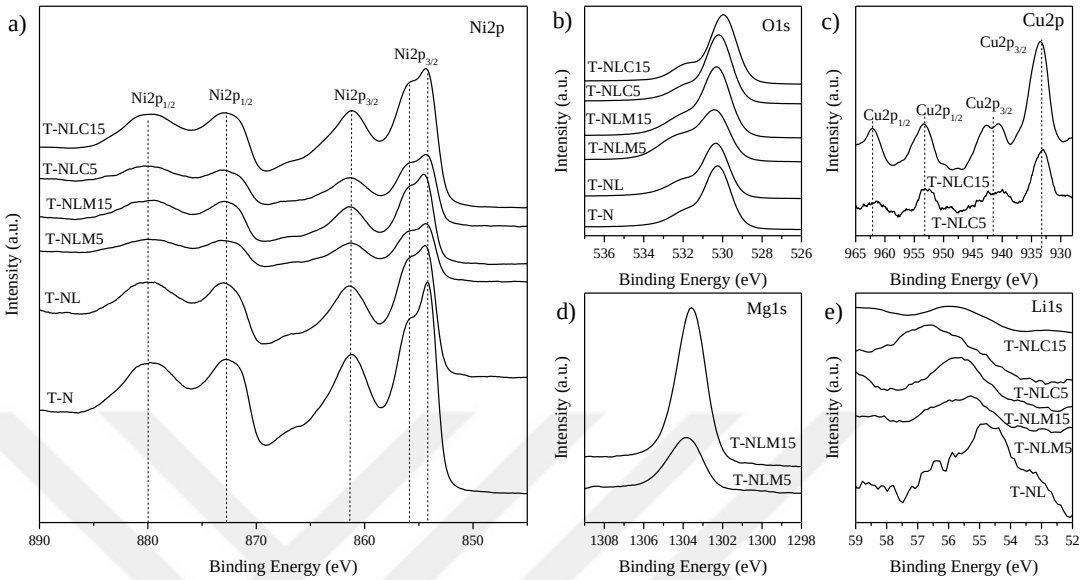

Figure 4.12 XPS core level spectra of a) Ni2p, b) O1s, c) Cu2p, d) Mg1s, and e) Li1s for all targets

Table 4.3 Peak positions and weight ratios for all targets

	T-N		**T-NL**	
Name	**Peak BE**	**Weight %**	**Peak BE**	**Weight %**
Ni2p	855.47	75.13	854.32	71.27
O1s	530.92	22.94	529.54	23.36
C1s	285.82	1.93	284.93	4.53
Li1s	-	-	55.43	0.84

	T-NLM5		**T-NLM15**		**T-NLC5**		**T-NLC15**	
Name	**Peak BE**	**Weight %**	**Peak BE**	**Weight %**	**Peak BE**	**Weight %**	**Peak BE**	**Weight %**
Ni2p	855.35	58.95	855.56	60.58	855.46	73.2	855.21	66.47
O1s	531.22	30.93	530.98	27.23	530.49	22.6	530.34	21.64
C1s	285.33	4.71	285.24	0.88	285.79	1.04	285.16	0.70
Mg1s	1304.13	5.12	1304.03	10.35	-	-	-	-
Cu2p	-	-	-	-	933.13	2.92	934.26	11.03
Li1s	56.34	0.28	55.90	0.96	54.46	0.24	56.08	0.16

4.2.3 Microstructure and Morphology Analysis

The surface morphology of targets was investigated by SEM as shown in Figure 4.13. SEM images show both T-N and T-NL bulk target materials were produced with

high density, low porosity SEM images of NLC5, NLC15, NLM5, and NLM15 target materials were shown in Figure 2.15. In comparison with T-N and T-NL samples, particles size were grown close to 100 µm except for NLC5 which had around 10 µm particle size.

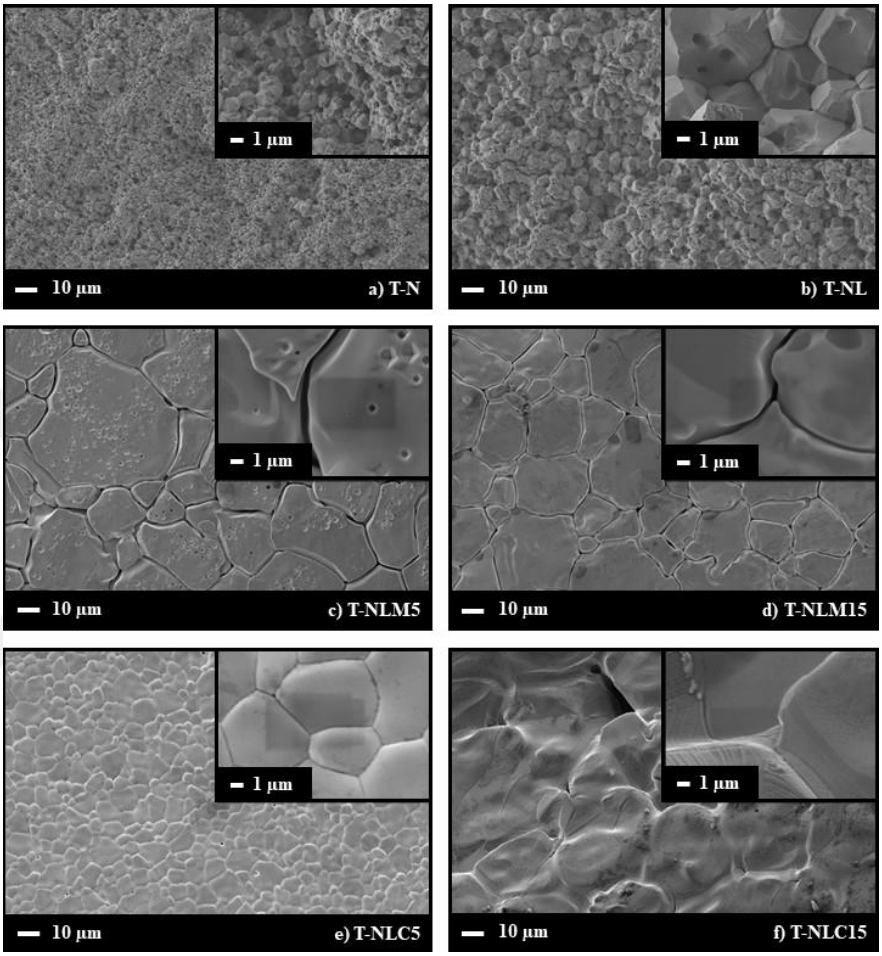

Figure 4.13 SEM images of a) T-N, b) T-NL, c) T-NLM5, d) T-NLM15, e) T-NLC5, and f) T-NLC15

4.2.4 Density

The density of target materials was determined by Archimedes Principle using samples that produced 1 cm in diameter with the same temperature and duration (de Terris et al., 2019). The values of W_K, W_A, W_D, bulk density, apparent solid density, and porosity were given in Table 4.4. The calculated porosity indicates that the target materials were produced with low porosities below 10%, except for the T-NLC15 sample which had a porosity of more than 40%.

Table 4.4 Weights for all samples in different environments, densities, and porosities values

Sample	W_K (g)	W_A (g)	W_D (g)	Bulk Density (g/cm^3)	Apparent Solid Density (g/cm^3)	Porosity (%)
T-N	1.81	1.53	1.82	6.21	6.51	4.67
T-NL	1.81	1.52	1.82	6.12	6.34	3.46
T-NLM5	1.39	1.17	1.42	5.62	6.17	8.87
T-NLM15	1.47	1.23	1.48	5.86	6.15	4.78
T-NLC5	1.53	1.27	1.54	5.61	5.87	4.40
T-NLC15	1.66	1.40	1.87	3.56	6.42	44.54

4.3 Characterization of Thin Films

4.3.1 Phase Analysis

XRD patterns of F-N, F-NL, F-NLM5, F-NLM15, F-NLC5, and F-NLC15 thin films deposited on ITO/glass substrate are shown in Figure 4.14. Peaks seen at 21.52°, 30.64°, 35.52°, 50.94°, 60.56° is well-matched with JCPDS card no. #01-089-4596 of (111)-preferred oriented crystalline ITO film (Raoui, Kiasatpour, Fallah, & Rozatian, 2007; Raoufi & Taherniya, 2015; K. Wang et al., 2014). Since the strong ITO peaks dampen the NiO peaks, the patterns between 36 - 45° are shown in Figure 4.15 for all thin films. Peaks around 37.5° and 43.4° are related to (111) and (200) planes of NiO, while the other peaks around 39.6°, 41.6° are associated with (420) and (332) planes of ITO. Previous phase analyses of NiO (powders and targets) resulted in (200)-preferred orientation. It can be seen from Figure 4.15 that the preferred orientation of NiO phase changed from (200) to (111) for a thin film deposited on ITO substrate.

It is known that substrate temperature and amount of oxygen gas are highly effective on preferred orientation when growing NiO thin film (H. L. Chen & Yang, 2008; Jang, Lu, Hwang, Hsiung, & Wang, 2008; Ryu, Choi, Hong, & Park, 2004). Jang et al correlated the orientation change with the substrate temperature while depositing thin films in the RF-magnetron sputter. It was observed that the orientation changed from (111) to (200) at substrate temperatures above 200 °C (Jang et al., 2008). Chen and Yang deposited NiO films in 0%, 50%, and 100% oxygen environments at 30 °C and 400 °C. Only (200)-preferred orientation film deposited in 100% O_2 at 400 °C. It is stated that this situation is related to O^{2-}. During deposition, Ni^{2+} (0.69 Å) and

O^{2-} (1.40 Å) ions move separately onto the substrate, and the O^{2-} ions must be arranged in a dense-packed (111) form to lower the NiO film surface energy (H. L. Chen & Yang, 2008). In addition, Kumar et al explained that when compared to NiO films of various orientations, the (111) oriented NiO films had a greater conductivity. Hence, NiO films with (111)- highly oriented are attractive for optoelectronic applications (Neetesh Kumar, Lee, Hwang, & Kang, 2020). NiO thin films were deposited with (111)-preferred orientation in a 40% O_2 environment at room temperature, with a full agreement with the literature.

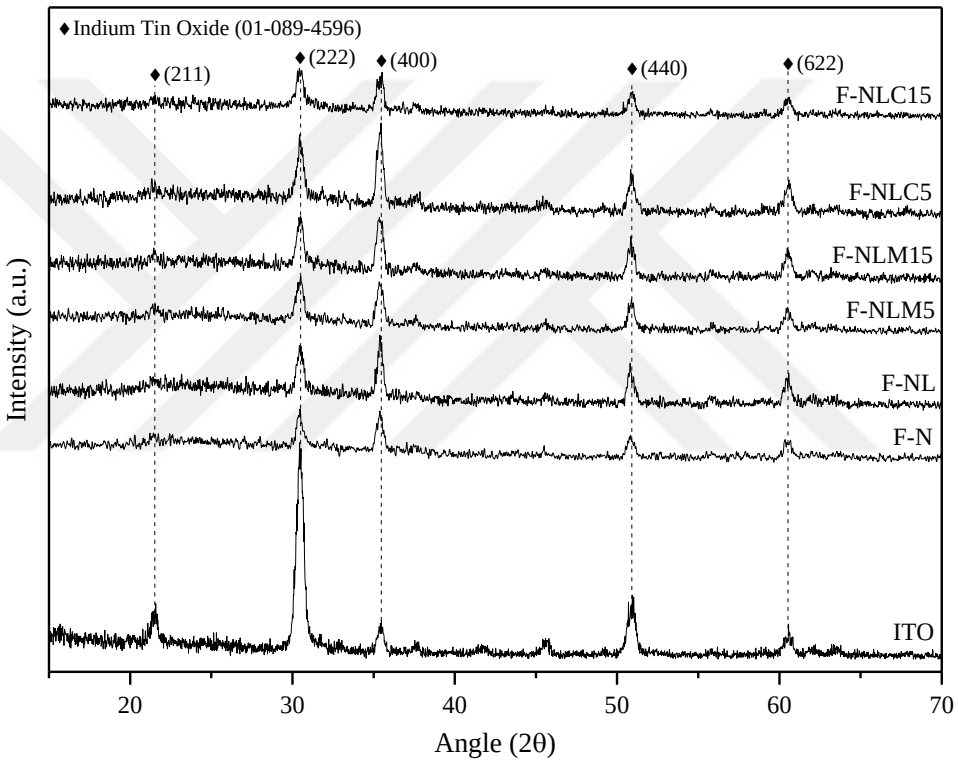

Figure 4.14 XRD patterns of F-N, F-NL, F-NLM5, F-NLM15, F-NLC5, and F-NLC15 thin films

Peak positions, FWHMs, crystallite sizes, d-scaping, and lattice parameters for all powders are given in Table 4.5. NiO(111) and ITO(411) interfere as can be seen from Figure 4.15 and can affect the crystallite size calculated around 37.5°. It is observed that the crystallite size of the Mg-doped samples increases with the increasing additive ratio. Lattice parameters of (111) are nearly identical for all films, while relatively higher differences of (200) for F-NLM15 and F-NLC15. It is about the expansion or contraction of the unit cells while extra atoms enter this structure.

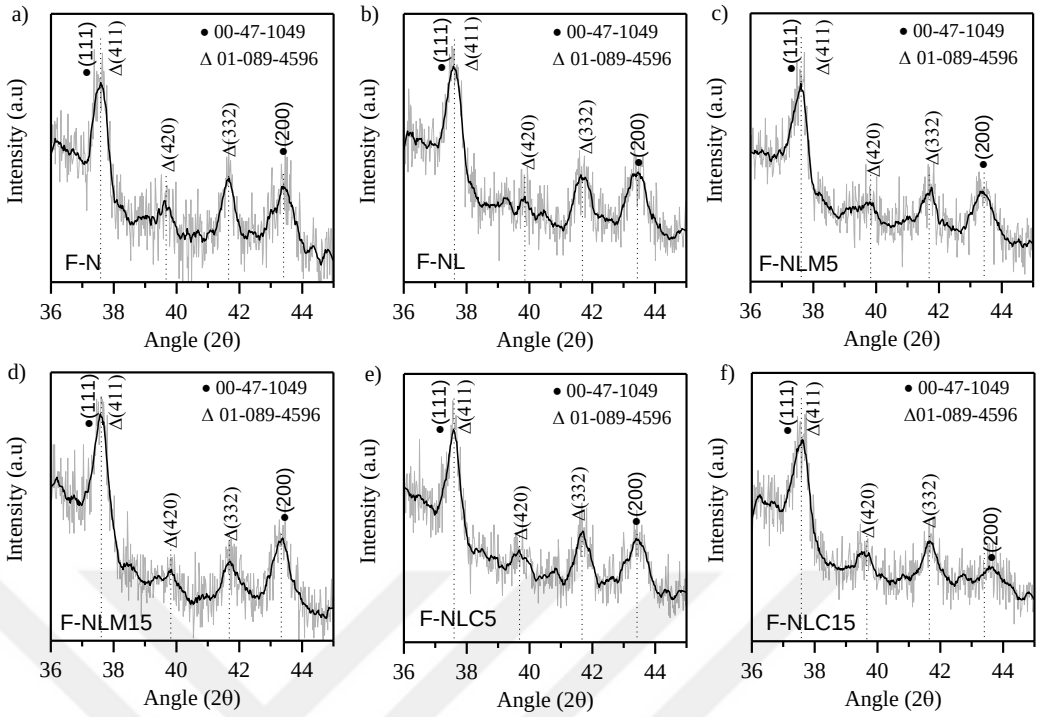

Figure 4.15 XRD patterns of a) F-N, b) F-NL, c) F-NLM5, d) F-NLM15, e) F-NLC5, and f) F-NLC15 thin films between 36-45°

Table 4.5 Peak positions, FWHMs, crystallite sizes, d-spacing, and lattice parameters of (111) and (200) position for all thin films

Sample	(111) Position 2θ (°)	FWHM β(°)	Crystallite size (nm)	a (Å)	(200) Position 2θ (°)	FWHM β(°)	Crystallite size (nm)	a (Å)
F-N	37.5408	0.4580	19.1316	4.1462	43.3786	0.6570	13.5913	4.1685
F-NL	37.5582	0.4991	17.5583	4.1444	43.3822	0.6881	12.9770	4.1682
F-NLC5	37.5533	0.3638	24.0889	4.1449	43.4000	0.6031	14.8081	4.1665
F-NLC15	37.5264	0.5012	17.4834	4.1478	43.5932	0.5076	17.6058	4.1490
F-NLM5	37.5313	0.4746	18.4632	4.1473	43.3684	0.6531	13.6724	4.1694
F-NLM15	37.5593	0.4404	19.8981	4.1443	43.3010	0.5492	16.2553	4.1756

4.3.2 Elemental Analysis

XPS survey spectrum of all thin films was illustrated in Figure 4.16. Peaks of Ni, Cu, Mg, and O elements were seen while Li element was barely viewed as a consequence of its low binding energy. The core level spectra of each elements are given in Figure 4.17 and elements, peak positions, and weight percentage for each films are listed in Table 4.6.

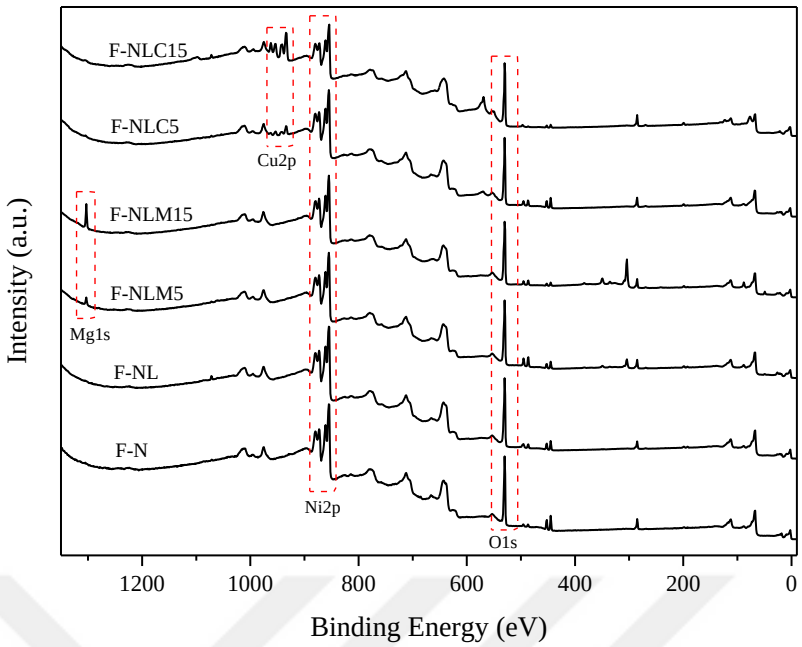

Figure 4.16 XPS survey spectrums of thin films

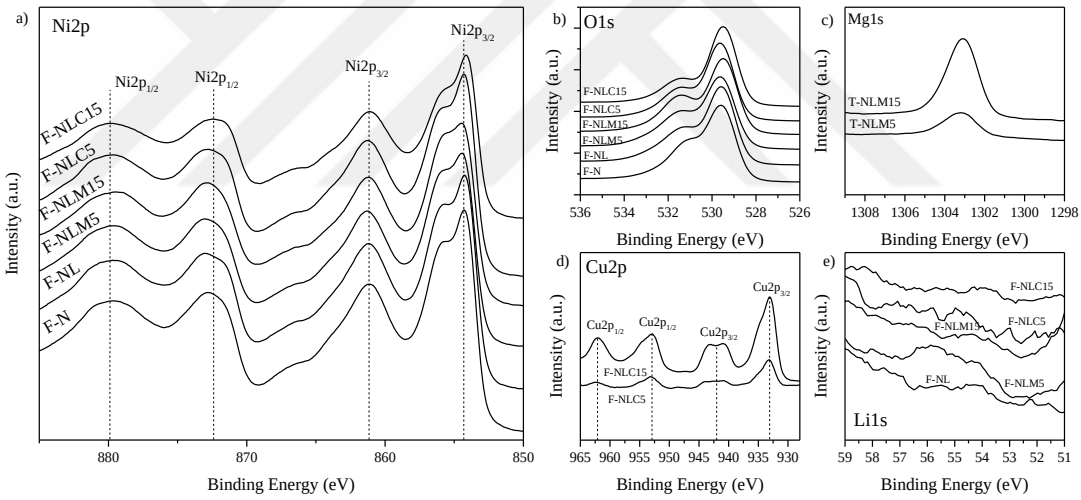

Figure 4.17 XPS core level spectra of a)Ni2p, b)O1s, c)Mg1s, d)Cu2p and e)Li1s

Characteristic $Ni2p_{3/2}$, $Ni2p_{3/2}$ scatterings, $Ni2p_{1/2}$, and $Ni2p_{1/2}$ scatterings were seen around 854 eV, 861 eV, 872 eV, and 879 eV and they are associated with NiO structure (J. Chen et al., 2018; W. Huang et al., 2017; H. Yan et al., 2014). Peak positions around 529 eV and 531 eV are two deconvolutes of O1s related to Ni-O binding (L. Xu et al., 2019). The presence of Mg^{2+} was detected by Mg1s peak around 1303 eV increasing with dopant ratio (Dong et al., 2018). $Cu2p_{3/2}$, $Cu2p_{3/2}$ scattering, $Cu2p_{1/2}$, and $Cu2p_{1/2}$ scattering peaks were seen around 933 eV, 942 eV, 952 eV, and

962 eV, respectively, which indicates presence of Cu^{2+} in the structure (He et al., 2017). Despite the fact that small quantities of Li are difficult to detect because of its low binding energy, the Li1s peak at roughly 55 eV indicates that Li is present in the structure (J. Chen et al., 2018).

Table 4.6 Peak positions and weight ratios for all thin films

	F-N		F-NL	
Name	**Peak BE**	**Weight %**	**Peak BE**	**Weight %**
Ni2p	855.15	72.84	855.17	69.67
O1s	530.16	17.49	530.20	19.18
C1s	285.11	9.67	285.24	11.02
Li1s	-	-	54.12	0.14

	F-NLM5		F-NLM15		F-NLC5		F-NLC15	
Name	**Peak BE**	**Weight %**	**Peak BE**	**Weight %**	**Peak BE**	**Weight %**	**Peak BE**	**Weight %**
Ni2p	855.24	67.86	855.22	61.59	855.25	66.20	855.08	56.45
O1s	530.25	20.67	530.19	22.50	530.22	20.26	530.09	19.34
C1s	285.24	9.28	285.25	11.23	285.29	9.65	285.20	10.43
Mg1s	1303.05	1.99	1303.11	4.55	-	-	-	-
Cu2p	-	-	-	-	933.97	3.74	933.95	13.65
Li1s	54.53	0.21	54.57	0.12	54.95	0.15	53.85	0.13

To examine the off-stoichiometry situation in more detail, the $Ni2p_{3/2}$ between 850-860 eV is divided into two deconvoluted peaks and is shown in Figure 4.18. The ratio between the peak areas around 854 eV and 856 eV are related to ratio of Ni^{2+} and Ni^{3+}, respectively (H. C. Chen, Chen, & Liu, 2021; Gokdemir Choi et al., 2021; Neetesh Kumar et al., 2020). The Ni^{3+} / Ni^{2+} ratio was calculated as 2.94, 3.12, 3.33, 3.03, 3.57, and 4 for F-N, F-NL, F-NLC5, F-NLC15, and F-NLM5, F-NLM15, respectively. It can be expressed that p-type properties were improved with the increase in the additives ratios.

4.3.3 Microstructure and Morphology Analysis

The surface morphology of all thin films was investigated by SEM with 20K and 100K magnifications shown in Figure 4.19. Looking at the images at 20K magnification, it can be seen that all thin films have homogeneous, dense, and smooth surfaces. Additionally, it is seen from morphology that grains have cubic morphologies

and films have grown perpendicular towards the surface (Jamal et al., 2019; Zhao et al., 2014). There was no significant difference as a result of doping. In Cu doped samples, the surface appears to be rougher with doping (Hassan, Saeed, & Elttayef, 2016).

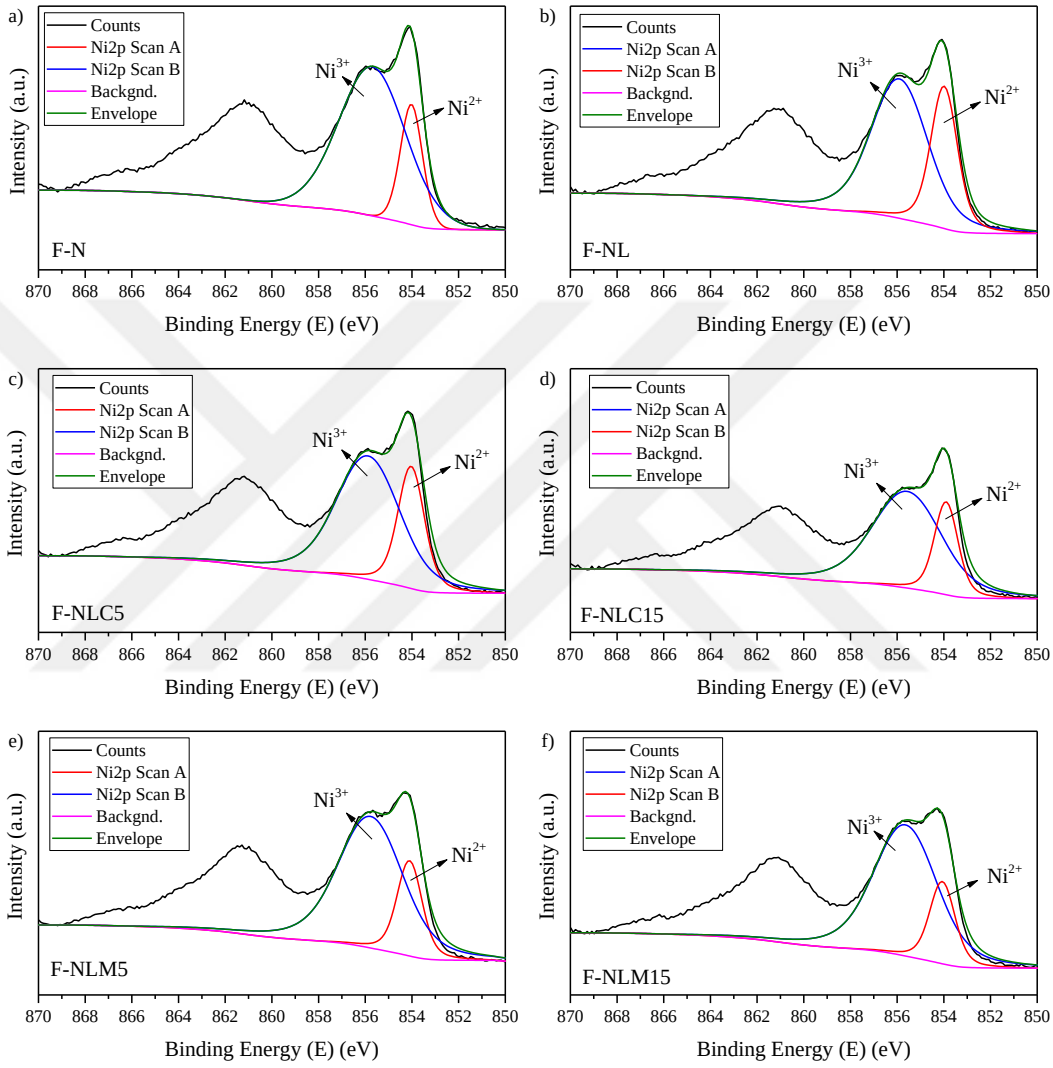

Figure 4.18 $Ni2p_{3/2}$ deconvoluted peaks for all thin films

4.3.4 Electrical and Optical Properties

In order to examine the electrical properties of the films, Hall-Effect measurement was performed and carrier mobilities were measured using Van der Pauw's method (Pauw, 1958). Positive values of all carrier concentrations attributed to the films that are p-type. In general, the carrier mobility increased with an increase in additives in

accordance with the literature (Table 4.7). This increase can be explained by the replacement of dopant atoms with Ni^{2+} and promoting the conversion of Ni^{2+} to Ni^{3+} for charge balance, therefore increasing hole mobility. (Guo, Hui, & Hui, 2013).

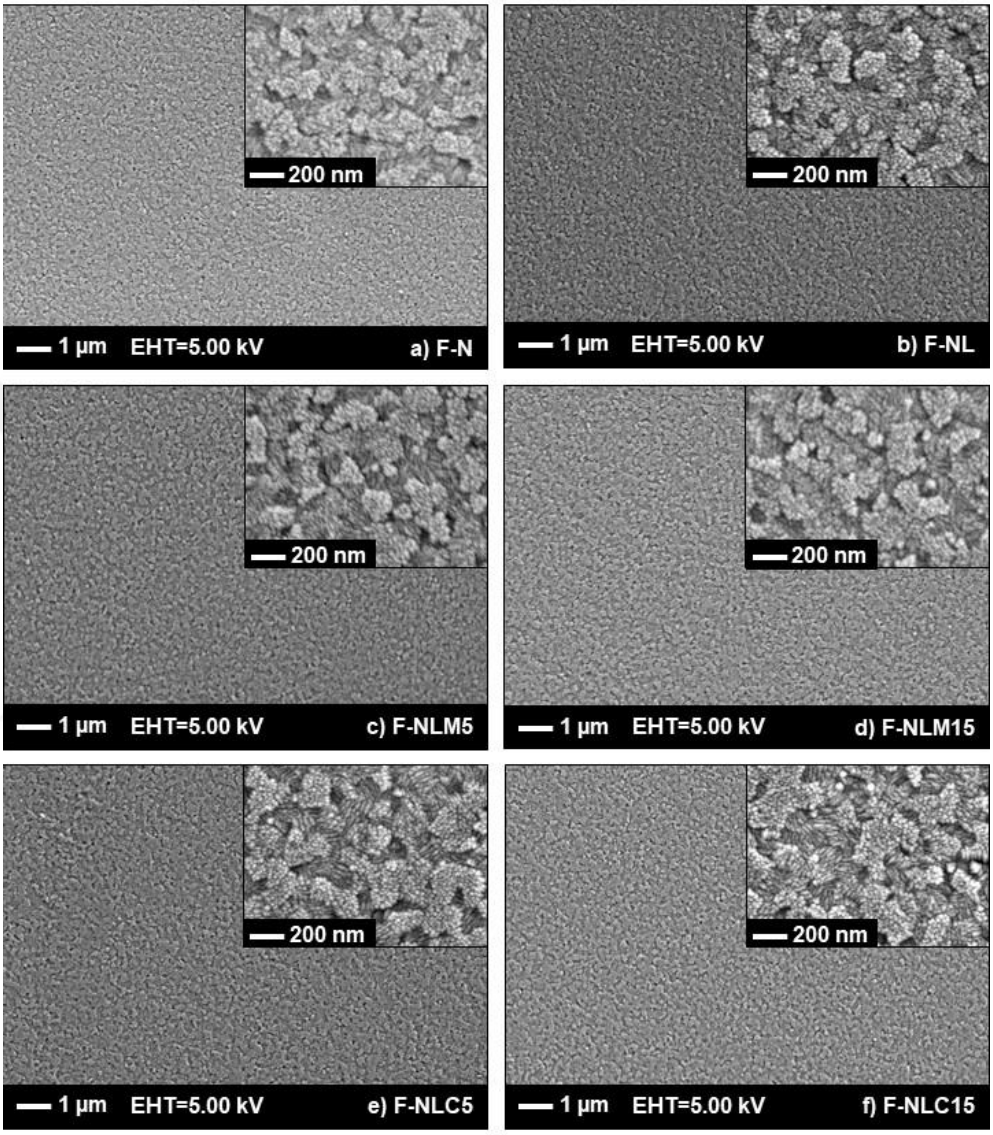

Figure 4.19 SEM images of a) F-N, b) F-NL, c) F-NLM5, d) F-NLM15, e) F-NLC5, and f) F-NLC15

The optical properties of thin films were investigated by UV-Vis spectrophotometer as shown in Figure 4.20. All thin films were analyzed as coated on ITO due to their type of usage in solar cells. For reference, the transmittance spectra of the ITO/glass substrate was measured. All samples showed an increase in their transmittance after 300 nm and are highly transparent in the visible region. Maximum and minimum transmittance values are given in Table 4.7. In the 590 - 615 nm range, all samples

show more than 90% transparency. In PCSs with p-i-n structure, high transparency is very important for the light to reach the absorber layer since it enters from the p-type part. There are changes in transmitting properties with different doping, and this is related to the optical bandgap of the thin film. The Tauc model is used to observe this relationship (Sta et al., 2015):

$$\alpha h\nu = A(h\nu - E_g)^{1/2} \tag{4.4}$$

where α is absorption coefficient, $h\nu$ is photon energy, A is constant and E_g is bandgap. E_g (eV) - $\alpha h\nu$ ($eV^2.cm^{-2}$) graph is plotted to give the bandgap, the value that intercepts the x-axis from the slope. Figure 4.21, Figure 4.22, Figure 4.23, Figure 4.24, Figure 4.25, and Figure 4.26 present the optical bandgap plots of F-N, F-NL, F-NLM5, F-NLM15, F-NLC5, and F-NLC15 thin films. All bandgap values are given in Table 4.7. The bandgap increases from 3.74 to 3.86 with Li doping in parallel with the literature (Sta et al., 2015). With the addition of Mg, the bandgap reached the level of 3.85-3.84 eV. Amor et al. showed that the bandgap increased with the addition of Mg to NiO (Ben Amor et al., 2014). The bandgap was calculated as 3.91 eV and 3.90 eV with the addition of Cu. Chen and colleagues showed that the transmittance value of NiO film decreased with increasing Cu doping ratio, and they attributed this to the scattering of incident light by grain boundaries from Cu clusters (S. C. Chen, Kuo, Lin, & Lin, 2011).

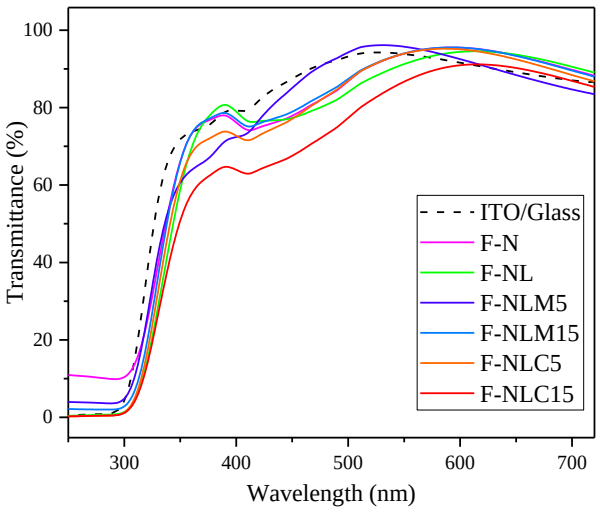

Figure 4.20. Transmittance spectra of all thin films

Table 4.7 Optical properties, bandgaps, and hole mobilities of all thin films

Sample	Hole Mobility (cm^2/Vs)	Maximum Transmittance (%)	Maximum Wavelength (nm)	Minimum Transmittance (%)	Minimum Wavelength (nm)	Bandgap (eV)
F-N	$1.2x10^3$	95.586	592	9.693	294	3.74
F-NL	$1.47x10^3$	94.602	613	0.358	239	3.86
F-NLM5	$8.53x10^3$	96.198	530	3.497	293	3.85
F-NLM15	$2.36x10^3$	95.598	592	1.98	292	3.84
F-NLC5	$3.06x10^3$	95.247	586	0.2	241	3.91
F-NLC15	$6.93x10^3$	91.221	611	0.224	240	3.90

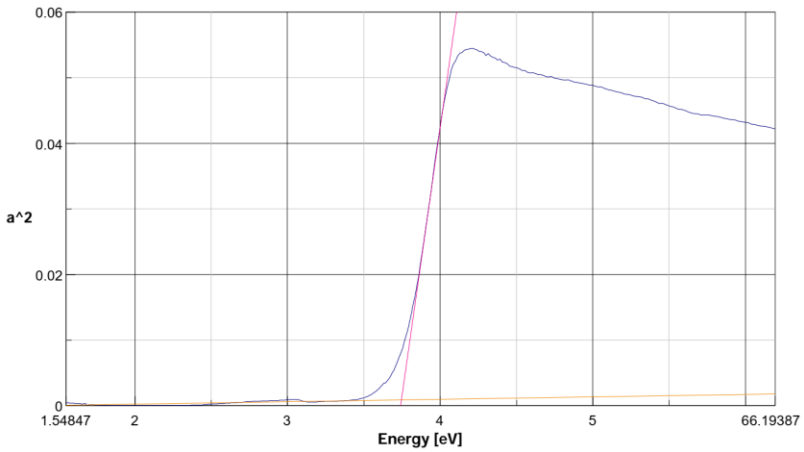

Figure 4.21 Optical bandgap of F-N

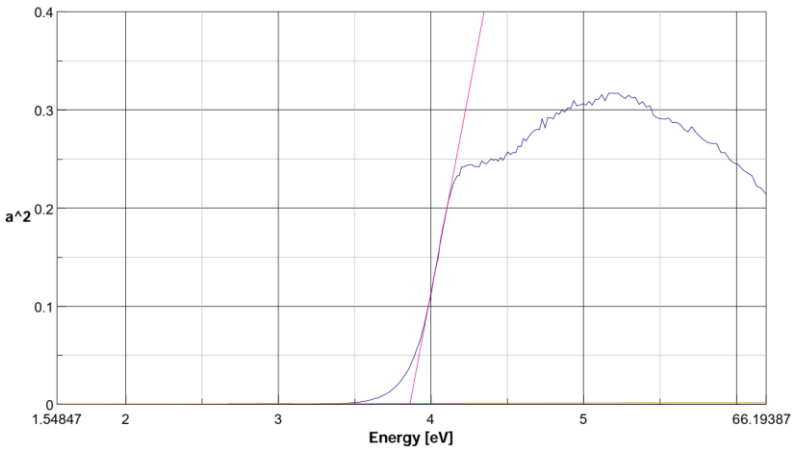

Figure 4.22 Optical bandgap of F-NL

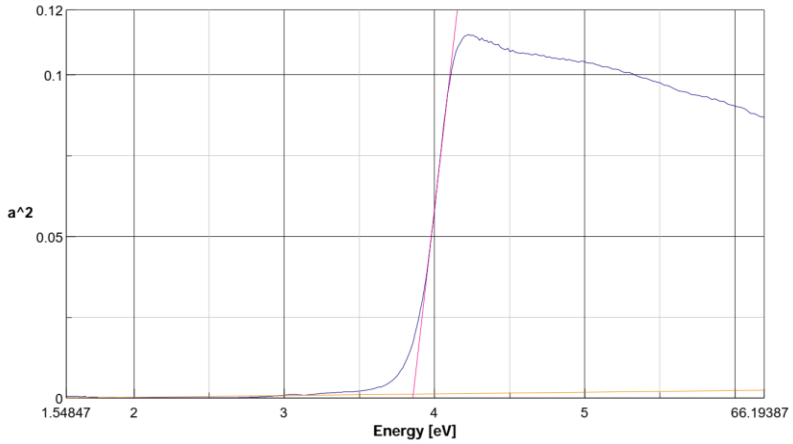

Figure 4.23 Optical bandgap of F-NLM5

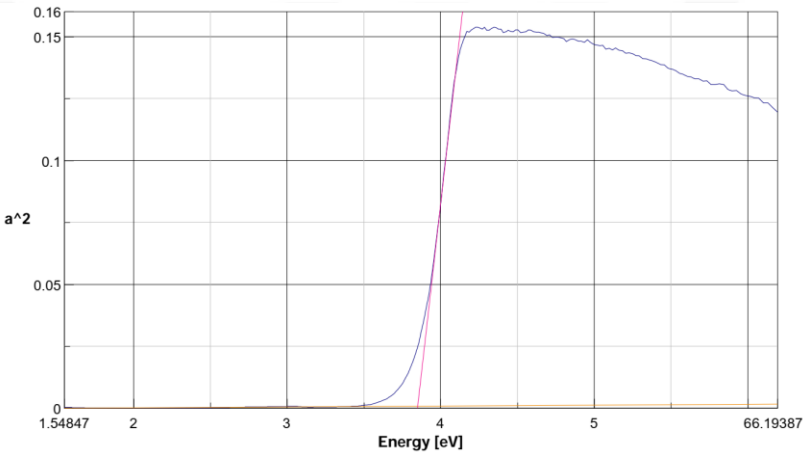

Figure 4.24 Optical bandgap of F-NLM15

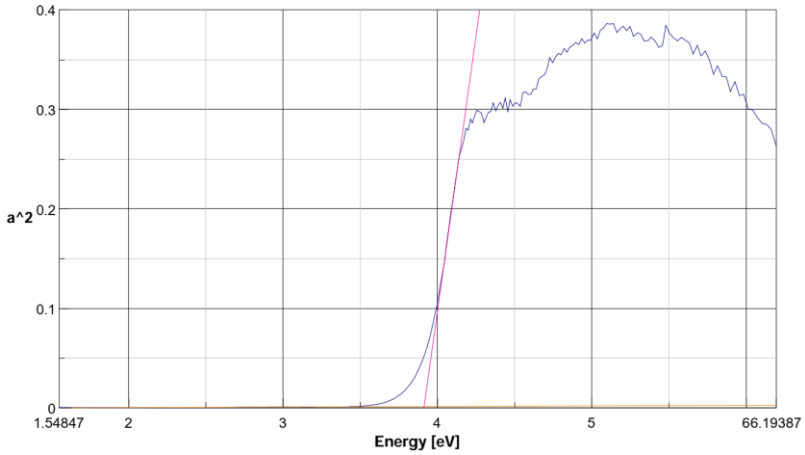

Figure 4.25 Optical bandgap of F-NLC5

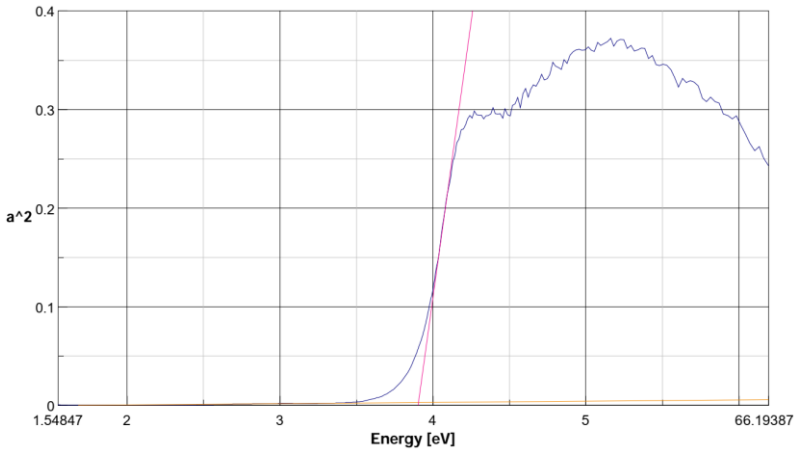

Figure 4.26 Optical bandgap of F-NLC15

In order to understand the film quality and carrier recombinations, PL measurements of PSKs coated on different HTM layers were carried out. Results in Figure 4.27 show that PL intensities increase as F-N, F-NL, F-NLC15, F-NLC5, F-NLM5, and F-NLM15, respectively. Huang and colleagues carried out a similar study and showed that the Mg doped NiO film had a higher PL intensity compared to the pristine film. They interpreted this situation that the PSK deposited on the film has high quality and crystallinity (L. Huang et al., 2021).

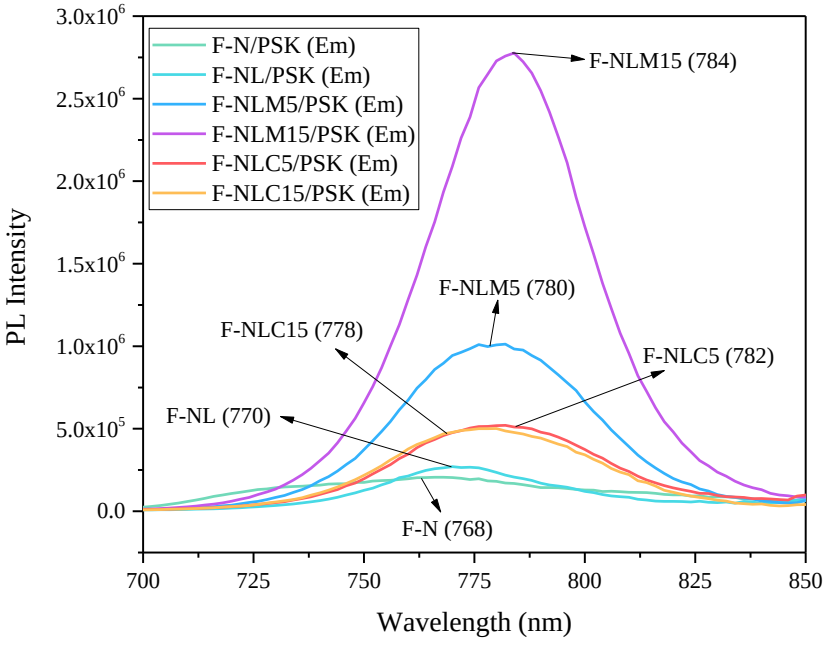

Figure 4.27 PL measurements of PSK coated on HTM layers

4.4 Photovoltaic Characterization

NiO_x-based thin films produced and characterized systematically were employed in PSCs as HTMs and the fabricated devices were tested under standard conditions using solar simulator. There are 6 and 3 cells on each architecture with 0.04 cm^2 and 0.1 cm^2 for S1 and S2, respectively, which can be seen in Figure 4.28. Measurements were taken from each cell on all samples. The champion efficiencies of all devices from S1 and S2 groups are shown in Figure 4.29 and values are listed in Table 4.8. The champion PCE of 11.17% was obtained with the S1-NLM5 sample after S1-NL sample (11.09%) for the first group, while the best PCE of 15.31% was obtained with S2-N sample after S2-NLM5 sample (15.24%) for the second group.

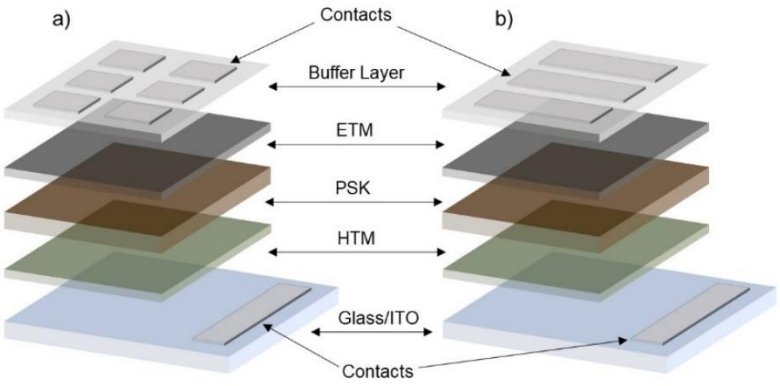

Figure 4.28 Solar cell architecture for a) Set 1 (S1) and b) Set 2 (S2)

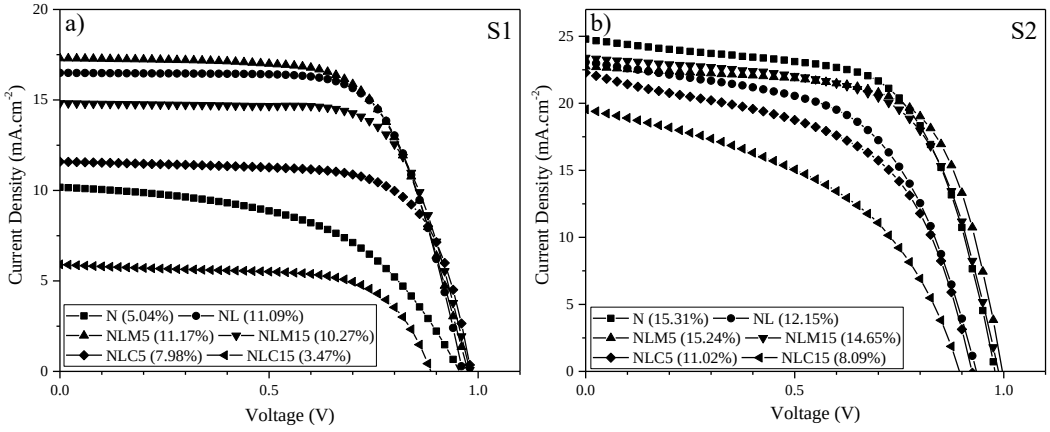

Figure 4.29 Champion efficiency values of a) S1 and b) S2 groups solar cells

Table 4.8 Photovoltaic results of champion cells

Sample	Area (cm^2)	JSC ($mA.cm^{-2}$)	VOC (V)	FF	PCE (%)
S1-N	0.04	10.2	0.940	0.53	5.04
S1-NL	0.04	16.5	0.960	0.70	11.09
S1-NLM5	0.04	17.3	0.960	0.67	11.17
S1-NLM15	0.04	14.8	0.980	0.71	10.27
S1-NLC5	0.04	11.6	0.980	0.70	7.98
S1-NLC15	0.04	5.9	0.880	0.67	3.47
S2-N	0.10	25.0	0.975	0.64	15.31
S2-NL	0.10	21.2	0.975	0.62	12.80
S2-NLM5	0.10	22.7	0.975	0.69	15.24
S2-NLM15	0.10	23.3	0.975	0.64	14.65
S2-NLC5	0.10	22.1	0.900	0.56	11.02
S2-NLC15	0.10	19.4	0.875	0.48	8.09

For better comparison, distributions of PCE, FF, V_{OC}, and J_{SC} values for all measurements are given in Figure 4.30. When the PCE values are compared, it is seen that the S2 group generally achieved higher efficiencies. For HTM layers, it is seen that it has a similar distribution in general, except N and NL. It is seen that this difference is due to J_{SC} values. When the FF values are compared, it is seen that the S1 group gives higher results, as can be seen from Figure 4.30. It can be said that S1 group cells have higher MPP values. When the VOC values are compared, the S2 group shows a very homogeneous distribution at high values, except for the S2-N and S2-NLC15 samples. These wide distributions are thought to be due to coating defects or less quality of the layers. Considering that each cell consists of at least 5 layers of architecture, a deficiency in any of the layers directly affects the efficiency of the cell. S2 group cells have higher values in J_{SC} values. This is the primary reason for higher efficiencies. Considering both groups of partners, it can be said that the NLM5 sample gives the best results.

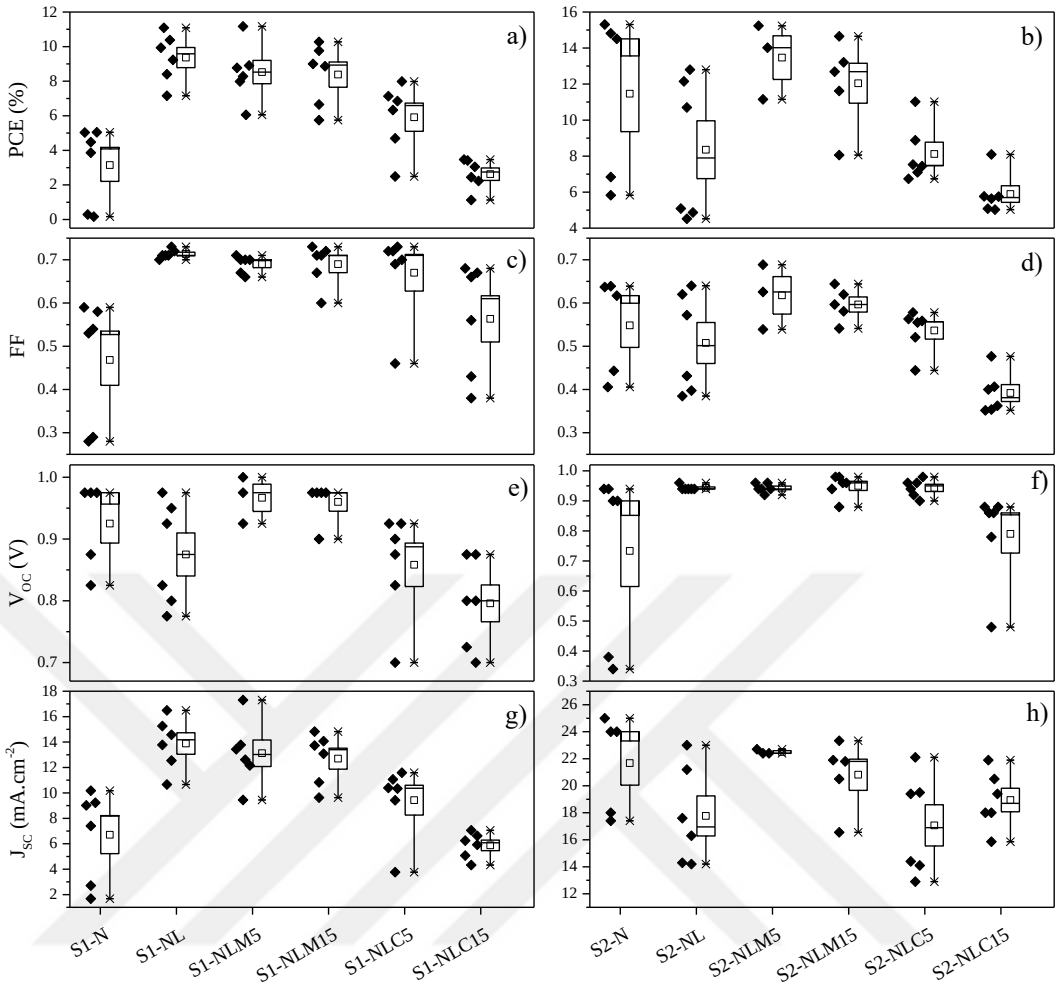

Figure 4.30 Distribution of PCE, FF, V_{OC}, and J_{SC} for all samples

CHAPTER FIVE
CONCLUSION

5.1 Conclusion

Nickel oxide powders were successfully produced cubic NiO phase according to JCPDS card no. #47-1049 at 650 °C by using nickel nitrate hexahydrate for matrix precursor and lithium nitrate, magnesium acetate tetrahydrate, and copper nitrate trihydrate for dopant precursors. High dense sputter targets were produced from powders by pressed in CIP and sintered at 1200 °C. Uniform, homogeneous, and dense NiO-based thin films were deposited on ITO substrate by using targets with different additive ratios. It was analyzed that the additive rates in the films were close to the additive rates in the powders. It was also investigated that the additives increase the off-stoichiometry, thereby improving the hole mobility. Perovskite solar cells using these films as HTM layers were produced and their efficiencies were examined. As a consequence, perovskite solar cells were successfully produced with the champion efficiency of %11.17 and 15.31% for S1-NLM5 and S2-N, respectively.

5.2 Future Plans

In this study, the effect of different additives for the HTM layer on perovskite solar cell efficiency was observed. As it is known, PSCs are multi-layered structures, each layer is very crucial and directly affects the working or efficiency of the device. Stability in PSCs is still one of the biggest challenges. For this reason, the following remarks are suggestions for future studies:

- Although spin coating is a very frequent and fast method for lab-scale, it is not applicable for mass production. It will be more beneficial to use a method that can be adapted to mass production to simulate real environmental conditions for the next developments.
- There are stability problems of organic structures. The use of alternative inorganic structures instead of organic structures will be able to eliminate

this challenge. It will also create an environment for the production of more economical PSCs.

REFERENCES

Adachi, H., & Wasa, K. (2012). Thin films and nanomaterials. In *Handbook of Sputtering Technology* (2nd ed., pp. 3–39). Oxford: Elsevier. https://doi.org/10.1016/B978-1-4377-3483-6.00001-2

Ahmed, R. A., Pang, Y. X., Olea, M., & Hodgson, S. N. B. (2012). Preparation and structural characterisation of SBA-15 supported nickel catalysts via sol-gel nickel oxide coatings for dry reforming of methane. *WIT Transactions on Engineering Sciences, 80*, 71–82. https://doi.org/10.2495/PMR120071

Akalin, S. A., Erol, M., Uzunbayir, B., Oguzlar, S., & Yildirim, S. (2021). Sol-gel derived Li and Mg incorporated nickel oxide particles: An investigation on structural and optical properties. *Optical Materials*, *118*, 111223. https://doi.org/10.1016/j.optmat.2021.111223

Alagiri, M., Ponnusamy, S., & Muthamizhchelvan, C. (2012). Synthesis and characterization of NiO nanoparticles by sol-gel method. *Journal of Materials Science: Materials in Electronics*, *23*(3), 728–732. https://doi.org/10.1007/s10854-011-0479-6

Amor, M. B., Boukhachem, A., Boubaker, K., & Amlouk, M. (2014). Structural, optical and electrical studies on Mg-doped NiO thin films for sensitivity applications. *Materials Science in Semiconductor Processing*, *27*, 994–1006.

Arora, N., Dar, M. I., Hinderhofer, A., Pellet, N., Schreiber, F., Zakeeruddin, S. M., et al. (2017). Perovskite solar cells with CuSCN hole extraction layers yield stabilized efficiencies greater than 20%. *Science*, *358*(6364), 768–771.

Arumugam, G. M., Karunakaran, S. K., Liu, C., Zhang, C., Guo, F., Wu, S., et al. (2021). Inorganic hole transport layers in inverted perovskite solar cells: A review. *Nano Select, 2*(6), 1081–1116. https://doi.org/10.1002/nano.202000200

Barbato, M., Artegiani, E., Bertoncello, M., Meneghini, M., Trivellin, N., Mantoan, E., et al. (2021). CdTe solar cells: Technology, operation and reliability. *Journal of Physics D: Applied Physics*, *54*(33). https://doi.org/10.1088/1361-6463/ac04e3

Bonnet, D., & Rabenhorst, H. (1972). New results on the development of a thin-film p-CdTe-n-CdS heterojunction solar cell. *Photovoltaic Specialists Conference, 9 Th, Silver Spring, Md*, 129–132.

Brinker, C. J., & Scherer, G. W. (2013). *Sol-gel science: The physics and chemistry of sol-gel processing*. London: Academic Press.

Callister, W. D., & Rethwisch, D. G. (2018). *Materials science and engineering: An introduction* (10th ed.). New York: Wiley.

Carlson, D. E., & Wronski, C. R. (1976). Amorphous silicon solar cell. *Applied Physics Letters*, *28*(11), 671. https://doi.org/10.1063/1.88617

Chapin, D. M., Fuller, C. S., & Pearson, G. L. (1954). A new silicon p-n junction photocell for converting solar radiation into electrical power. *Journal of Applied Physics*, *25*(5), 676. https://doi.org/10.1063/1.1721711

Chen, H. C., Chen, Y. R., & Liu, T. F. (2021). Photoelectrochemical performance of a UV-cured all-solid-state complementary ITO/WO3/Ta2O5/electrolyte/NiO/ITO electrochromic device deposited by ion-beam assisted electron-beam evaporation. *Electrochimica Acta*, *382*, 138355. https://doi.org/10.1016/j.electacta.2021.138355

Chen, H. L., & Yang, Y. S. (2008). Effect of crystallographic orientations on electrical properties of sputter-deposited nickel oxide thin films. *Thin Solid Films*, *516*(16),

Chen, J., Wu, X., Tan, Q., & Chen, Y. (2018). Designed synthesis of ultrafine NiO nanocrystals bonded on a three dimensional graphene framework for high-capacity lithium-ion batteries. *New Journal of Chemistry*, *42*(12), 9901–9910.

Chen, S. C., Kuo, T. Y., Lin, Y. C., & Lin, H. C. (2011). Preparation and properties of p-type transparent conductive Cu-doped NiO films. *Thin Solid Films*, *519*(15), 4944–4947. https://doi.org/10.1016/j.tsf.2011.01.058

Chen, W., Wu, Y., Yue, Y., Liu, J., Zhang, W., Yang, X., et al. (2015). Efficient and stable large-area perovskite solar cells with inorganic charge extraction layers. *Science*, *350*(6263), 944–948. https://doi.org/10.1126/science.aad1015

Chi, W., & Banerjee, S. K. (2020). Progress in materials development for the rapid efficiency advancement of perovskite solar cells. *Small*, *16*(28), 1–24. https://doi.org/10.1002/smll.201907531

Chwang, R., Smith, B. J., & Crowell, C. R. (1974). Contact size effects on the van der Pauw method for resistivity and Hall coefficient measurement. *Solid State Electronics*, *17*(12), 1217–1227. https://doi.org/10.1016/0038-1101(74)90001-X

de Terris, T., Andreau, O., Peyre, P., Adamski, F., Koutiri, I., Gorny, C., et al. (2019). Optimization and comparison of porosity rate measurement methods of Selective Laser Melted metallic parts. *Additive Manufacturing*, *28*(April), 802–813. https://doi.org/10.1016/j.addma.2019.05.035

Dilsiz, N., & Akovali, G. (2002). Study of sol–gel processing for fabrication of low density alumina microspheres. *Materials Science and Engineering: A*, *332*(1–2), 91–96. https://doi.org/10.1016/S0921-5093(01)01726-9

Dirksen, J. A., Duval, K., & Ring, T. A. (2001). NiO thin-film formaldehyde gas sensor. *Sensors and Actuators B: Chemical*, *80*(2), 106–115.

Docampo, P., Ball, J. M., Darwich, M., Eperon, G. E., & Snaith, H. J. (2013). Efficient organometal trihalide perovskite planar-heterojunction solar cells on flexible polymer substrates. *Nature Communications*, *4*(1), 1–6. https://doi.org/10.1038/ncomms3761

Dong, D., Wang, W., Barnabé, A., Presmanes, L., Rougier, A., Dong, G., et al. (2018). Enhanced electrochromism in short wavelengths for NiO:(Li, Mg) films in full inorganic device ITO/NiO:(Li, Mg)/Ta2O5/WO3/ITO. *Electrochimica Acta*, *263*, 277–285. https://doi.org/10.1016/j.electacta.2018.01.049

Dorey, R. (2012). Routes to thick films: What is a thick film? How is it made? *Ceramic Thick Films for MEMS and Microdevices*, 35–61. https://doi.org/10.1016/B978-1-4377-7817-5.00002-X

Dubey, P., & Kaurav, N. (2020). Stoichiometric and nonstoichiometric compounds. In *Structure processing properties relationships in stoichiometric and nonstoichiometric oxides* (p. 20). London: IntechOpen. https://doi.org/10.5772/intechopen.89402

Erten-Ela, S., Ueno, Y., Asaba, T., & Kubo, Y. (2017). Synthesis of a dibenzo-BODIPY-incorporating phenothiazine dye as a panchromatic sensitizer for dye-sensitized solar cells. *New Journal of Chemistry*, *41*(18), 10367–10375. https://doi.org/10.1039/C7NJ01735A

Fu, Q., Tang, X., Huang, B., Hu, T., Tan, L., Chen, L., et al. (2018). Recent progress on the long-term stability of perovskite solar cells. *Advanced Science*, *5*(5). https://doi.org/10.1002/advs.201700387

Ge, B., Qiao, H. W., Lin, Z. Q., Zhou, Z. R., Chen, A. P., Yang, S., et al. (2019). Deepening the valance band edges of NiOx contacts by alkaline earth metal doping for efficient perovskite photovoltaics with high open-circuit voltage. *Solar RRL*, *3*(8), 1–7. https://doi.org/10.1002/solr.201900192

German, R. M. (2005). *Powder metallurgy and particulate materials processing: the processes, materials, products, properties and applications*. Princeton: Metal Powder Industries Federation.

German, R. M. (2010). Thermodynamics of sintering. In *Sintering of advanced materials: Fundamentals and processes* (pp. 3–32). Cambridge: Woodhead Publishing Limited. https://doi.org/10.1533/9781845699949.1.110

Gokdemir Choi, F. P., Moeini Alishah, H., Bozar, S., Kahveci, C., Canturk Rodop, M., & Gunes, S. (2021). First demonstration of lithium, cobalt and magnesium introduced nickel oxide hole transporters for inverted methylammonium lead triiodide based perovskite solar cells. *Solar Energy*, *215*, 434–442. https://doi.org/10.1016/j.solener.2020.12.068

Gorjian, S., & Shukla, A. (2020). *Photovoltaic solar energy conversion* (1st ed.). London: Elsevier. https://doi.org/10.1016/C2018-0-05265-2

Green, M. A., Dunlop, E. D., Hohl-Ebinger, J., Yoshita, M., Kopidakis, N., & Hao, X. (2021). Solar cell efficiency tables (Version 58). *Progress in Photovoltaics: Research and Applications*, *29*(7), 657–667. https://doi.org/10.1002/pip.3444

Guo, W., Hui, K. N., & Hui, K. S. (2013). High conductivity nickel oxide thin films by a facile sol-gel method. *Materials Letters*, *92*, 291–295.

Handwerker, C. A., Vaudin, M. D., & Blendell, J. E. (1988). Equilibrium crystal shapes and surface phase diagrams at surfaces in ceramics. *Le Journal de Physique Colloques*, *49*(C5), 367–373. https://doi.org/10.1051/jphyscol:1988542

Hassan, E. S., Saeed, A. A., & Elttayef, A. K. (2016). Doping and thickness variation influence on the structural and sensing properties of NiO film prepared by RF-magnetron sputtering. *Journal of Materials Science: Materials in Electronics*,

He, Q., Yao, K., Wang, X., Xia, X., Leng, S., & Li, F. (2017). Room-temperature and solution-processable Cu-doped nickel oxide nanoparticles for efficient hole-transport layers of flexible large-area perovskite solar cells. *ACS Applied Materials and Interfaces*, *9*(48), 41887–41897. https://doi.org/10.1021/acsami.7b13621

Hersch, P., & Zweibel, K. (1982). *Basic photovoltaic principles and methods*. Washington: Technical Information Office, Solar Energy Research Institute. https://doi.org/10.2172/5191389

Hu, L., Peng, J., Wang, W., Xia, Z., Yuan, J., Lu, J., et al. (2014). Sequential deposition of CH3NH3PbI3 on planar NiO film for efficient planar perovskite solar cells. *ACS Photonics*, *1*(7), 547–553. https://doi.org/10.1021/ph5000067

Hu, Z., Chen, D., Yang, P., Yang, L., Qin, L., Huang, Y., et al. (2018). Sol-gel-processed yttrium-doped NiO as hole transport layer in inverted perovskite solar cells for enhanced performance. *Applied Surface Science*, *441*, 258–264. https://doi.org/10.1016/j.apsusc.2018.01.236

Huang, A. B., Zhu, J. T., Zheng, J. Y., Yu, Y., Liu, Y., Yang, S. W., et al. (2016). Achieving high-performance planar perovskite solar cells with co-sputtered Co-doping NiOx hole transport layers by efficient extraction and enhanced mobility. *Journal of Materials Chemistry C*, *4*(46), 10839–10846. https://doi.org/10.1039/c6tc03624d

Huang, A., Lei, L., Chen, Y., Yu, Y., Zhou, Y., Liu, Y., et al. (2018). Minimizing the energy loss of perovskite solar cells with Cu+ doped NiOx processed at room temperature. *Solar Energy Materials and Solar Cells*, *182*(March), 128–135. https://doi.org/10.1016/j.solmat.2018.01.025

Huang, L., Wang, Y., Zhu, X., Zhao, X., Li, G., Li, L., et al. (2021). Mg-doped nickel oxide as efficient hole-transport layer for perovskite photodetectors. *Journal of Physical Chemistry C*, *125*(29), 16066–16074.

Huang, W., Ding, S., Chen, Y., Hao, W., Lai, X., Peng, J., et al. (2017). 3D NiO hollow sphere/reduced graphene oxide composite for high-performance glucose biosensor. *Scientific Reports*, *7*(1), 1–11. https://doi.org/10.1038/s41598-017-05528-1

Jamal, M. S., Shahahmadi, S. A., Chelvanathan, P., Alharbi, H. F., Karim, M. R., Ahmad Dar, M., et al. (2019). Effects of growth temperature on the photovoltaic properties of RF sputtered undoped NiO thin films. *Results in Physics*, *14*. https://doi.org/10.1016/j.rinp.2019.102360

James, S., & Contractor, R. (2018). Study on nature-inspired fractal design-based flexible counter electrodes for dye-sensitized solar cells fabricated using additive manufacturing. *Scientific Reports*, *8*(1), 1–12. https://doi.org/10.1038/s41598-018-35388-2

Jang, W. L., Lu, Y. M., Hwang, W. S., Hsiung, T. L., & Wang, H. P. (2008). Effect of substrate temperature on the electrically conductive stability of sputtered NiO films. *Surface and Coatings Technology*, *202*(22–23), 5444–5447. https://doi.org/10.1016/j.surfcoat.2008.06.025

Jeong, J., Kim, M., Seo, J., Lu, H., Ahlawat, P., Mishra, A., et al. (2021). Pseudo-halide anion engineering for α-FAPbI3 perovskite solar cells. *Nature*, *592*(7854), 381–385. https://doi.org/10.1038/s41586-021-03406-5

Ji, J. M., Zhou, H., Eom, Y. K., Kim, C. H., & Kim, H. K. (2020). 14.2% efficiency dye-sensitized solar cells by Co-sensitizing novel Thieno[3,2-b]indole-based organic dyes with a promising porphyrin sensitizer. *Advanced Energy Materials*, *10*(15), 2000124. https://doi.org/10.1002/AENM.202000124

Kazmerski, L. L., White, F. R., & Morgan, G. K. (1976). Thin-film CuInSe2/CdS heterojunction solar cells. *Applied Physics Letters*, *29*(4), 268–270. https://doi.org/10.1063/1.89041

Kim, H. S., Lee, C. R., Im, J. H., Lee, K. B., Moehl, T., Marchioro, A., et al. (2012). Lead iodide perovskite sensitized all-solid-state submicron thin film mesoscopic solar cell with efficiency exceeding 9%. *Scientific Reports*, *2*, 1–7. https://doi.org/10.1038/srep00591

Kim, J. H., Liang, P. W., Williams, S. T., Cho, N., Chueh, C. C., Glaz, M. S., et al. (2015). High-performance and environmentally stable planar heterojunction perovskite solar cells based on a solution-processed copper-doped nickel oxide hole-transporting layer. *Advanced Materials*, *27*(4), 695–701. https://doi.org/10.1002/adma.201404189

Kofstad, P. (1995). Defects and transport properties of metal oxides. *Oxidation of Metals*, *44*(1–2), 3–27. https://doi.org/10.1007/BF01046721

Kojima, A., Teshima, K., Shirai, Y., & Miyasaka, T. (2009). Organometal halide perovskites as visible-light sensitizers for photovoltaic cells. *Journal of the American Chemical Society*, *131*(17), 6050–6051. https://doi.org/10.1021/ja809598r

Kumar, N., Rani, J., & Kurchania, R. (2021). A review on power conversion efficiency of lead iodide perovskite-based solar cells. *Materials Today: Proceedings*, *46*, 5570–5574. https://doi.org/10.1016/j.matpr.2020.09.349

Kumar, N., Lee, H. B., Hwang, S., & Kang, J. W. (2020). Large-area, green solvent spray deposited nickel oxide films for scalable fabrication of triple-cation perovskite solar cells. *Journal of Materials Chemistry A*, *8*(6), 3357–3368. https://doi.org/10.1039/c9ta13528f

Kuşoğlu, İ. M. (2011). *Demir esaslı metal tozlarından geleneksel ve mikrodalga sinterleme yöntemleri ile malzeme üretimi ve özelliklerinin karşılaştırılması*. Phd Thesis, Dokuz Eylül University, İzmir.

Lee, M. M., Teuscher, J., Miyasaka, T., Murakami, T. N., & Snaith, H. J. (2012). Efficient hybrid solar cells based on meso-superstructured organometal halide perovskites. *Science*, *338*(6107), 643–647. https://doi.org/10.1126/SCIENCE.1228604

Lee, T. D., & Ebong, A. U. (2017). A review of thin film solar cell technologies and challenges. *Renewable and Sustainable Energy Reviews*, *70*, 1286–1297. https://doi.org/10.1016/j.rser.2016.12.028

Li, G. R., & Gao, X. P. (2020). Low-cost counter-electrode materials for dye-sensitized and perovskite solar cells. *Advanced Materials*, *32*(3), 1–20. https://doi.org/10.1002/adma.201806478

Li, S., Cao, Y. L., Li, W. H., & Bo, Z. S. (2021). A brief review of hole transporting materials commonly used in perovskite solar cells. *Rare Metals*, *40*(10), 2712–2729. https://doi.org/10.1007/s12598-020-01691-z

Li, Y., Li, X., Wang, Z., Guo, H., & Li, T. (2016). One-step synthesis of Li-doped NiO as high-performance anode material for lithium ion batteries. *Ceramics International*, *42*(13), 14565–14572.

Lin, L., Jones, T. W., Yang, T. C. J., Duffy, N. W., Li, J., Zhao, L., et al. (2021). Inorganic electron transport materials in perovskite solar cells. *Advanced Functional Materials*, *31*(5), 1–24. https://doi.org/10.1002/adfm.202008300

Liu, D., Li, Y., Yuan, J., Hong, Q., Shi, G., Yuan, D., et al. (2017). Improved performance of inverted planar perovskite solar cells with F4-TCNQ doped PEDOT:PSS hole transport layers. *Journal of Materials Chemistry A*, *5*(12), 5701–5708. https://doi.org/10.1039/C6TA10212C

Liu, L., Xi, Q., Gao, G., Yang, W., Zhou, H., Zhao, Y., et al. (2016). Cu2O particles mediated growth of perovskite for high efficient hole-transporting-layer free solar cells in ambient conditions. *Solar Energy Materials and Solar Cells*, *157*, 937–942.

Liu, M. H., Zhou, Z. J., Zhang, P. P., Tian, Q. W., Zhou, W. H., Kou, D. X., et al. (2016). p-type Li, Cu-codoped NiOx hole-transporting layer for efficient planar perovskite solar cells. *Optics Express*, *24*(22), A1349.

Luo, J., Xia, J., Yang, H., Chen, L., Wan, Z., Han, F., et al. (2018). Toward high-efficiency, hysteresis-less, stable perovskite solar cells: unusual doping of a hole-transporting material using a fluorine-containing hydrophobic Lewis acid. *Energy & Environmental Science*, *11*(8), 2035–2045.

Ma, F., Zhao, Y., Li, J., Zhang, X., Gu, H., & You, J. (2021). Nickel oxide for inverted structure perovskite solar cells. *Journal of Energy Chemistry*, *52*, 393–411. https://doi.org/10.1016/J.JECHEM.2020.04.027

Mandelkorn, J., & Lamneck Jr, J. H. (1973). A new electric field effect in silicon solar cells. *Journal of Applied Physics*, *44*(10), 4785. https://doi.org/10.1063/1.1662040

Marinova, N., Valero, S., & Delgado, J. L. (2017). Organic and perovskite solar cells: Working principles, materials and interfaces. *Journal of Colloid and Interface Science*, *488*, 373–389. https://doi.org/10.1016/j.jcis.2016.11.021

Martin, P. M. (2010). Deposition tTechnologies: An overview. In *Handbook of deposition technologies for films and coatings* (3rd ed., pp. 1–31). Oxford: Elsevier. https://doi.org/10.1016/B978-0-8155-2031-3.00001-6

Massiot, I. (2014). *Design and fabrication of nanostructures for light-trapping in ultra-thin solar cells*. Phd Thesis, Paris Sud University, Paris.

Mastuli, M. S., Kamarulzaman, N., Nawawi, M. A., Mahat, A. M., Rusdi, R., & Kamarudin, N. (2014). Growth mechanisms of MgO nanocrystals via a sol-gel synthesis using different complexing agents. *Nanoscale Research Letters*, *9*(1), 1–9. https://doi.org/10.1186/1556-276X-9-134

Matsubara, K., Huang, S., Iwamoto, M., & Pan, W. (2014). Enhanced conductivity and gating effect of p-type Li-doped NiO nanowires. *Nanoscale*, *6*(2), 688–692.

Matsui, T., Bidiville, A., Maejima, K., Sai, H., Koida, T., Suezaki, T., et al. (2015). High-efficiency amorphous silicon solar cells: Impact of deposition rate on metastability. *Applied Physics Letters*, *106*(5). https://doi.org/10.1063/1.4907001

Mattox, D. M. (2010). Physical sputtering and sputter deposition (sputtering). In *Handbook of physical vapor deposition (PVD) processing* (pp. 237–286). Oxford: Elsevier. https://doi.org/10.1016/B978-0-8155-2037-5.00007-1

Maurya, D. K., Sardarinejad, A., & Alameh, K. (2014). Recent developments in R.F. magnetron sputtered thin films for pH sensing applications - An overview. *Coatings*, *4*(4), 756–771.

Mehrotra, P. K. (2014). Powder processing and green shaping. *Comprehensive Hard Materials*, *1*, 213–235. https://doi.org/10.1016/B978-0-08-096527-7.00007-6

Mitzi, D. B., Feild, C. A., Harrison, W. T. A., & Guloy, A. M. (1994). Conducting tin halides with a layered organic-based perovskite structure. *Nature*, *369*(6463), 467–469. https://doi.org/10.1038/369467a0

Moulder, J. F., Stickle, W. F., Sobol, P. E., & Bomben, K. D. (1992). *Handbook of X-ray photoelectron spectroscopy*. Minnesota, USA: Perkin-Elmer Corporation.

Nakamura, M., Yamaguchi, K., Kimoto, Y., Yasaki, Y., Kato, T., & Sugimoto, H. (2019). Cd-Free Cu(In,Ga)(Se,S)2 thin-film solar cell with record efficiency of 23.35%. *IEEE Journal of Photovoltaics*, *9*(6), 1863–1867. https://doi.org/10.1109/JPHOTOV.2019.2937218

Nandy, S., Saha, B., Mitra, M. K., & Chattopadhyay, K. K. (2007). Effect of oxygen partial pressure on the electrical and optical properties of highly (200) oriented p-type Ni1−x O films by DC sputtering. *Journal of Materials Science*, *42*(14), 5766–5772. https://doi.org/10.1007/s10853-006-1153-x

National Renewable Energy Laboratory [NREL]. (2021). *Best research-cell efficiency chart.* Retrieved November 15, 2021, from https://www.nrel.gov/pv/cell-efficiency.html

Neacşu, I. A., Nicoară, A. I., Vasile, O. R., & Vasile, B. Ş. (2016). Inorganic micro- and nanostructured implants for tissue engineering. *Nanobiomaterials in Hard Tissue Engineering: Applications of Nanobiomaterials*, 271–295. https://doi.org/10.1016/B978-0-323-42862-0.00009-2

Nie, W., Tsai, H., Blancon, J. C., Liu, F., Stoumpos, C. C., Traore, B., et al. (2018). Critical role of interface and crystallinity on the performance and photostability of perovskite solar cell on nickel oxide. *Advanced Materials*, *30*(5), 1–9.

Niveditha, C. V., Fatima, M. J. J., & Sindhu, S. (2016). Comprehensive interfacial study of potentio-dynamically synthesized copper oxide thin films for photoelectrochemical applications. *Journal of The Electrochemical Society*, *163*(6), H426–H433. https://doi.org/10.1149/2.0971606jes

Nouri, E., Mohammadi, M. R., & Lianos, P. (2018). Construction of perovskite solar cells using inorganic hole-extracting components. *ACS Omega*, *3*(1), 46–54.

O'Regan, B., & Grätzel, M. (1991). A low-cost, high-efficiency solar cell based on dye-sensitized colloidal TiO2 films. *Nature*, *353*(6346), 737–740.

Panigrahi, U. K., Sathe, V., Babu, P. D., Mitra, A., & Mallick, P. (2020). Effect of Mg doping on the improvement of photoluminescence and magnetic properties of NiO nanoparticles. *Nano Express*, *1*(2), 020009. https://doi.org/10.1088/2632-959x/aba285

Park, J. H., Seo, J., Park, S., Shin, S. S., Kim, Y. C., Jeon, N. J., et al. (2015). Efficient CH3NH3PbI3 perovskite solar cells employing nanostructured p-Type NiO electrode formed by a pulsed laser deposition. *Advanced Materials*, *27*(27), 4013–4019. https://doi.org/10.1002/ADMA.201500523

Park, N. G. (2015). Perovskite solar cells: An emerging photovoltaic technology. *Materials Today*, *18*(2), 65–72. https://doi.org/10.1016/J.MATTOD.2014.07.007

Pauw, Lj. (1958). A method of measuring specific resistivity and Hall effect of discs of arbitrary shape. *Philips Research Reports*, *13*(1), 1–9.

Pham, N. D., Shang, J., Yang, Y., Hoang, M. T., Tiong, V. T., Wang, X., et al. (2020). Alkaline-earth bis(trifluoromethanesulfonimide) additives for efficient and stable perovskite solar cells. *Nano Energy*, *69*, 104412. https://doi.org/10.1016/J.NANOEN.2019.104412

Philipps, S., Burger, B., Kiefer, K., & Kost, C. (2018). *Photovoltaics Report*. Retrieved July 27, 2021 from https://www.ise.fraunhofer.de/content/dam/ise/de/documents/publications/studies/Photovoltaics-Report.pdf

Qiu, Z., Gong, H., Zheng, G., Yuan, S., Zhang, H., Zhu, X., et al. (2017). Enhanced physical properties of pulsed laser deposited NiO films via annealing and lithium doping for improving perovskite solar cell efficiency. *Journal of Materials Chemistry C*, *5*(28), 7084–7094. https://doi.org/10.1039/c7tc01224a

Ranabhat, K., Patrikeev, L., Antal'evna-Revina, A., Andrianov, K., Lapshinsky, V., & Sofronova, E. (2016). An introduction to solar cell technology. *Journal of Applied Engineering Science*, *14*(4), 481–491. https://doi.org/10.5937/jaes14-10879

Rao, H., Sun, W., Ye, S., Yan, W., Li, Y., Peng, H., et al. (2016). Solution-processed CuS NPs as an inorganic hole-selective contact material for inverted planar perovskite solar cells. *ACS Applied Materials and Interfaces*, *8*(12), 7800–7805. https://doi.org/10.1021/ACSAMI.5B12776

Raoufi, D., Kiasatpour, A., Fallah, H. R., & Rozatian, A. S. H. (2007). Surface characterization and microstructure of ITO thin films at different annealing temperatures. *Applied Surface Science*, *253*(23), 9085–9090. https://doi.org/10.1016/j.apsusc.2007.05.032

Raoufi, D., & Taherniya, A. (2015). The effect of substrate temperature on the microstructural, electrical and optical properties of Sn-doped indium oxide thin films. *EPJ Applied Physics*, *70*(3). https://doi.org/10.1051/epjap/2015150004

REN21. (2021). *Renewables 2021 global status report.* Paris.

Righini, G. C., & Enrichi, F. (2020). Solar cells' evolution and perspectives: a short review. In *Solar Cells and Light Management* (pp. 1–32). Amsterdam: Elsevier. https://doi.org/10.1016/B978-0-08-102762-2.00001-X

Ryu, H. W., Choi, G. P., Hong, G. J., & Park, J. S. (2004). Growth and surface morphology of textured NiO thin films deposited by off-axis RF magnetron sputtering. *Japanese Journal of Applied Physics, Part 1: Regular Papers and Short Notes and Review Papers*, *43*, 5524–5525. https://doi.org/10.1143/JJAP.43.5524

Sajid, S., Elseman, A. M., Huang, H., Ji, J., Dou, S., Jiang, H., et al. (2018). Breakthroughs in NiOx-HTMs towards stable, low-cost and efficient perovskite solar cells. *Nano Energy*, *51*, 408–424. https://doi.org/10.1016/j.nanoen.2018.06.082

Salim, T., Sun, S., Abe, Y., Krishna, A., Grimsdale, A. C., & Lam, Y. M. (2015). Perovskite-based solar cells: impact of morphology and device architecture on device performance. *Journal of Materials Chemistry A*, *3*(17), 8943–8969. https://doi.org/10.1039/C4TA05226A

Sarıtaş, S., Türker, M., & Durlu, N. (2007). Toz metalurjisi ve parçacıklı malzeme işlemleri. *Türk Toz Metalurjisi Yayınları*, *5*, 2–34.

Sathiyan, G., Syed, A. A., Chen, C., Wu, C., Tao, L., Ding, X., et al. (2020). Dual effective dopant based hole transport layer for stable and efficient perovskite solar cells. *Nano Energy*, *72*, 104673. https://doi.org/10.1016/J.NANOEN.2020.104673

Schmahl, N. G., Barthel, J., & Eikerling, G. F. (1964). Röntgenographische untersuchungen an den systemen MgO-CuO und NiO-CuO. *Zeitschrift Für Anorganische Und Allgemeine Chemie*, *332*(5–6), 230–237.

Seo, J. Y., Kim, H. S., Akin, S., Stojanovic, M., Simon, E., Fleischer, M., et al. (2018). Novel p-dopant toward highly efficient and stable perovskite solar cells. *Energy Environ. Sci*, *11*, 2985. https://doi.org/10.1039/c8ee01500g

Shannon, R. D. (1976). Revised effective ionic radii and systematic studies of interatomic distances in halides and chalcogenides. *Acta Crystallographica Section A*, *32*(5), 751–767. https://doi.org/10.1107/S0567739476001551/FULL

Sheena, P. A., Priyanka, K. P., Sabu, N. A., Sabu, B., & Varghese, T. (2014). Effect of calcination temperature on the structural and optical properties of nickel oxide nanoparticles. *Nanosystems: Physics, Chemistry, Mathematics*, *5*(3), 441–449.

Song, Z., Watthage, S. C., Phillips, A. B., & Heben, M. J. (2016). Pathways toward high-performance perovskite solar cells: review of recent advances in organo-metal halide perovskites for photovoltaic applications. *Journal of Photonics for Energy*, *6*(2), 022001. https://doi.org/10.1117/1.jpe.6.022001

Sönmezoğlu, S., Koç, M., & Akın, S. (2012). İnce film üretim teknikleri. *Erciyes Üniversitesi Fen Bilimleri Enstitüsü Fen Bilimleri Dergisi*, *28*(5), 389–404.

Soo Kim, D., & Chul Lee, H. (2012). Nickel vacancy behavior in the electrical conductance of nonstoichiometric nickel oxide film. *Journal of Applied Physics*, *112*(3), 1–5. https://doi.org/10.1063/1.4742993

Sta, I., Jlassi, M., Kandyla, M., Hajji, M., Koralli, P., Allagui, R., et al. (2015). Hydrogen sensing by sol-gel grown NiO and NiO:Li thin films. *Journal of Alloys and Compounds*, *626*, 87–92. https://doi.org/10.1016/j.jallcom.2014.11.151

Tao, Y. (2016). Screen-printed front junction n-type silicon solar cells. In *Printed electronics - Current trends and applications* (pp. 47–73). London: InTech. https://doi.org/10.5772/63198

Teoh, L. G., & Li, K. D. (2012). Synthesis and characterization of NiO nanoparticles by sol-gel method. *Materials Transactions*, *53*(12), 2135–2140. https://doi.org/10.2320/matertrans.M2012244

Thongtem, T., & Thongtem, S. (2005). Preparation and characterization of Li 1-x Ni 1+ x O 2 powder used as cathode materials. *Advances in Technology of Materials and Materials Processing Journal*, *7*(1), 71–76.

Tirado, J., Roldán-Carmona, C., Muñoz-Guerrero, F. A., Bonilla-Arboleda, G., Ralaiarisoa, M., Grancini, G., et al. (2019). Copper sulfide nanoparticles as hole-transporting-material in a fully-inorganic blocking layers n-i-p perovskite solar cells: Application and working insights. *Applied Surface Science*, *478*, 607–614. https://doi.org/10.1016/J.APSUSC.2019.01.289

Toygun, Ş., Köneçoğlu, G., & Kalpaklı, Y. (2013). Sol-jel yöntemi genel prensipleri. *Sigma : Mühendislik ve Fen Bilimleri Dergisi*, *31*(4), 456–476.

Upadhyaya, G. S. (2002). *Powder metallurgy technology*. Cambridge: Cambridge International Science Publishing.

Van Overstraeten, R. (1990). Crystalline silicon solar cells for one sun utilisation. *Energy and the Environment*, 104–111. https://doi.org/10.1016/B978-0-08-037539-7.50013-2

Wang, K., Shen, P., Li, M., Chen, S., Lin, M., Chen, P., et al. (2014). Low-temperature sputtered nickel oxide compact thin film as effective electron blocking layer for mesoscopic NiO/CH3NH3PbI3 perovskite heterojunction solar cells. *ACS Applied Materials & Interfaces*, *6*, 11851−11858.

Wang, Q., Lin, Z., Su, J., Hu, Z., Chang, J., & Hao, Y. (2021). Recent progress of inorganic hole transport materials for efficient and stable perovskite solar cells. *Nano Select*, *2*(6), 1055–1080. https://doi.org/10.1002/nano.202000238

Wang, T., Ding, D., Zheng, H., Wang, X., Wang, J., Liu, H., et al. (2019). Efficient inverted planar perovskite solar cells using ultraviolet/ozone-treated NiOx as the hole transport layer. *Solar RRL*, *3*(6), 1900045. https://doi.org/10.1002/SOLR.201900045

Wilson, G. M., Al-jassim, M., Metzger, W. K., Glunz, S. W., Verlinden, P., Xiong, G., et al. (2020). *The 2020 photovoltaic technologies roadmap*. *Journal of Physics D: Applied Physics*, *53*(49), 493001. https://doi.org/10.1088/1361-6463/ab9c6a

Xie, F., Chen, C. C., Wu, Y., Li, X., Cai, M., Liu, X., et al. (2017). Vertical recrystallization for highly efficient and stable formamidinium-based inverted-structure perovskite solar cells. *Energy and Environmental Science*, *10*(9), 1942–1949. https://doi.org/10.1039/c7ee01675a

Xu, D., He, K., Chen, B. H., Jiao, L., Wu, W., Mu, S., et al. (2015). Dielectric and varistor properties of Cu doped Li0.02Ni0.98O ceramics. *Journal of Materials Science: Materials in Electronics*, *26*(12), 9831–9836. https://doi.org/10.1007/s10854-015-3657-0

Xu, L., Chen, X., Jin, J., Liu, W., Dong, B., Bai, X., et al. (2019). Inverted perovskite solar cells employing doped NiO hole transport layers: A review. *Nano Energy*, *63*(June), 103860. https://doi.org/10.1016/j.nanoen.2019.103860

Yan, H., Zhang, D., Xu, J., Lu, Y., Liu, Y., Qiu, K., et al. (2014). Solution growth of NiO nanosheets supported on Ni foam as high-performance electrodes for supercapacitors. *Nanoscale Research Letters*, *9*(1), 1–7. https://doi.org/10.1186/1556-276X-9-424

Yan, W., Li, Y., Li, Y., Ye, S., Liu, Z., Wang, S., et al. (2015). High-performance hybrid perovskite solar cells with open circuit voltage dependence on hole-transporting materials. *Nano Energy*, *16*, 428–437. https://doi.org/10.1016/J.NANOEN.2015.07.024

Ye, S., Liu, Z., Bian, Z., & Huang, C. (2018). Oxide hole transport materials in inverted planar perovskite solar cells. In *the future of semiconductor oxides in next-generation solar cells* (pp. 117–158). Amsterdam: Elsevier. https://doi.org/10.1016/B978-0-12-811165-9.00004-1

Ye, S., Sun, W., Li, Y., Yan, W., Peng, H., Bian, Z., et al. (2015). CuSCN-Based Inverted Planar Perovskite Solar Cell with an Average PCE of 15.6%. *Nano Letters*, *15*(6), 3723–3728. https://doi.org/10.1021/ACS.NANOLETT.5B00116

Yu, J. C., Hong, J. A., Jung, E. D., Kim, D. B., Baek, S. M., Lee, S., et al. (2018). Highly efficient and stable inverted perovskite solar cell employing PEDOT:GO composite layer as a hole transport layer. *Scientific Reports 2018 8:1*, *8*(1), 1–9. https://doi.org/10.1038/s41598-018-19612-7

Zhang, Y., Elawad, M., Yu, Z., Jiang, X., Lai, J., & Sun, L. (2016). Enhanced performance of perovskite solar cells with P3HT hole-transporting materials via molecular p-type doping. *RSC Advances*, *6*(110), 108888–108895. https://doi.org/10.1039/C6RA21775C

Zayim, E. O., Turhan, I., Tepehan, F. Z., & Ozer, N. (2008). Sol-gel deposited nickel oxide films for electrochromic applications. *Solar Energy Materials and Solar Cells*, *92*(2), 164–169. https://doi.org/10.1016/j.solmat.2007.03.034

Zhang, Y., Liu, W., Tan, F., & Gu, Y. (2015). The essential role of the poly(3-hexylthiophene) hole transport layer in perovskite solar cells. *Journal of Power Sources*, *274*, 1224–1230. https://doi.org/10.1016/J.JPOWSOUR.2014.10.145

Zhang, Z., Li, Z., Meng, L., Lien, S. Y., & Gao, P. (2020). Perovskite-based tandem solar cells: Get the most out of the sun. *Advanced Functional Materials*, *30*(38). https://doi.org/10.1002/adfm.202001904

Zhao, Y., Wang, H., Wu, C., Shi, Z. F., Gao, F. B., Li, W. C., et al. (2014). Structures, electrical and optical properties of nickel oxide films by radio frequency magnetron sputtering. *Vacuum*, *103*, 14–16. https://doi.org/10.1016/j.vacuum.2013.11.009

Zuo, C., & Ding, L. (2015). Solution-processed Cu2O and CuO as hole transport materials for efficient perovskite solar cells. *Small*, *11*(41), 5528–5532. https://doi.org/10.1002/SMLL.201501330

Zuo, C., & Ding, L. (2017). Modified PEDOT layer makes a 1.52 V Voc for perovskite/PCBM solar cells. *Advanced Energy Materials*, *7*(2), 1601193. https://doi.org/10.1002/AENM.201601193

Zweibel, K., & Hersch, P. (1984). Basic photovoltaic principles and methods. In *Van Nostrand Reinhold*. Colorado: Van Nostrand Reinhold. https://doi.org/10.2172/5191389

APPENDICES

APPENDIX 1: ABBREVIATIONS

PV: Photovoltaic

GW: Gigawatt

Cz: Czochralski

a-Si: Amorphous Silicon

CIGS: Copper Indium Gallium Selenide

CdTe: Cadmium Telluride

DSSC: Dye-Sensitized Solar Cell

PSC: Perovskite Solar Cell

PCE: Power Conversion Efficiency

NiO: Nickel Oxide

HTM: Hole Transport Material / Layer

ITO: Indium Tin Oxide

AM: Air Mass

I_{SC}: Short Circuit Current

V_{OC}: Open Circuit Voltage

FF: Fill Factor

PSK: Perovskite Absorber Layer

ETM: Electron Transport Material / Layer

TCO: Transparent Conductive Oxide

MC: Metallic Contact

FTO: Fluorine Doped Tin Oxide

MAI: Methylammonium Iodide

PbI_2: Lead(II) Iodide

$MAPbI_3$: Methylammonium Lead Iodide

$FAPbI_3$: Formamidinium Lead Iodide

PCBM: ([6,6]-phenyl-C61-butyric acid methyl ester)

VBM: Valance Band Maximum

CBM: Conduction Band Minimum

HOMO: High Occupied Molecular Orbital

LUMO: Low Unoccupied Molecular Orbital

GBL: Gamma-Butyrolactone

DMSO: Dimethyl Sulfoxide

DMF: Dimethylformamide

PEDOT:PSS: Poly(3,4-ethylenedioxythiophene)-poly(styrenesulfonate)

IO:H: Hydrogen-Doped Indium Oxide

IZO: Indium Zinc Oxide

AZO: Aluminum-Doped Zinc Oxide

spiro-OMeTAD: 2,2',7,7'-Tetrakis[N,N-di(4-methoxyphenyl)amino]-9,9'-spirobifluorenethe

PTAA: Poly[bis(4-phenyl)(2,4,6-trimethylphenyl)amine]

P3HT: Poly(3-hexylthiophene)

tPB: 4-tert-Butylpyridine

Li-TFSI: Lithium bis(trifluoromethanesulfonyl)imide

PSS-Na: Poly(sodium-4-styrene sulfonate)

F4TCNQ: 2,3,5,6-Tetrafluoro-7,7,8,8-tetracyanoquinodimethane

CuO: cupric oxide and

Cu_2O: cuprous oxide

CuS: Copper sulfide

CuSCN: Copper(I) thiocyanate

CSD: Chemical Solution Deposition

CVD: Chemical Vapor Deposition

PVD: Physical Vapor Deposition

DC: Direct Current

RF: Radio Frequency

CIP: Cold Isostatic Press

HIP: Hot Isostatic Press

SCCM: Standard Cubic Centimeters per Minute

PVDF: Polyvinylidene Fluoride

FTIR: Fourier Transform Infrared Spectroscopy

ATR: Attenuated Total Reflection

XRD: X-Ray Diffractometer

SEM: Scanning Electron Microscope

SE: Secondary Electron

XPS: X-Ray Photoelectron Spectroscopy

PL: Photoluminescence

MPP: Maximum Power Point